In vitro and *in silico* modelling of arteriovenous malformations for surgical planning

Jordan Lee Bougardt

A dissertation submitted to the Faculty of Engineering and the Built Environment, University of the Witwatersrand, Johannesburg, in fulfilment of the requirements for the degree of Master of Science in Engineering.

Johannesburg

2024

DECLARATION

I declare that this dissertation is my own unaided work. It is being submitted to the Degree of Master of Science to the University of the Witwatersrand, Johannesburg. It has not been submitted before for any degree or examination to any other University.

5th day of June 2024

ABSTRACT

Modelling vascular pathologies and associated interventions using computational fluid dynamics (CFD) techniques can improve pre-surgical planning. This study examines arteriovenous malformations (AVMs), which involve the direct shunting of high-pressure arterial blood into low-pressure venous circulation, leading to severe ischemic events (strokes, seizures, etc.) for which coil embolisation, aimed at complete flow blockage, is the preferred intervention technique.

Vascular parameters, including blood rheology, patient-derived vasculature, and haemostasis, were computationally replicated to augment physiological accuracy, while the flow blockage of the embolising coil and clot formations were modelled through cell-based porous media approaches.

This investigation evaluates AVM characteristics and treatment efficacy, emphasizing the impact of coil number and insertion angle on flow reduction and thrombogenesis. Results indicate that a minimum of three coils are required for successful embolisation, while the preferred insertion angle was determined to be that which is aligned with the blood vessel axis, i.e., a 0° angle of insertion.

CURRENT AND FORTHCOMING PUBLICATIONS

This work has already generated a publication and is scoped to include several more which reflect key advancements in the modelling of arteriovenous malformations for surgical planning. The completed and planned publications are listed below:

1. **Published Conference Paper**

   Title: *In-vitro* and *in-silico* modelling of Arteriovenous Malformations for Surgical Planning

   Conference: 13th South African Conference on Computational and Applied Mechanics (SACAM) 2024

   This paper explores the use of porous media models to simulate the impact of embolisation coils on haemodynamics during embolisation procedures.

2. Journal Article (In Preparation)

   Planned Journal: Physics of Fluids special topics on "Recent Advances in Fluid Dynamics and Its Applications"

   This article investigates the feasibility of using 4D-MRI as an experimental validation tool for CFD.

3. Comprehensive Study (Planned)

   A comprehensive paper is planned to encapsulate the computational and experimental work of this research, presenting the primary findings and outcomes, so as to provide a full picture of the modelling approach and results.

4. Conference Paper (Accepted Abstract)

   Conference: 14th South African Conference on Computational and Applied Mechanics (SACAM) 2025

   This upcoming paper compares a coupled biochemical-haemodynamic clotting model with a purely haemodynamic model, offering insights into the applicability of the latter in the simulation of clot formation.

Dedication

I dedicate this work to my mother, for your tireless care and constant encouragement. To my father, for your unwavering belief in me. To my brother, for your insightful guidance. To my girlfriend, for your love and support. And to my friends, for your endless encouragement and advice. Your support has carried me through and lifted me up.

Thank you.

ACKNOWLEDGEMENTS

I extend my deepest gratitude to Prof. Wei Hua Ho for introducing me to biomechanics and providing invaluable mentorship in computational and experimental flow dynamics. My sincere thanks also go to Dr. Randall Paton for his expert guidance in computational flow and CFD, which greatly facilitated my learning and kept my project focused. I am grateful to Prof. Malebogo Ngoepe for her support in the computational modelling of thrombosis, which was crucial for developing a coherent and innovative approach to blood clotting.

I would like to thank Prof. Davd Chandler for kindly offering his time and effort to aid in the collection of rheological data which formed the foundation of the synthesis of a blood-replicate used for the experimental verification of this work.

I extend my sincere thanks to Prof. Jay Pillai, Dr. Cecil Pule, and Dr. Karabo Moisane from the Donald Gordon Medical Center for their numerous contributions. Their expertise ensured the clinical relevance of my data and provided essential knowledge and resources, including the crucial patient-derived geometry. Special appreciation goes to Dr. Pule for his dedicated effort in ensuring I had the necessary information and resources to succeed.

I am deeply grateful to the University of Twente for their generous provision of the tabletop MRI. Special thanks go to Dr. Frank Simonis for his expertise in MRI imaging and invaluable guidance, which ensured the success of my 4D MRI velocimetry results. The data obtained was essential for the experimental verification of my research.

I thank Barbara Wohlmuth, Markus Muhr, and Fabian Holzberger from the Technical University of Munich, School of Computation, Information, and Technology (CIT). Their work on simulating coil behaviour was integral to my research. I am especially grateful to Fabian for his collaboration and detailed communication, and to Markus for providing coil data in a format compatible with the Fluent solver, which greatly enhanced my study.

CONTENTS

LIST OF FIGURES

LIST OF TABLES

LIST OF ABBREVIATIONS

CFD	Computational Fluid Dynamics
AVM	Arteriovenous Malformation
pAVM	Peripheral Arteriovenous Malformation
SRS	Stereotactic Radiosurgery
MR	Magnetic Resonance
MRA	Magnetic Resonance Angiography
AV	Arteriovenous
CT	Computed Tomography
DGMC	Donald Gordon Medical Center
TUM	Technical University of Munich, Germany
MRI	Magnetic Resonance Imaging
UT	University of Twente, Netherlands
3D	Three-Dimensional
HU	Hounsfield Units
CAD	Computer-Aided Design
STL	Stereolithographic
4D	Four-Dimensional
ID	Internal Diameter
BMF	Blood Mimicking Fluid
DER	Discrete Elastic Rod
CGNS	CFD General Notation System
CSV	Comma-Separated Values
UDF	User Defined Function
UDMI	User Defined Memory Index
UDM	User Defined Memory
PISO	Pressure-Implicit with Splitting of Operations
PRESTO!	Pressure Staggered Option
RF	Radiofrequency
PC	Phase Contrast
VENC	Velocity Encoding
B	Baseline Embolisation Case
S	Single Coil Packing
D	Double Coil Packing
T	Triple Coil Packing
DSA	Digital Subtraction Angiography
LOD	Limit of Detectability
FOV	Field of View

NOMENCLATURE

s	Arc length [m]
$\boldsymbol{m}$	Axis of orthonormal frame
α	Bending stiffness
ΔG	Bipolar gradient strength
$\boldsymbol{\kappa}$	Centerline curvature of material frame
γ	Central curvature {DER}
ΔP	Change in Pressure [Pa]
λ	Characteristic time or consistency [s]
R^2	Coefficient of determination
ρ	Density [$\mathrm{kg/m^3}$]
$\emptyset$	Diameter
η	Dynamic viscosity [$\mathrm{Pa \cdot s}$]
E	Elastic energy
k	Flow resistance in Simplified Darcy-Weisbach
z	Fluid height [m]
Δt	Gradient duration
γ	Gyromagnetic ratio {MRI}
C_2	Inertial Resistance Coefficient [$\mathrm{m^{-1}}$]
η_∞	Infinite viscosity [$\mathrm{Pa \cdot s}$]
$\boldsymbol{F'}$	Internal force vector
$\boldsymbol{M}$	Internal moment vector
Δn	Length of coil in flow-wise direction
C_{min}	Minimum contrast concentration [$\mathrm{mg\ I/ml}$]
S_i	Momentum sink term [$\mathrm{kg \cdot ms^{-1}}$]
η_0	Near-zero viscosity [$\mathrm{Pa \cdot s}$]
$\Delta\phi$	Phase offset
$\boldsymbol{r}$	Position vector
n	Power law index
ΔP_{AVM}	Pressure drop over the AVM [mmHg]
$\dot{\gamma}$	Shear rate [$\mathrm{s^{-1}}$]
$\boldsymbol{t}$	Tangent vector
β	Twist stiffness
v	Velocity [$\mathrm{m/s}$]
$\emptyset_v$	Vessel diameter [mm]
$\dot{\gamma}_{AVM}$	Volume-averaged AVM shear rate [$\mathrm{s^{-1}}$]
Q	Volumetric flow rate [$\mathrm{m^3/s}$]
Q_{AVM}	Volumetric flow rate through the malformation

1 INTRODUCTION

1.1 Background Information

Arteriovenous Malformations (AVMs) are vascular abnormalities which allow the intermixing of high pressure arterial and low-pressure venous blood flow through a variety of interwoven vessels and/or capillaries (Yakes & Baumgartner, 2014), in the absence of a capillary bed (location of blood-tissue perfusion). Arteries entering the AVM are referred to as feeder arteries, the bundled capillary network as the nidus and the exiting veins are known as draining veins. AVMs are typically found in the brain (47,4%); however, they may occur outside of the nervous system, i.e., in the extremities (28,5%) (Uller *et al*, 2014) where they are termed peripheral (pAVMs). AVMs have a global prevalence of 10 - 18 individuals per 100,000 (Rutledge *et al*, 2014), and thus are relatively rare yet clinically significant, posing considerable risks to the affected.

AVMs can present as a variety of different structures depending on their biological environment, surrounding anatomy and vascular tree. For example, a conglomeration of multiple feeder arteries shunting into a singular vein may cause the vein to swell, becoming aneurysmal (IIIa), i.e., exhibiting swelling of the arterial wall. The Yakes classification scheme is an established, simple categorisation of different AVM types as listed in Table 1, wherein the AVMs are arranged in order of increasing complexity and potential risk.

Table 1: Yakes AVM classification {A-Arterial, V-Venous}

Type I: A direct artery-to-vein attachment without interconnecting nidus.	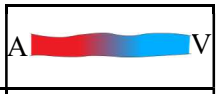
Type II: Multiple feeder arteries attached via an interconnecting nidus which drains into multiple outflow veins.	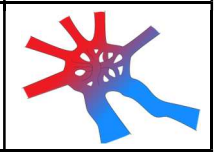
Type IIIa: Multiple inflow arterioles shunt into a draining aneurysmal vein wall that has a single outflow vein.	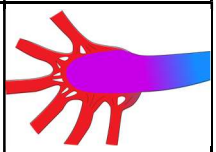
Type IIIb: Multiple feeder arterioles shunt into an aneurysmal vein with multiple outflow veins. AV tubes infiltrate the aneurysmal vein wall.	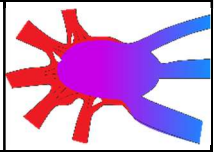
Type IV: Multiple arteries/oles form micro-fistulae that diffusely infiltrate the affected tissue, while interspersed capillary beds maintain viability.	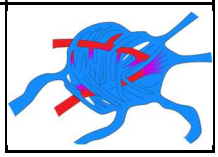

AVMs commonly originate as congenital lesions, present from birth, which remain dormant during childhood and worsen over time. AVMs may also develop during adolescence and rarely adulthood. Left untreated, AVMs cause significant and potentially lethal symptoms, often related to their rupture, e.g., various forms of ischaemia (inadequate blood supply) such as gangrene, haemorrhage (internal bleeding), stroke, and seizures (Barreau *et al*, 2014) as well as cardiac overload and heart failure (Uller *et al*, 2014). The AVM mortality rate is 10 – 15% (Bokhari & Bokhari, 2023), while $23 - 40\%$ (Majamdar & McWilliams, 2020) of AVM haemorrhage survivors suffer from significant difficulties.

Arteriovenous Malformations and related pathologies (e.g., aneurysms) are notoriously difficult to treat, generally requiring extensive surgery and post-surgical care. Prevalent treatment strategies for AVMs include endovascular (within blood vessels) embolisation, microsurgery and stereotactic radiosurgery (SRS), however, recent advancements in transcatheter embolotherapy, the targeted delivery of flow-blocking agents (chemical or physical) through blood vessels, have established it as the standard of care. As illustrated in Figure 1 with data taken from Nataraj *et al* (2014), over 50% of AVM treatments currently involve endovascular embolisation and as a practice it is also frequently combined with other treatment modalities, reflecting its growing prominence in AVM management.

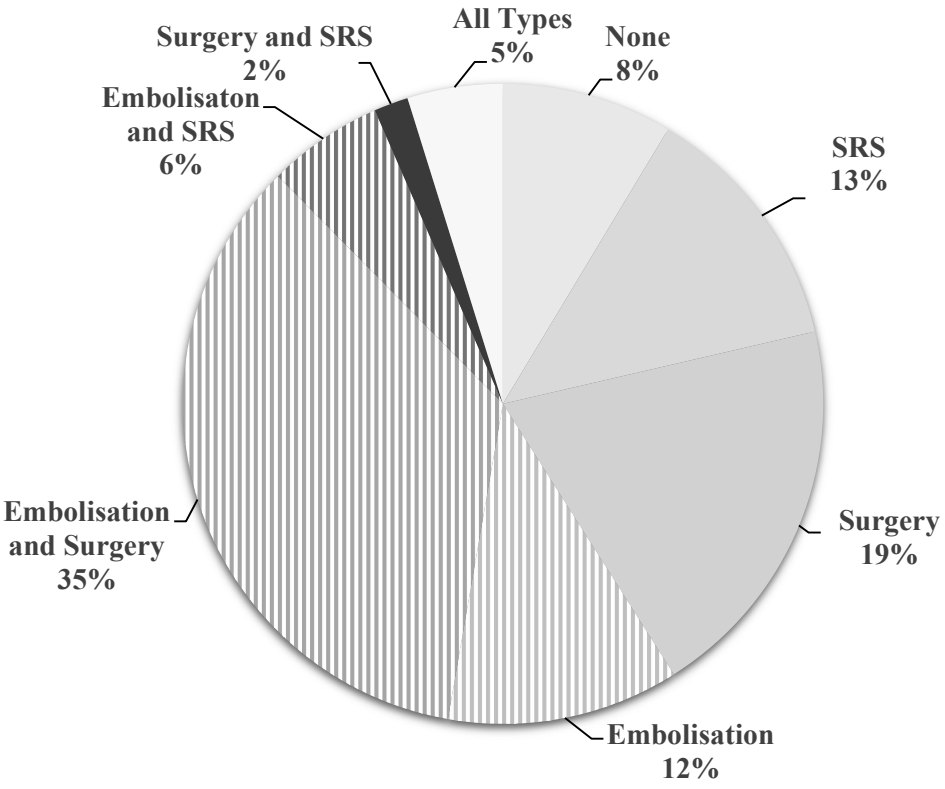

Figure 1: Distribution of AVM treatment techniques

Endovascular embolisation, as with other endovascular treatment options, is minimally invasive and reduces the risks that are generally associated with open surgery such as infection and extended recovery times. Furthermore, coil embolisation allows precise targeting and occlusion of abnormal vessels while sparing surrounding healthy tissue.

Another advantage of coil embolisation specifically, is its versatility, as it can be tailored to the patient's individual anatomy and the AVMs characteristics, offering a personalised approach to treatment. For example, where surgical resection or radiosurgery may be challenging, embolisation serves as a preparatory step, reducing the AVMs blood flow and volume, thereby minimise intraoperative bleeding and improving overall outcomes.

Transcatheter embolisation is a widely used endovascular treatment that involves delivering embolic agents, such as coils or chemicals, via a catheter to the site of a diseased vessel (Osuga *et al*, 2006). An example of a coil embolisation is illustrated and annotated in Figure 2, where a continuous coil is used for the embolisation procedure.

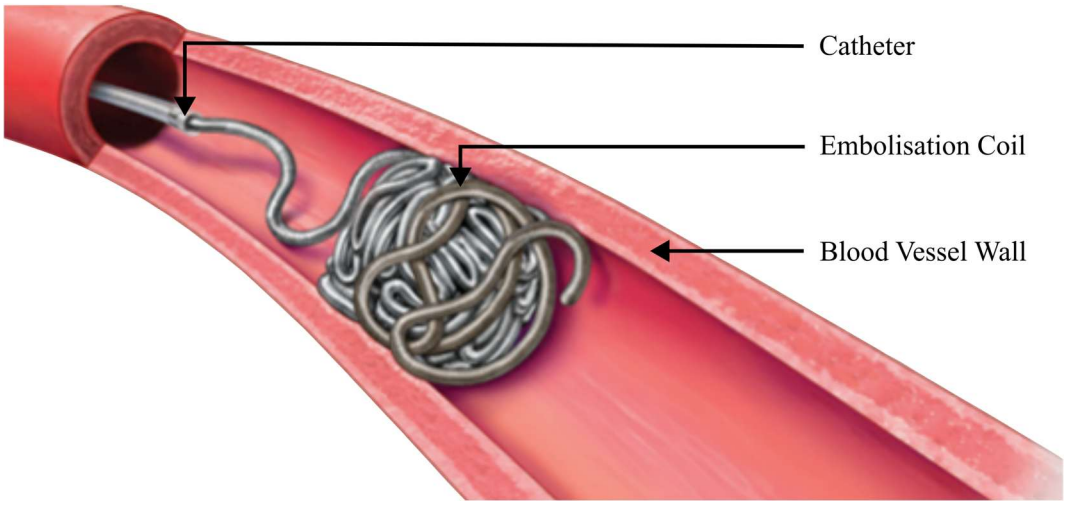

Figure 2: Transcatheter coil embolisation (Teigen, C., 2015)

Several complications are associated with endovascular procedures, including vessel wall trauma, distal thromboembolism (travelling blood clot which blocks blood flow), and vessel perforation (Wani *et al*, 2012) resulting from the pressure that the catheter applies to vessel walls. Another complication of this surgery is the inadequacy of current methods in the evaluation of a successful embolisation. The rate of recurrence for AVMs treated with coil embolisation has been purported to be as high as 25.5% in the long-term (Wani *et al*, 2012) and can be attributed to insufficient vessel embolisation. Furthermore, an AVM which has revascularized (restored blood flow) can increase the risk of haemorrhage, excessive bleeding, ulcerations, and the destruction of healthy tissue (Linh *et al*, 2022).

1.2 Research Motivation

In Africa and particularly in South Africa, the burden of vascular diseases such as AVMs is increasingly significant. Stroke, sometimes resulting from AVMs, is a leading cause of death and disability, with an estimated incidence of 244 per 100,000 people per year and an observed mortality rate of 144 per 100,000 people per year in rural South Africa (Maredza *et al*, 2015). This is compounded by limited and disparate access to advanced diagnostic and treatment technologies, contributing to a higher mortality rate compared to other regions (WHO, 2022), as well as a high prevalence of hypertension, a major risk factor for vascular diseases. The same reported that diagnostic challenges are exacerbated by a shortage of specialized medical professionals and limited availability of advanced imaging techniques, such as MRI and CT angiography, which are essential for accurate diagnosis and treatment. Moreover, economic constraints and healthcare infrastructure inequalities further hinder the effective management of AVMs, making innovative research and development in this area crucial.

Pre-surgical planning plays a crucial role in enhancing the potential for success of surgical interventions by providing clinicians with valuable insights into pathological structures and their characteristics before performing procedures. This proactive approach not only improves treatment selection but also reduces costs and increases procedural efficiency, ultimately minimising surgical time. In the context of endovascular coil embolisation for AVMs, the primary objective is to achieve complete occlusion. Despite this goal, high recurrence rates undermine the success of these procedures. Currently, there is no established quantitative framework to guide the design of effective surgical plans, leaving a gap in the ability of clinicians to objectively assess and optimise procedural success.

This research aims to address this by developing quantitative methods for pre-surgical planning that enhance the outcomes of coil embolisation. By incorporating metrics such as coil insertion parameters and flow rate reduction, this study seeks to provide an initial framework for improving procedural success rates. The lack of a quantitative relationship to inform surgical planning underscores the need for such advancements, as existing methods do not adequately support the objective evaluation of procedural effectiveness.

Emerging technologies, such as robotic arm catheter insertion, offer promising opportunities for this research. These technologies allow for the variation of coil parameters during interventions, which can be computationally extended to study their impact on embolisation outcomes. Furthermore, common AVM co-morbidities such as hypertension may also be studied computationally using parametric variation.

Leveraging these advancements, this study develops and validates a pre-surgical planning workflow, aiming to refine the accuracy and effectiveness of endovascular procedures with the ultimate goal of enabling the future development of integrated pre-surgical tools.

Addressing these gaps, this research will not only enhance the scientific understanding of AVM coil embolisation but also contribute to the establishment of new standards for pre-surgical planning. This will, in time, contribute to more successful interventions, improved patient outcomes, and a more objective assessment of procedural success. A structured motivation may be found in Figure 3.

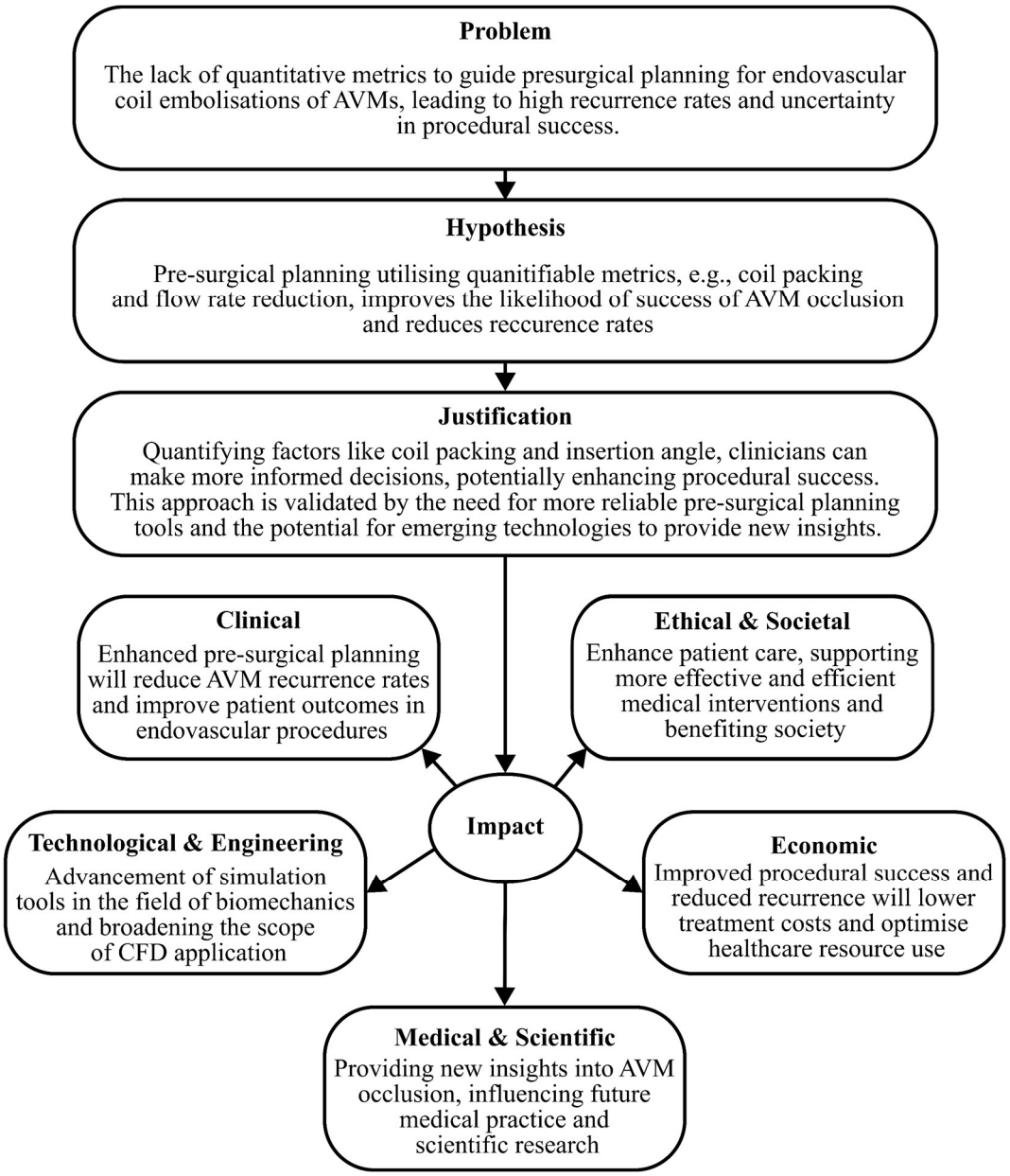

Figure 3: Research framework and motivation

1.3 Literature Review

The computational assessment of clinical interventions involves a detailed evaluation of the treatment mechanism, procedural approach, and the determination of its success within a clinical context. Furthermore, vascular interventions, such as those targeting AVMs require a consideration of physiological properties, including the complex and tortuous nature of vascular networks, blood rheology, pulsatile blood flow, and the viscoelastic behaviour of vessel walls. Additionally, the potential for thrombus (blood clot) formation and its subsequent impact on blood flow requires attention, especially when evaluating the efficacy of embolisation or other flow-diverting procedures.

Ultimately, the characteristics of the vascular system that must be accurately accounted for through computational models are dictated by the specific goals and implementation of the surgical procedure. As such, the surgical overview and dominant vascular system characteristics generally resolved through computational methods are presented here.

1.3.1 Clinical considerations

The success of an AVM coil embolisation procedure can be defined by the complete occlusion (blockage) or obliteration of the AVM. An ill-planned or unsuccessful treatment can result in AVM revascularisation and re-occurrence (Uller *et al*, 2014). Furthermore, a partial occlusion during coil embolisation has the potential to be harmful, as it may lead to increased haemodynamic stress, especially on fragile vessels, elevating pressure within the AVM and increasing the risk of rupture (de Leacy *et al*, 2022). An AVM may even be rendered proliferative from a dormant state by partial occlusion (Yakes & Baumgartner, 2014). However, the evaluation of the efficacy of an AVM coil embolisation is subjective, requiring vascular surgeons to conduct at least one of two postoperative observations:

- Visually discern if contrast agent (CA) moves through the embolised region.
- Postoperative patient monitoring for symptoms of incomplete obliteration.

As suggested in the list above, visualisation-based techniques, such as MRI and CT imaging, are integral to the clinical assessment of AVMs but are inherently limited by stochastic variation and subjective interpretation of clinical metrics. Variability in image quality, inter-observer differences, and the absence of standardised metrics can lead to inconsistent evaluations of factors such as flow dynamics and treatment efficacy.

The velocity and pressure reduction through the AVM has been employed as a means of monitoring AVM treatment by a multitude of papers in literature including Franzetti *et al* (2021) and Zhang *et al* (2020).

An example of the results of this method is shown in Figure 4, wherein a successful occlusion has been defined computationally and experimentally as when the AVM exhibits no internal flow, i.e., complete occlusion. However, this measure has not been associated with AVM intervention procedures or surgical metrics of success.

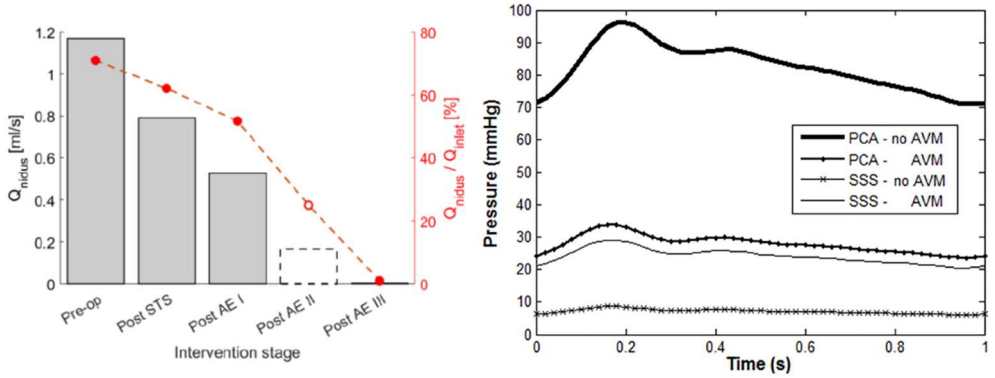

Figure 4: AVM flow rate reduction by consecutive intervention stages (left) (Franzetti *et al*, 2021) and pressure drop changes due to an AVM (right) (Zhang *et al*, 2020)

Literature concerning intra-aneurysmal flow, as published by Babiker *et al* (2013) has postulated a means by which vascular clinicians can intra-operatively quantify the degree of coil embolisation, namely coil packing density. As exhibited in Figure 5, the coil packing density is described as a percentage of the total flow volume (in this case saccular volume) occupied by the embolising coil. Also shown is that as the saccular coil packing density increases, the inlet flow vectors reduce.

Linking coil packing parameters, such as packing density and the flow reduction through the AVM requires a limiting condition which relates a known flow state to a successful procedure. Furthermore, total occlusion during a coil embolisation is strongly dependent on clotting, which will thus also need to be considered. Clot formation and growth are strong functions of blood flow shear rate as described by Casa *et al* (2017). Ultimately, an objective metric vascular surgeons can use to improve the likelihood of success of an AVM coil embolisation could be derived by relating coil packing, AVM flow and clotting.

Figure 5: Coil packing density in an aneurysmal sack (Zhang *et al*, 2020)

1.3.2 Current modelling techniques

An overview of the numerical techniques used in the modelling of the various components of the embolisation procedure and their adaptation in literature are compiled herein.

Vascular geometry modelling

Current literature on vascular flow modelling specifically relating to AVMs incorporates a variety of techniques including lumped resistance electrical network models (Zhang *et al*, 2020), *in vitro* cast and patient-specific modelling (Babiker *et al*, 2013) as well as combinations of CFD simulations and validatory experimentation (Kaneko *et al*, 2020). The data shown in Figure 6 corresponds to the latter case, wherein both the computational and experimental modelling of an arteriovenous malformation are shown.

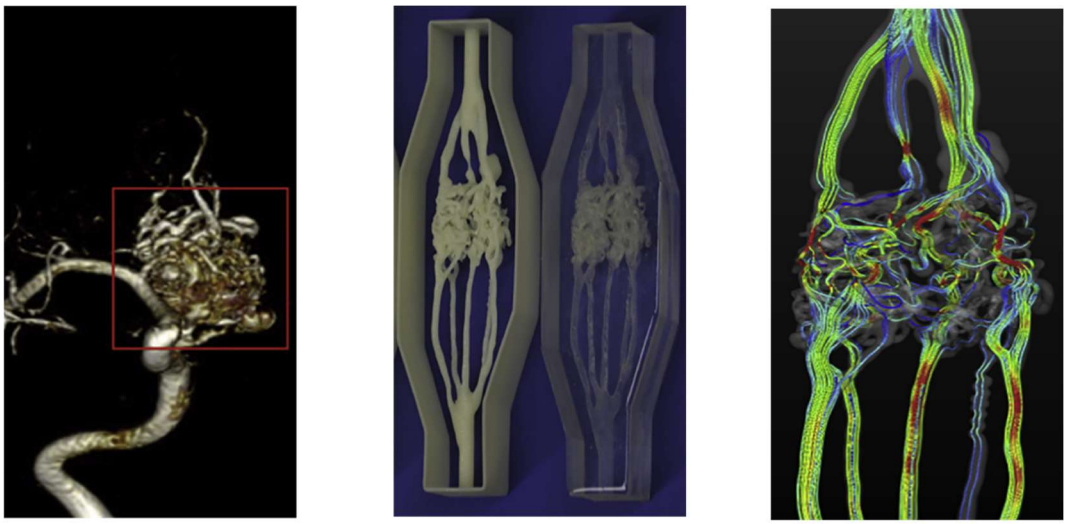

(a) (b) (c)

Figure 6: AVM flow models including (a) MRA of the AVM, (b) simplified *in vitro* casts of the AVM structure and (c) CFD simulation of the AVM geometry (Kaneko *et al*, 2020)

Figure 6, taken from Kaneko *et al* (2020), showcases different stages of the most recent vascular and AVM modelling techniques. Beginning with (a), the patient-specific geometry is derived from MR (Magnetic Resonance) imaging which allows the fabrication of (b) a simplified *in vitro* cast/print of the AVM and which also informs (c) CFD simulation of blood flow through the nidus, as highlighted using the red box in (a). Notably, such geometric simplifications are often required due to insufficient imaging resolution or field of view, e.g., in this case the patient-derived topology was scaled to a planar fabrication through the adaptation of artificial feeder arteries and draining veins.

An example of clinically relevant results from recent computational aneurysmal research is detailed in the work of Teixeira *et al* (2020), wherein a Fluid-Solid-Growth framework is presented for modelling intracranial aneurysm evolution. Combining patient-specific segmentation, CFD, and mechanobiological modelling, regions of low wall shear stress and high oscillatory flow were identified and linked to localised degradation of aneurysmal walls, the formation of secondary blebs (local outpouchings), and increased rupture risk. The results of the implementation of this framework are exemplified in Figure 7.

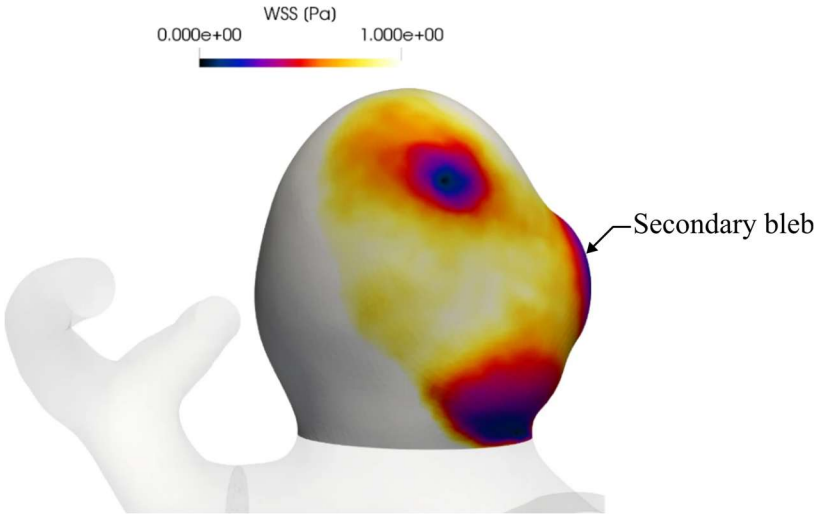

Figure 7: Localised degradation of aneurysm walls (Teixeira *et al,* 2020)

In addition, other approaches for modelling aneurysms for clinical applications are reviewed by Friesen *et al* (2021), which discusses the use of techniques including CFD, machine-learning, and deep learning-based prediction to enhance personalised treatment strategies and improve rupture risk assessment.

Embolisation coil modelling

Embolisation coil geometries are notoriously challenging to model computationally due to their intricate and convoluted shapes. Various strategies have been applied, with one common approach being the use of porous media models, in which the coil geometry is simplified into a manageable uniform porous region, as described by Umeda *et al* (2017) and Kyung *et al* (2007). In such models, the porous medium is characterised by constant porosity or resistance, providing an averaged approximation of flow resistance. Typically, the equivalent uniform porosity is calculated by assessing the pressure drop and flow rate across a known coil segment, applying equations like Darcy's to determine a mean porosity value. These models are computationally efficient and reduce memory demands, offering a practical approach for estimating flow impedance without resolving the coil structure.

However, as noted by Panneerselvam *et al* (2023), "a homogenous porous medium does not account for finer details of the coil distribution". This limitation underscores the inadequacy of uniform porosity models in capturing local variations in coil density and geometry, which can significantly affect flow patterns and shear rates within the coil region. Notably, tortuosity, reflecting the curvature and complexity of the flow paths, plays a critical role in defining high-shear regions. By accounting for porosity but neglecting tortuosity, uniform models fail to capture the pronounced curvature of streamlines near densely packed coil regions, misrepresenting shear stresses and flow resistance. This lack of spatial and geometric detail can lead to oversimplified flow predictions, limiting the model's clinical applicability, particularly for patient-specific insights into flow obstruction and clot dynamics in embolisation procedures.

Blood rheology and flow modelling

Blood cells range in size from approximately 2 (platelets) to 20 μm (white blood cells) and make up a heterogeneous fluid which behaves in a fundamentally different manner to classical Newtonian fluids. As shown in Figure 8, whole blood (blood with all its liquid and solid constituents) exhibits a non-Newtonian behaviour, whereby it does not maintain a constant viscosity with changes in shear rate. Rather, whole blood is shear-thinning and thus its viscosity reduces as shear rate increases until a point at which the trend plateaus at a viscosity of $\approx 4\ \text{mPa} \cdot \text{s}$ when the blood flow shear rate approaches $200\ \text{s}^{-1}$.

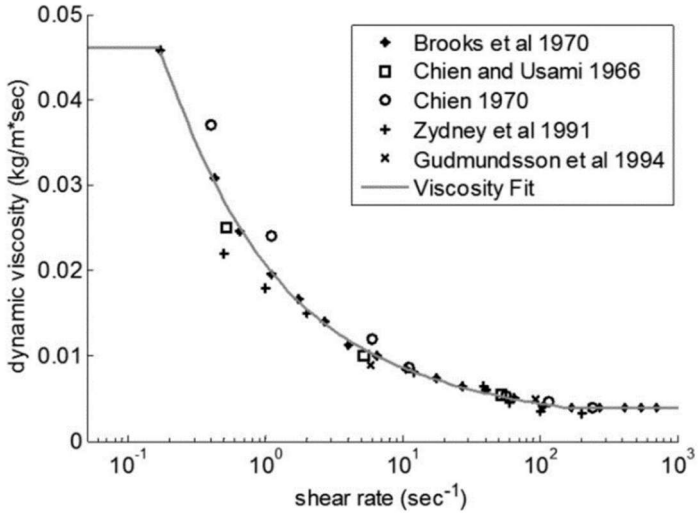

Figure 8:The general non-Newtonian, shear thinning behaviour of whole blood (Cherry & Eaton, 2013)

Patient-specificity is a pre-requisite for obtaining useful data for individual patients due to the highly tortuous and distinct nature of AVMs, however the effect of considering both pulsatile blood flow as well as non-Newtonian blood rheology with respect to AVM modelling is largely untried.

Figure 9 elucidates the typical effect of including both of these vascular flow characteristics individually, when they have been investigated in general vascular flow literature. Figure 9 was derived by comparing flow measurements which were distinguished only by the inclusion of pulsatile flow, when the flow was otherwise steady or non-Newtonian blood rheology, when the flow was otherwise Newtonian.

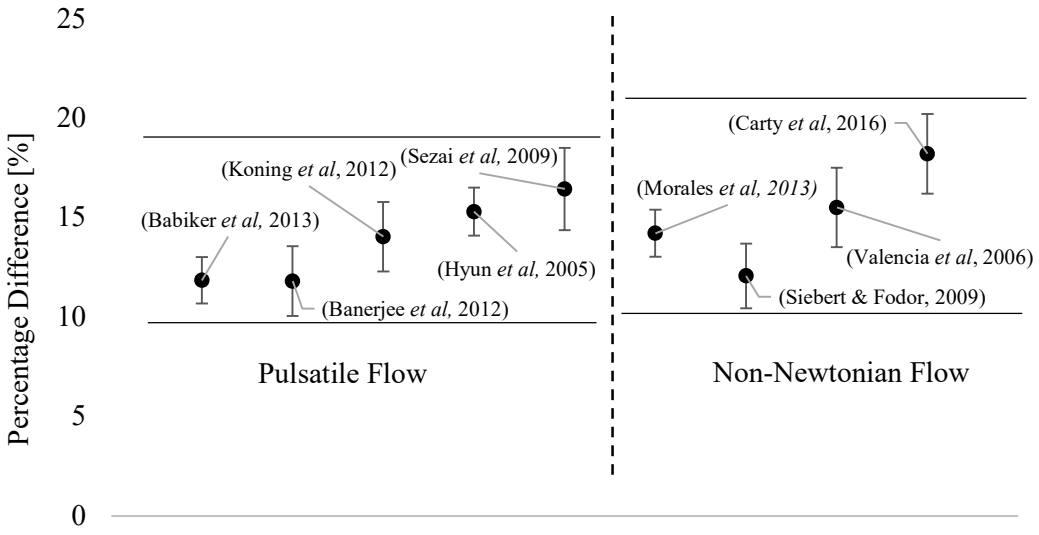

Figure 9: Average flow variation due to pulsatile and non-Newtonian flow modelling

From Figure 9, the result variation due to the inclusion of pulsatile flow is approximately between $10-17\%$, which is similar to that for the inclusion of non-Newtonian flow $11-20\%$. Thus, while the effects of these mechanisms are different, they are of comparable magnitude. These variations serve to contextualise and enhance the interpretation of the data produced by this study, highlighting the influence of flow assumptions on the results.

Vessel wall elasticity and compliance

Another pertinent vascular system parameter is vasodilation (Lowe *et al*, 2024). Vasodilation, the widening of blood vessels, as well as vasoconstriction, the thinning of blood vessels, are both mechanisms by which the blood vessel lumen (hollow passageway for blood flow) changes in size in response to variations in temperature or blood pressure. The modelling of vasodilation involves complex structural and fluid analysis, such as fluid structure interaction (FSI).

Figure 10 depicts a comparison between a rigid CFD formulation and an FSI formulation of the velocity profile through a carotid artery bifurcation (Lopes *et al*, 2019).

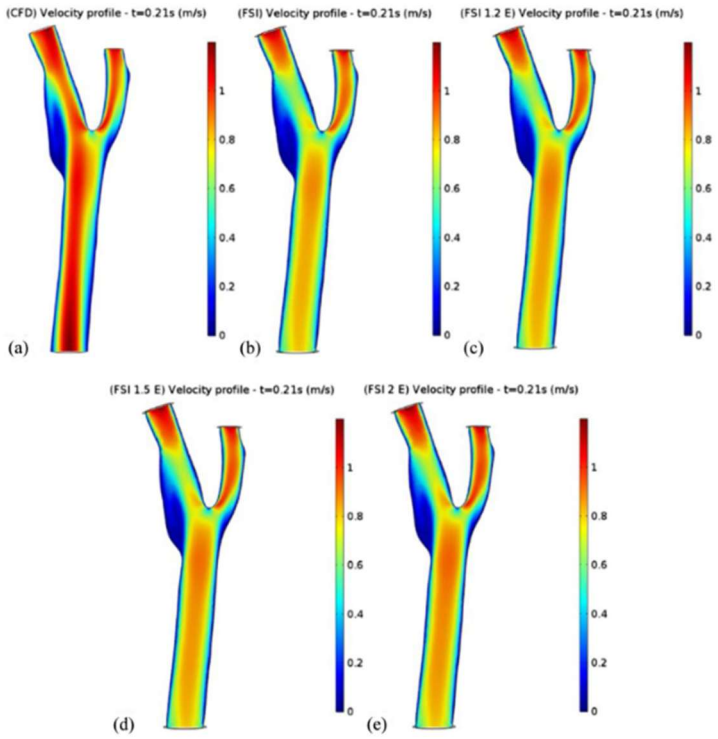

Figure 10: Rigid CFD and elastic FSI models of carotid artery bifurcation

As illustrated in Figure 10, the tendency of the rigid model is to overestimate velocity magnitudes due to its inability to account for vessel compliance. By assuming a fixed lumen size, the rigid model restricts the flow area, resulting in artificially elevated flow velocities. In contrast, the FSI model incorporates vessel wall flexibility, allowing the lumen to expand resulting in more realistic lower velocities.

This finding aligns with the results of Siogkas *et al* (2015), which demonstrate through *in vivo* pressure measurements that rigid models consistently overestimate pressure, whereas FSI models show improved agreement with physiological values. Hence, both studies thus support that FSI modelling provides a more realistic representation of vessel mechanics, accurately capturing both flow and pressure dynamics. It should be noted however that FSI approaches are computationally expensive and need to be considered in light of their computational resource requirements.

Rigid AVM models will likely exhibit a similar pattern in that the neglect of vasodilation and vasoconstriction will result in an increase of the flow velocity through the feeder arteries and AVM.

Thrombosis mechanisms and computational modelling

The computational modelling of thrombosis is a well-established field of research consisting of various numerical strategies, which may be broadly categorised into system level, continuum, discrete particle and multiscale methods. For the purposes of this study, continuum models of clot formation will be considered, which typically simulate clot growth by considering biochemical interactions of blood components, transport mechanisms and haemodynamic parameters (Yesudasan & Averett, 2019) to varying degrees of complexity. These models typically range from simplified haemodynamic formulations to complex routines accounting for the entirety of the coagulation cascade and several inter-related biochemical components, their reactions and flow processes.

The most common flow parameter utilised for thrombus modelling is shear rate and/or shear stress which is typically included to assess the possibility of clot genesis, formation and stability (Sakariassen *et al*, 2015; Li *et al*, 2014). Shear rate is a crucial variable in thrombus formation as it combines the effects of velocity gradients, wherein high gradients and thus high shear inhibit clot formation and increase the potential for clot lysis and more specifically fibrinolysis, the process of breaking down blood clots (Diamond, 1999). Alternatively, low shear environments are conducive to thrombus genesis and proliferation as these are associated with higher residence times (the amount of time blood remains in a specific region) as well as clot growth due to greater localised coagulant concentrations.

Purely haemodynamic models utilise the relationship between thrombus formation and shear to parameterise clot growth as a function of different shear rate regimes, as presented in Jafarinia *et al* (2022). Building on this, continuum models, such as those developed by Ngoepe & Ventikos (2016), include the transport mechanisms, biochemical concentrations and reactions in the final pathway of the coagulation cascade, e.g., thrombin, fibrinogen and fibrin in addition to shear rate.

Finally, two-phase continuum models allow for the simulation of influential blood coagulants as well as platelet deposition and interaction by including these platelets as a secondary solid phase. Such models are presented in Li *et al* (2014) and Du *et al* (2020). An example of the thrombus formations achieved via such two-phase continuum models and the resulting impact on flow in a cylindrical tube is shown in Figure 11 (Du *et al*, 2020), where it is evident that the presence of the clot results in a reduction in flow velocity as well as a redirection of flow around the thrombus. This substantiates the need for the replication of clotting effects in the context of embolisation models, as thrombus growths will increase the overall resistance to flow in an injured vessel that has been embolised.

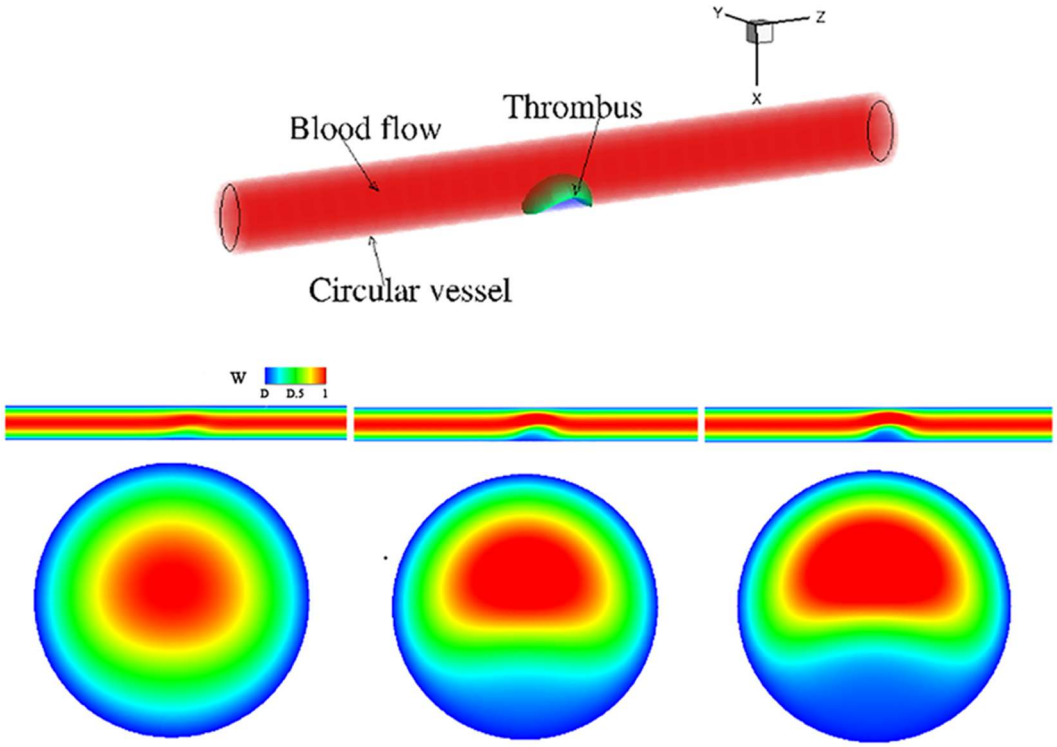

Figure 11: Two-phase model of thrombus formation in pipe flow

1.4 Data Sources and Dissertation Structure

Throughout this work, three primary external data sources serve as inputs for the computational modelling and experimentation. The geometric data for the AVM is derived from patient CT imaging provided by the Donald Gordon Medical Centre (DGMC), collected under ethics code M210728. The discrete modelling of embolisation coil geometries inserted into the computational flow domain was contributed by collaborators at the Technical University of Munich (TUM), led by Prof. Barbara Wohlmuth, Chair of Numerical Analysis. Additionally, training and data collection relating to MRI velocimetry was undertaken at the University of Twente, Netherlands (UT) under the guidance of a specialist in magnetic detection and imaging, Dr. Frank Simonis. Figure 12 provides a schematic overview of the dissertation structure, illustrating how each data source is integrated throughout the text.

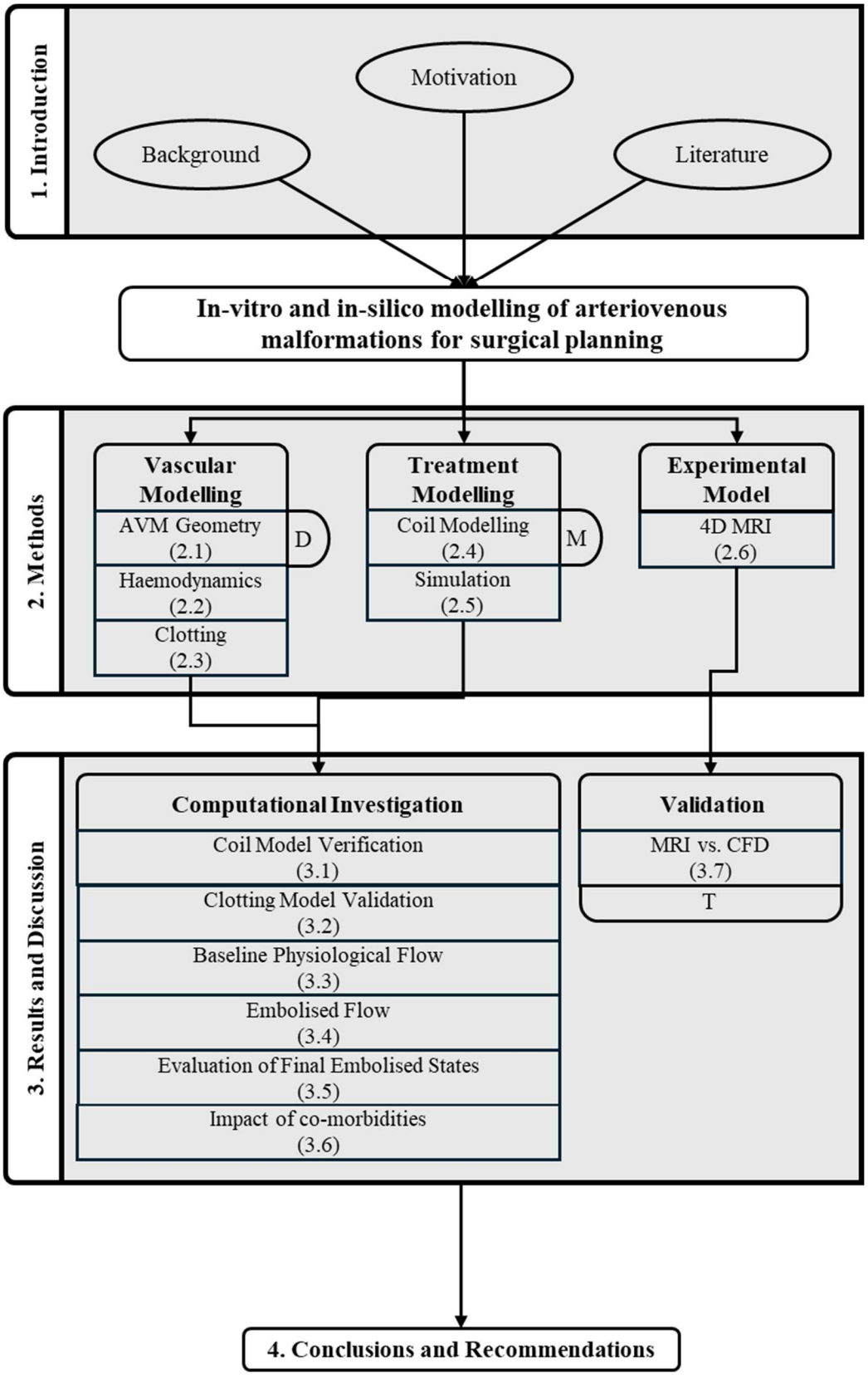

Figure 12: Dissertation structure

(Sources: D – DGMC, M – TUM, T – UT)

1.5 Delimitations

Coil embolisations typically exhibit high shear flow, specifically near the coil, resulting in platelet-dominated clotting (Casa *et al*, 2017). This research models clotting without simulating biochemistry or platelet interactions, focusing instead on a simplified approach using shear rate as a proxy for clot formation. While this method is generalised and neglects individual biochemical differences, it is adequate for the study's objectives, which target a broader understanding of embolisation outcomes rather than patient-specific details.

This study evaluates end-stage clotting behaviour under constant (plug) flow conditions, emphasizing the final clot structure rather than the dynamic clot formation. This approach is particularly relevant given that the focus lies in investigating the stabilised configurations of the clot rather than its evolution. The limitations of the shear-based clotting model, developed for this work, further justify the exclusion of time-dependent flow behaviour. As the model lacks an inherent time scale, it is unable to simulate time-resolved clotting, thus it is unsuitable for capturing dynamic clot evolution under pulsatile and steady conditions.

Moreover, the location of the pathology under investigation, the calf, and the nature of AVMs support the use of steady flow in this context. In peripheral regions such as the calf, the pressure generated by the heart is significantly dampened as blood travels away from the aorta, resulting in a diminished pulsatile component in the flow. This pulse reduction is further amplified by the unique anatomy of AVMs, which couple arterial and venous flows, creating a complex vascular connection where pulsatile energy is largely dissipated as the primary time-varying flow component is carried away via the arterial parent vessel.

The incorporation of vasodilation into the computational model requires time-dependent fluid-structure interaction (FSI) analysis, which involve considerations of anisotropic elasticity, variations in vessel wall thickness, and the interaction between the different vessel wall layers. These factors would increase the computational burden and are not integrable given the inherently time-independent nature of the shear rate clotting model.

Furthermore, while Gao *et al* (1997) indicates that vasodilation can alter flow velocities by approximately 30%, the complexity of both experimental and computational modelling of vasodilation renders it impractical for this research. As this study represents a pioneering effort in modelling AVM treatment interventions, the inclusion of vasodilation is deferred to future research. For this initial exploration, a more controlled environment with constant flow conditions is prioritised to establish foundational insights.

2 METHODS

2.1 Geometry Definition and Generation

The AVM case investigated in this work, derived from pre-operative CT imaging sourced from the DGMC as mentioned in Section 1.4, is classified as a Yakes Type I peripheral malformation, i.e., a single artery extends to a single vein, and it is located outside of the nervous system, in the left calf. The only distinction between this AVM case, as shown in Figure 13, and the classification description is the presence of an aneurysmal or swollen zone. The feeder vessel was easily identified as a named artery, specifically the posterior tibial artery, while the venous side of the AVM was more difficult to visually discern even with the use of segmentation (digital isolation and three-dimensional reconstruction), however it is known that the named draining vein in this area is the anterior tibial vein. The location and structure of the AVM is shown in Figure 13.

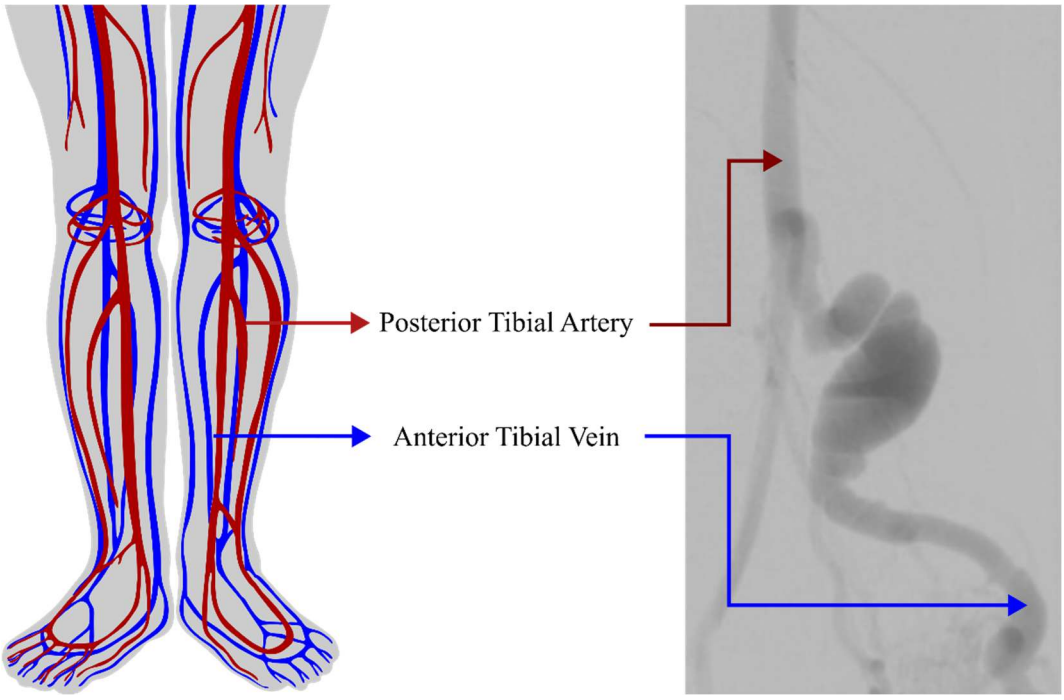

Figure 13: Arteries and veins of the lower legs (left) (Lezak & Varacallo, 2022) and patient CT scan derived from the DGMC (right)

Regarding the geometry generation, segmentation software, namely 3D Slicer was used to identify and delineate surfaces through CT contour boundary selection based on units of radio density known as Hounsfield units (HU), while CAD software was used to revolve sections of the geometry and ensure that the segmented portions were valid structures.

Using this combination of segmentation and CAD techniques two geometries were generated. The primary computational geometry includes the malformation and feeder vessels. The arterial inlet vessel was determined to have a 3 mm diameter during the initial scan in agreement with literature such as (Yi *et al*, 2021), while the venous size was taken to be the average diameter of the anterior tibial vein, i.e., 5.22 mm (Lorbeer *et al*, 2018).

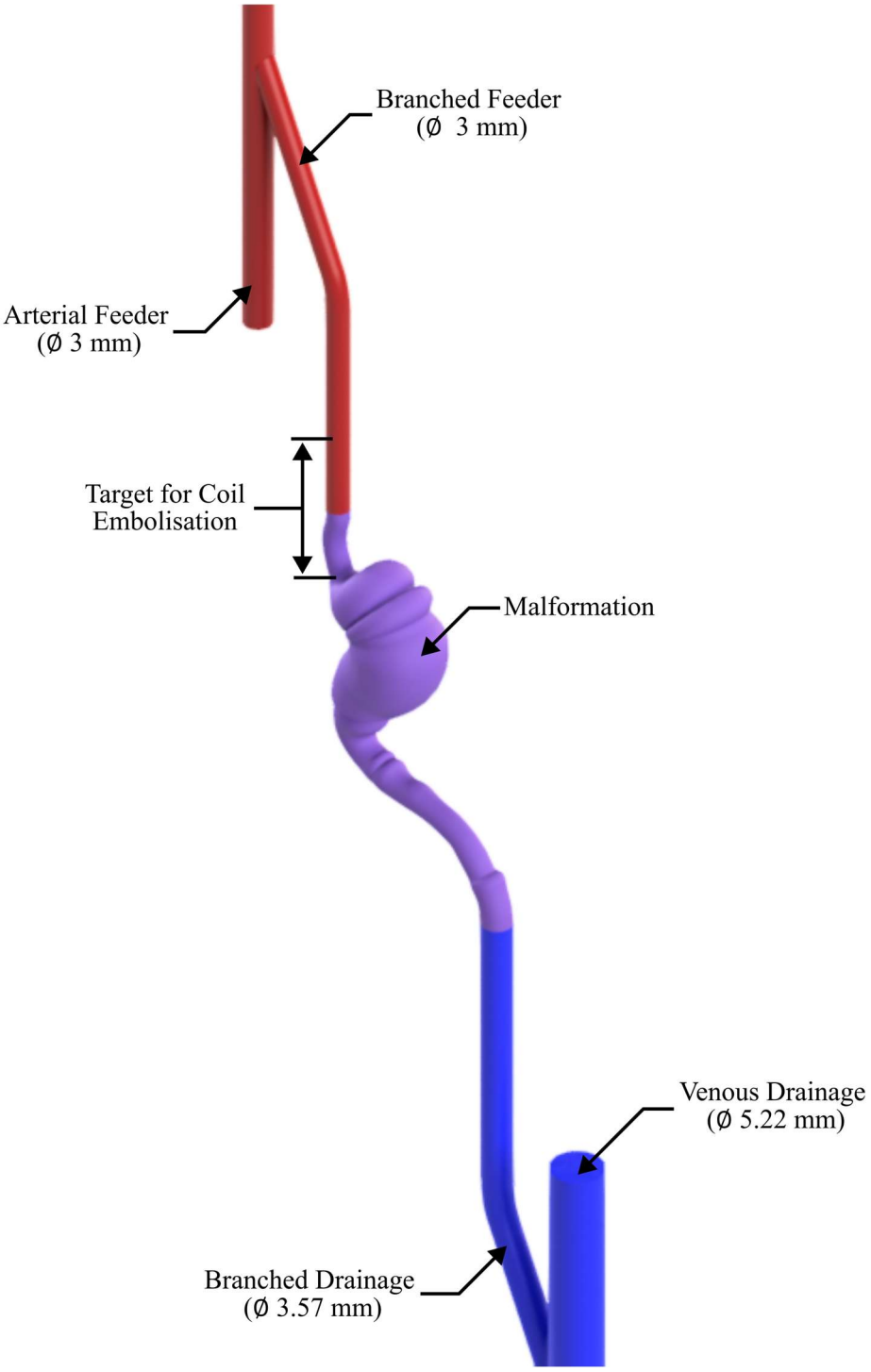

Figure 14: Primary computational geometry

A secondary geometry was generated to be used for experimental validation, shown in Figure 15. Significant differences include downscaling, the removal of the parent vessels and a slight narrowing of the aneurysmal zone. These changes are discussed in section 2.6.3, but it is in consideration of the experimental equipment and its constraints.

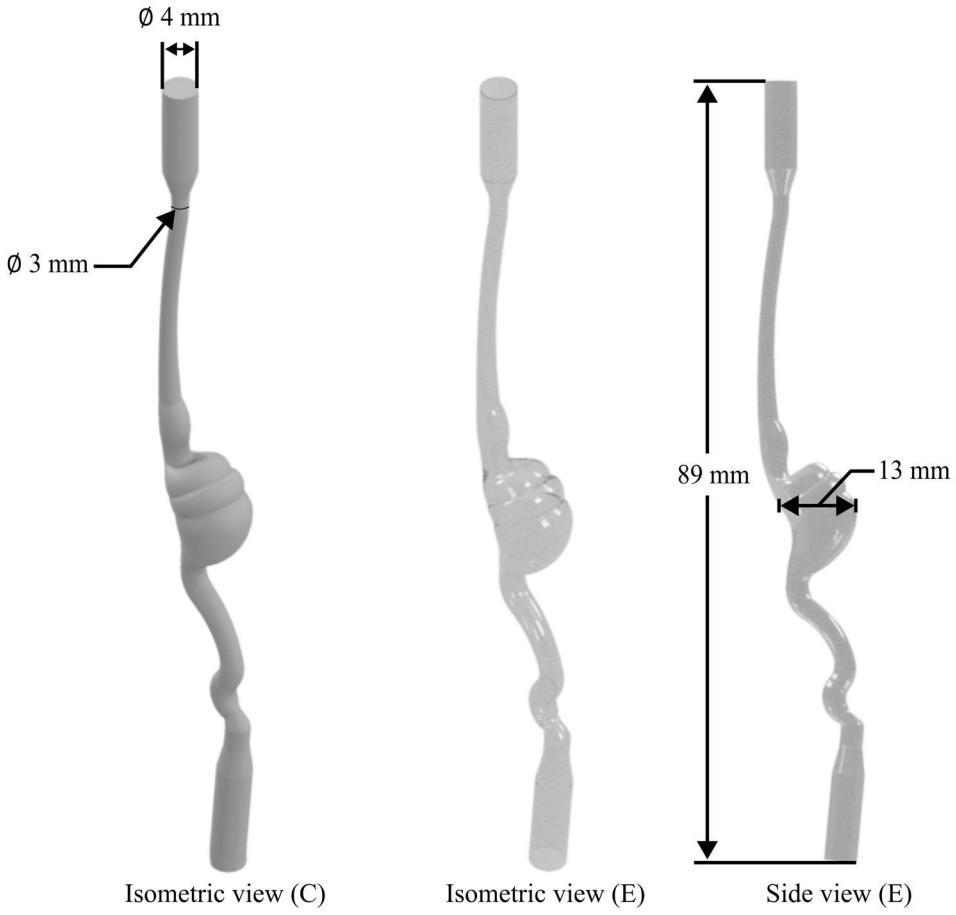

Figure 15: Secondary geometry – Computational (C) flow domain (left) and experimental (E) flow boundary (right)

This secondary geometry was created for 3D printing through the use of a Formlabs Form 3 Stereolithographic (SLA) printer (Formlabs, United States), specifications of which may be found in Appendix A. These printed models were subsequently used in two distinct experimental regimes. The first experimental series was conducted for the purposes of characterising the resistance associated with embolisation coils (section 2.3), while the second series took the form of a computational verification through the application of 4D Magnetic Resonance Imaging, also known as MRI velocimetry (section 2.6).

This model was designed to enable press fits with silicon tubing with an interior diameter of 4 mm, hence the cylindrical extrusions evident at both the inlet and outlet ends.

The flow domain of the AVM is subsequently divided into four distinct zones:

1. Arterial Zone
2. Coil Zone
3. Aneurysmal Zone
4. Venous Zone

This classification enables the application of targeted control measures, particularly concerning coil insertion and clot formation. For example, the modelled clot formations were limited to have their origin in the "Aneurysmal Zone" as discussed in section 2.4.2. The division of these zones, along with the relevant enforced flow directions, is depicted in Figure 16. The enforced flow directions were determined based on the relative direction of arterial and venous flows and the orientation of the AVM.

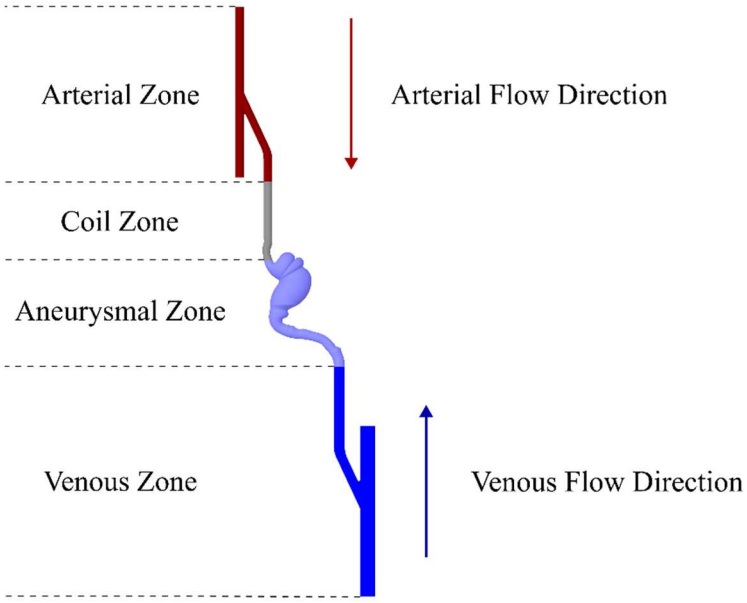

Figure 16: Zone definition and allocation

2.2 Experimental and Computational Material Description of Whole Blood

As previously discussed, whole blood exhibits non-Newtonian (shear-thinning) behaviour, where its viscosity decreases with increasing shear rate. While a common approach in literature is to model blood as a Newtonian fluid with a constant viscosity of $4\ mPa \cdot s$, coil embolisation procedures involve significant variations in the local AVM shear rate from the associated abrupt changes in flow velocity and the flow field geometry due to both coiling and clot formation. These variations in local shear necessitate a more accurate replication of blood's non-Newtonian properties for reliable modelling in these contexts.

2.2.1 Experimental technique for non-Newtonian blood flow Analysis

The shear-thinning behaviour of blood was parameterised using the curve shown in Figure 8, which served as the baseline for all non-Newtonian modelling across both computational and experimental regimes. This curve was derived from trends observed in human whole blood, synthesized from multiple studies. The resulting dataset, representing the dynamic viscosity changes across a range of shear rates, is hereafter referred to as "True blood" and provides a physiologically accurate foundation for the following rheological analyses.

Following on from work published by Perrira *et al* (2022), a fluid was created which is capable of mimicking the shear-thinning nature of whole blood. This fluid, termed the blood mimicking fluid (BMF), is a mixture of distilled water, xanthan gum and glycerol. The synthesis of an accurate blood-replicate came about by means of rheological testing using an AR 2000 rheometer (TA Instruments, United States), detailed in Appendix B, wherein the viscosity of the fluid was measured during shear rate cycles of between 0 and 1000 Hz. A sample of the results for the total of 36 mixtures tested has been given in Figure 17 along with their compositions as Distilled Water – Glycerol – Xanthan Gum by weight percentage. The corresponding R^2 and critical shear rate values are shown in Table 2.

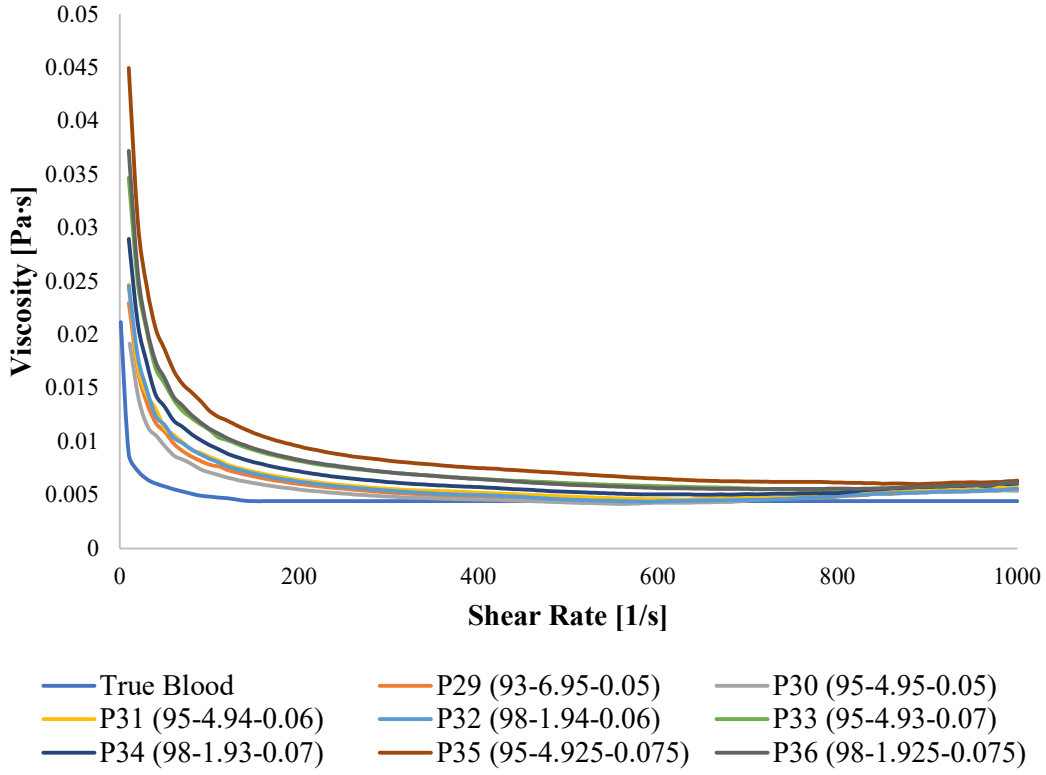

Figure 17: Results of samples 29 through 36 and their comparison with True Blood

Table 2: Compositions and R^2 values for tested BMF samples

Sample	R^2	Critical shear rate [s^{-1}]
29	0.948	610
30	0.942	570
31	0.942	630
32	0.944	600
33	0.944	790
34	0.881	720
35	0.941	900
36	0.943	820

The R^2 values were derived based on the deviation of each viscosity-shear curve from that of True Blood and was the dominant metric for BMF selection, however the critical shear rate which marked the onset of turbulence was also considered as a secondary metric. As a result, sample 33 was selected as the optimal BMF mixture, as it had one of the best overall comparisons with true blood with an R^2 value of 0.944 as well as a delayed critical shear rate of 790 s^{-1}, which is not expected to be exceeded in the corresponding experiments.

As shown in Figure 18, the BMF viscosity is generally greater than that of whole blood, however the difference was taken to be acceptable as the BMF mixture was thinned as much as possible without reducing critical Re to impractically low levels. Furthermore, at the expected average shear rate of 180 s^{-1}, True Blood demonstrates significant thinning, which motivated the use of the BMF as opposed to Newtonian fluids like water. Notably, the BMF replicated the flow dynamics of blood for verification purposes, with the computational material model matched to the BMF curve rather than that of True Blood.

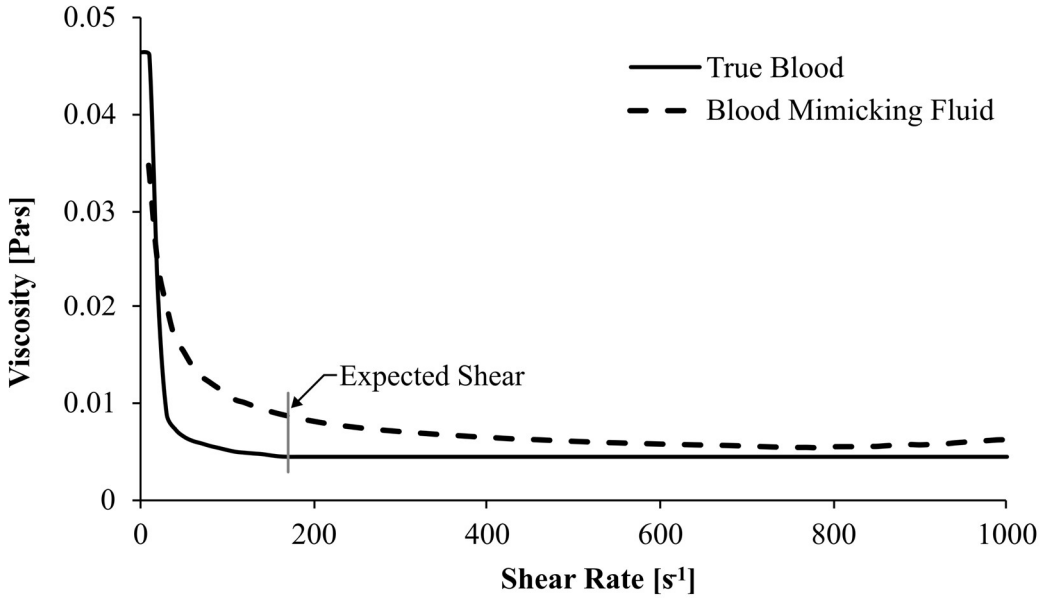

Figure 18: Final BMF mixture compared to the True Blood curve

2.2.2 Non-Newtonian computational models and parameterisation

There are a number of models available for replicating the shear-thinning behaviour of blood in the ANSYS Fluent (Ansys, United States) solver used for this work. The non-Newtonian power law, Cross, and Carreau-Yasuda models were tested to evaluate their applicability and stability in embolisation scenarios. Ultimately, the Carreau-Yasuda model was selected as the ideal choice, as shown in Eqn 1 (Jalali *et al*, 2020), because it offers greater flexibility in capturing blood's viscosity across the tested shear rate spectrum and thus a more precise replication. Its improved numerical stability arises from improved handling of viscosity at higher shear rates, while ensuring consistency at the lower shear rates typical in embolisation cases.

$$\eta = \eta_\infty + (\eta_0 + \eta_\infty)[1 + \gamma^2\lambda^2]^{\frac{n-1}{2}} \quad \ldots\ldots\ldots\ldots 1$$

where η is the fluid viscosity [Pa · s], η_∞ is the limiting steady state viscosity at high shear rates or infinite viscosity [Pa · s] and η_0 is the limiting steady state viscosity at low shear rates or near-zero viscosity [Pa · s]. λ is the characteristic time or consistency [s], i.e., it is the inverse of the shear rate at which the fluid transitions from Newtonian to power-law behaviour and lastly n is the power law index which describes the rate of shear-thinning during the power law behaviour of the fluid.

Two distinct sets of these parameters were formulated, which pertain to the True Blood curve given in Figure 8 as well as the final blood mimicking fluid viscosity-shear curve as shown in section 2.2.1. These parameter sets are given in Table 3.

Table 3: Carreau-Yasuda model parameters

Parameters	True blood	BMF
$\eta_\infty\ [mPa \cdot s]$	4.41	5
$\eta_0\ [mPa \cdot s]$	46.5	35
$\lambda\ [s]$	6.12	6.12
n	0.27	0.2

Viscosity in this model is treated as a function of shear rate alone, based on the assumption that body temperature variations in AVM cases are minimal. Although chronic inflammation associated with AVM development has been shown to potentially elevate local temperatures (Cox *et al*, 2014), the degree of this effect is influenced by case-dependent factors such as inflammation severity and in some cases, there is no measurable change in temperature (Onciu *et al*, 2024). Furthermore, such localised variations are relevant to tissue-level phenomena, hence they fall outside the scope of this study.

The shear rate-dependent variation in viscosity, is illustrated in Figure 19. The regions outlined in black are areas of anticipated recirculation within the AVM, where low shear rates are predicted, leading to higher viscosity as expected in such stagnant zones. This nuanced approach enhances the fidelity of the velocity and pressure field calculations, particularly in capturing the complex haemodynamics of AVMs.

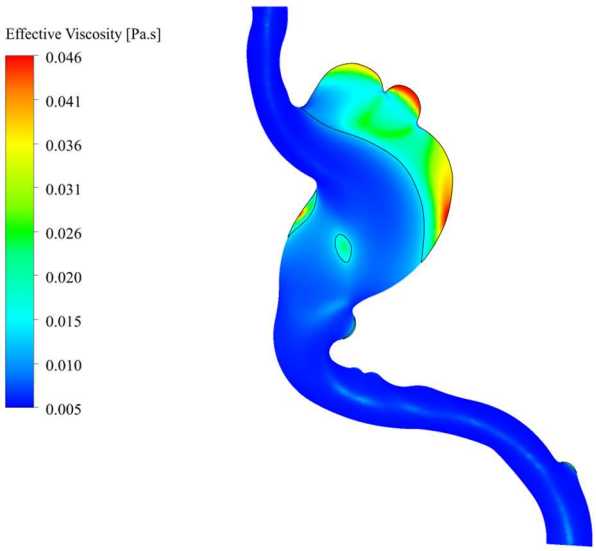

Figure 19: Variation of fluid viscosity with shear rate

2.3 Embolisation Coil Modelling

The coils used as the basis for the implantation model are the Cook® Medical MReye® Embolisation Coils sourced from the DGMC as shown in Figure 20. The AVM case presented utilises a coil scoped to be inserted into the region designated as the "Coil Zone" in Figure 16. The coil has a diameter of 0.889 mm and a coiled diameter of 4 mm.

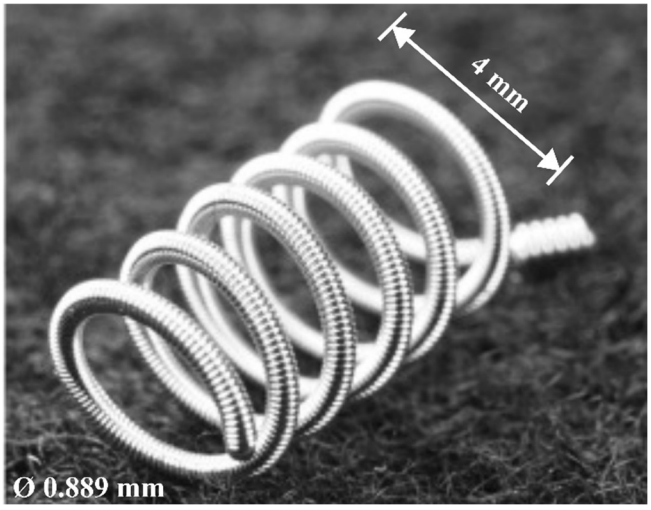

Figure 20: MReye® embolisation coils (Trerotola *et al*, 2019)

2.3.1 Uniform porosity modelling

Variable pressure head flow tests enabled the derivation of the flow resistance (k – values) associated with the embolising coil, through the application of the simplified Darcy-Weisbach equation, given in Eqn 2.

$$\Delta P = kQ^2 \quad \ldots\ldots\ldots\ldots 2$$

Figure 21 depicts the flow rig used to ascertain these values, as well as an image of the printed AVM model with the inserted coil in the upper right corner. z_1 refers to the height of the fluid within the reservoir, which may be adjusted to provide a variable pressure head, while z_2 refers to the height at which the outflow rate is determined.

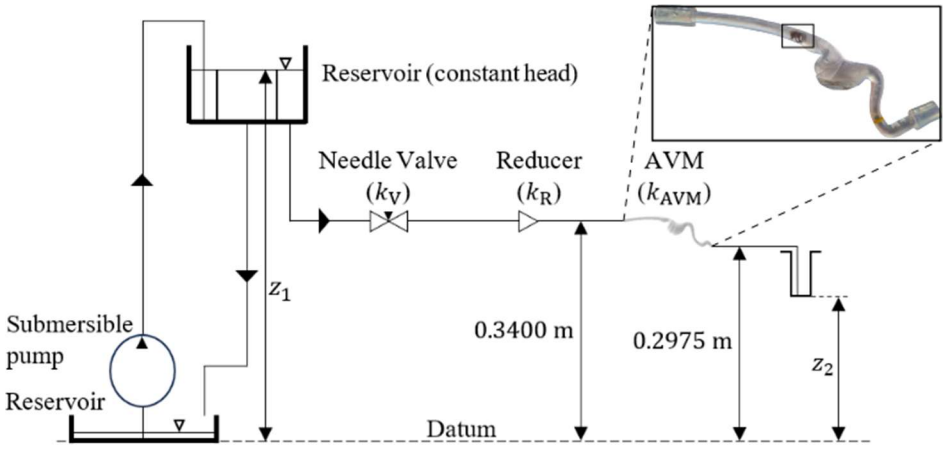

Figure 21: Variable pressure flow rig setup (Bougardt *et al*, 2024)

Tests at various inlet pressure heads were conducted to determine the flow resistance associated with the embolisation coil. Through the comparison of the flow rates in the open system (pre-coiled) and the embolised system, the additive nature of flow resistance values within the system allowed for the isolation of the k value associated with the embolisation coil. The corresponding formulations are presented in Eqns 3 and 4.

$$\Delta P_{\text{open}} = \left(k_{\text{p}} + k_{\text{v}} + k_{\text{r}} + k_{\text{AVM}}\right)Q_1^2 \quad \ldots\ldots\ldots\ldots 3$$

$$\Delta P_{\text{embolised}} = \left(k_{\text{p}} + k_{\text{v}} + k_{\text{r}} + k_{\text{AVM}} + k_{\text{coil}}\right)Q_2^2 \quad \ldots\ldots\ldots\ldots 4$$

As demonstrated in Eqns 3 and 4, the flow resistance value associated with the embolisation coil (k_{coil}) may be computed through subtraction of the total flow resistance for the embolised and open systems. Figure 22 illustrates the k value derivation from the gradient of the ΔP vs Q^2 plots.

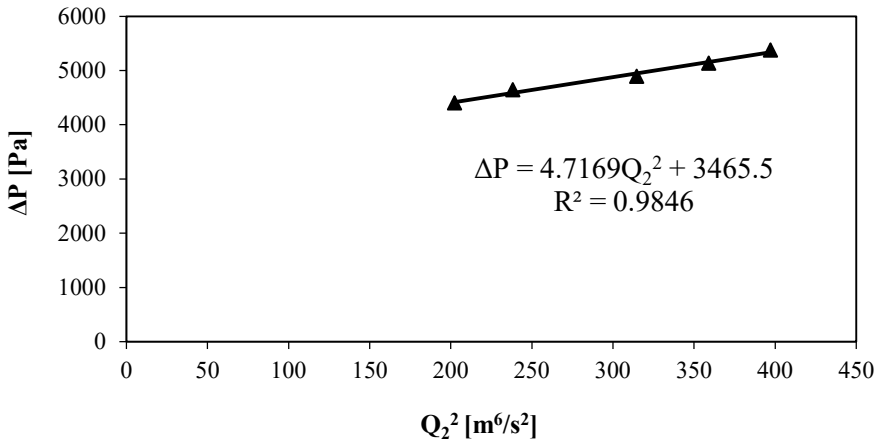

Figure 22: Flow resistance (k) derivation for the embolised system

The accuracy of the derived flow resistance values was determined by way of simulation, through the introduction of a porous zone and thus a momentum sink in the volume denoted as the "Coil Zone" in Figure 14. The momentum sink was tuned through the use of an inertial resistance coefficient, derived through application of the continuity equation and the manipulation of momentum terms in the governing equations, wherein the v^2 term in Eqn 5 allows for direct comparison with the inertial resistance coefficient term, neglecting the viscous resistance coefficient. This relationship is summarised in Eqns 5 and 6:

$$\Delta P = 735{,}071.4518 v^2 = S_{\mathrm{i}} \quad \ldots\ldots\ldots\ldots 5$$

$$S_{\mathrm{i}} = \frac{1}{2} C_2 \rho v^2 \Delta n \quad \ldots\ldots\ldots\ldots 6$$

where S_{i} is the momentum sink term $[\mathrm{kg} \cdot \mathrm{ms}^{-1}]$, C_2 is the inertial resistance coefficient $[\mathrm{m}^{-1}]$, ρ is the fluid density, which in this case is water $[\mathrm{kg/m}^3]$, v is the physical velocity of the flow through the coil $[\mathrm{m/s}]$ and $\Delta\mathrm{n}$ is the length of the coil in the flow-wise direction $[\mathrm{m}]$. The results of a validation exercise performed for this technique may be found in section 3.1.1.

In summary, using a uniform porosity field to model the coil provides a simplified approximation of flow but has inherent limitations due to its inability to capture the detailed structure of the coil. This approach assumes a homogenous distribution of flow resistance throughout the coil region (the bounding volume of the coil), which neglects the spatial variability in flow paths and obstructions created by the coil's physical geometry. As a result, the uniform porosity model may inaccurately represent local variations in velocity and pressure due to the neglect of the coil structure.

2.3.2 Non-uniform porosity modelling

Background on modelling coil geometry

As outlined in section 2.3.1, employing a uniform porosity field to model the coil provides an approximation of its flow impedance. However, this approach oversimplifies the coil's complex geometry. Given the influence of coil geometries on local flow structures and downstream flow, accurately capturing these interactions is crucial for understanding embolisation. The coil's intricate shape induces localised changes in velocity, pressure and shear rate, the latter of which plays a critical role in clot formation and stability.

To address these limitations, this study adopts a non-uniform porous media model, which provides a detailed representation of the complex flow behaviour surrounding the coil. While this approach incurs a slightly higher computational cost than the uniform porous media model, it remains more efficient than modelling the coil as a solid. This balance between computational efficiency and accuracy make the model better suited for replicating nuanced flow interactions, enabling closer approximations of *in vivo* conditions, improving predictions of clinical outcomes, and informing the optimisation of coil implementation for effective AVM treatment.

The necessity for capturing and replicating the inserted coil structure led to a collaboration with the Technical University of Munich (TUM), specifically with Prof. Barbara Wohlmuth's Group in the Chair of Numerical Analysis. The group has developed a method for modelling embolisation coils and their insertion into biological vessels using Discrete Elastic Rod (DER) theory.

The governing equations in DER theory are derived from the balance of forces and moments along a rod's length. The Kirchhoff equations, which govern the equilibrium of the rod, are given by:

$$\boldsymbol{F}' = 0\,, \boldsymbol{M}' + \boldsymbol{r}' \times \boldsymbol{F} = 0 \qquad \ldots\ldots\ldots\ldots 7$$

where **F** is the internal force vector, **M** is the internal moment vector and **r** is the position vector along the centerline of the rod.

Numerically, Eqn 7 is applied to the discretised rod, i.e., it is applied at each node along the length of the rod and accounts for both its bending and twisting, which requires formulations for the energy associated with both of these variables.

The total elastic energy E of an inextensible rod, like an embolisation coil, is derived from its bending and twisting energies, omitting the stretching component due to the inextensibility assumption as shown in Eqn 8.

$$E = E_{bend} + E_{twist} \quad \ldots\ldots\ldots\ldots 8$$

In the context of DER theory, the centerline $\boldsymbol{\gamma}(\mathrm{s})$ represents the central curve of the rod, parameterised by the arc length s, which serves as the reference for the rod's geometry.

Along this centerline, a material frame $\{\boldsymbol{t}(\mathrm{s}), \boldsymbol{m_1}(\mathrm{s}), \boldsymbol{m_2}(\mathrm{s})\}$ is attached, which is an orthonormal frame where $\boldsymbol{t}(\mathrm{s}) = \boldsymbol{\gamma}'(\mathrm{s})$ denotes the tangent vector and $\boldsymbol{\kappa} = \boldsymbol{t}'$ is the centerline's curvature (normal) vector (Bergou *et al*, 2008). The DER model is subsequently extended to include collision and intersection algorithms, applied at the boundary of the material frame, which allows for the simulation of the self-collision of the coil as well as its interaction with the surrounding vessel walls. This allows for the replication of the real-world conditions of coil deployment during embolisation procedures.

The DER model developed by TUM, as detailed for aneurysmal cases in Frank *et al* (2024) and Holzberger *et al* (2024) has been directly applied to simulate the configuration of embolisation coils within the AVM under investigation. Six different embolisation coil geometries and packing conditions are considered, wherein the number of inserted coils and the insertion angle of the coils is varied to achieve stochastically representative coil configurations.

Figure 23 illustrates an example of a single coil inserted into the "Target for Coil Embolisation" within the AVM flow field.

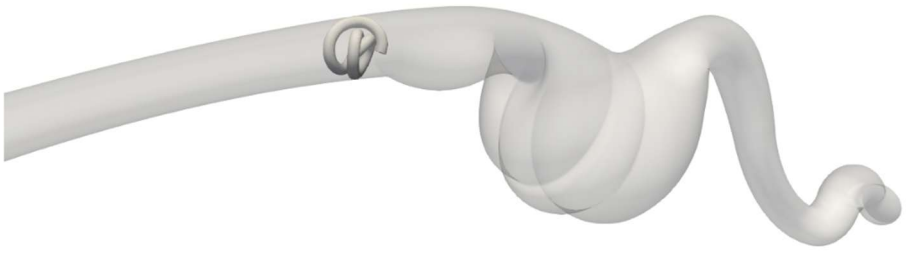

Figure 23: Example coil insertion

CFD coil implantation and workflow

The incorporation of the detailed coil geometry into the finite volume mesh follows a structured five-step process, as depicted in Figure 24.

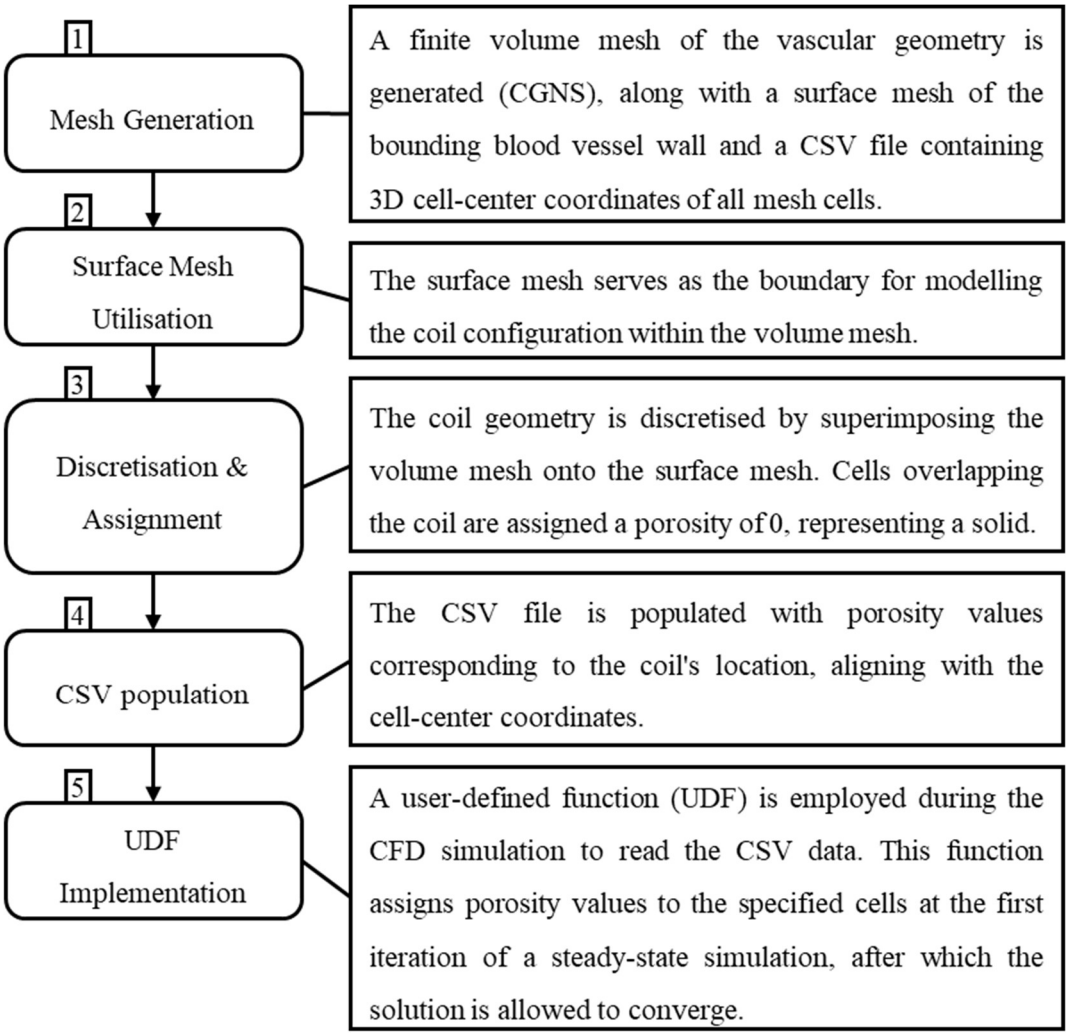

Figure 24: Coil modelling workflow

UDF implementation

Two User-Defined Functions (UDFs) were utilised to model and assign the porosity and inertial resistance respectively within the mesh cells occupied by the embolisation coil geometries from the DER simulations. This approach allowed for a more sophisticated representation of the coil's impact on the blood flow within the computational domain. The two codes are henceforth referred to as the "Coil Porosity Allocation" and "Coil Resistance Assignment" UDFs. Both of the codes are of the macro DEFINE_PROFILE type, which is capable of accessing and scoping values to any mesh feature including cell zones, cells, faces and individual nodes.

The output of the coil deployment (DER) simulations are CSV files listing all mesh cell centers occupied by the coil, identified by associating these coordinates with a porosity value of 0 (solid). The Coil Porosity Allocation UDF assigns these porosity values to the corresponding mesh cells, effectively mapping the coil geometry into the computational mesh. This process, detailed in Table 4, ensures accurate representation of the coil's geometry, given the mesh resolution is sufficient.

Table 4: Overview of Coil Porosity Allocation Function

Step	Description
Coil mapping	Opens the text file containing the 3D coordinates and corresponding porosity values. These values are stored in an array for further processing.
Cell matching	Iterates over all mesh cells and compares the cell centroids with the stored coil coordinates to locate the matching cells based on the cell-centroid.
Porosity Allocation	If a match is found within a specified tolerance, the porosity value is assigned to the cell, and this value is stored using a User Defined Memory Index (UDMI).

The second define profile macro assigns an inertial resistance value to cells based on the porosity profile generated by the Coil Porosity Allocation function.

Table 5: Overview of Coil Resistance Assignment Function

Step	Description
Coiled cell Resistance Assignment	Checks the UDMI value for each cell. If the UDMI value is 0.00 (indicating a coil is present), a high inertial resistance value, derived in section 2.3.1, is assigned.
"Empty" cell resistance assignment	If the UDMI is 1.00 (indicating no coil), the resistance is set to 0.00, allowing free flow.

The "Empty" cell resistance assignment as described in Table 5 is pertinent as inertial resistance is a diffusive property and therefore may spread to other cells surrounding the coil, hence the Coil Resistance Assignment Function writes the coiled and empty resistances to cells at each iteration of the solution.

The inertial resistance applied in the non-uniform porous media model was taken directly from the experimentally validated uniform model to ensure consistency in representing the flow-impeding behaviour of the coil. This value was applied to mesh cells intersected by the DER-generated coil geometry, resulting in spatially varying resistance that reflected local coil occupancy. This approach preserved the model's ability to differentiate between densely and sparsely packed regions, where cumulative resistance and flow impedance differ meaningfully. This value was selected as opposed to applying a uniformly high resistance value, which would have imposed identical flow restriction in all coil-occupied regions regardless of local geometry, thereby disregarding variation in packing density and leading to a binary representation of flow suppression. The selected resistance allowed or flow deceleration in a manner more consistent with physical measurements, without introducing solver instabilities (negative pressure values/spikes) or compromising sensitivity to coil configuration.

To incorporate a large number of coils, the "Target for Coil Embolisation" shown in Figure 14 was extended to make up most of the arterial feeder branch, as shown in Figure 16. Figure 25 shows a single coil inserted into the enlarged zone as well as the discretisation and recreation of the coil in the CFD solver. Notably, the walls of the discretised coil are not smooth because it takes the shape of the native mesh.

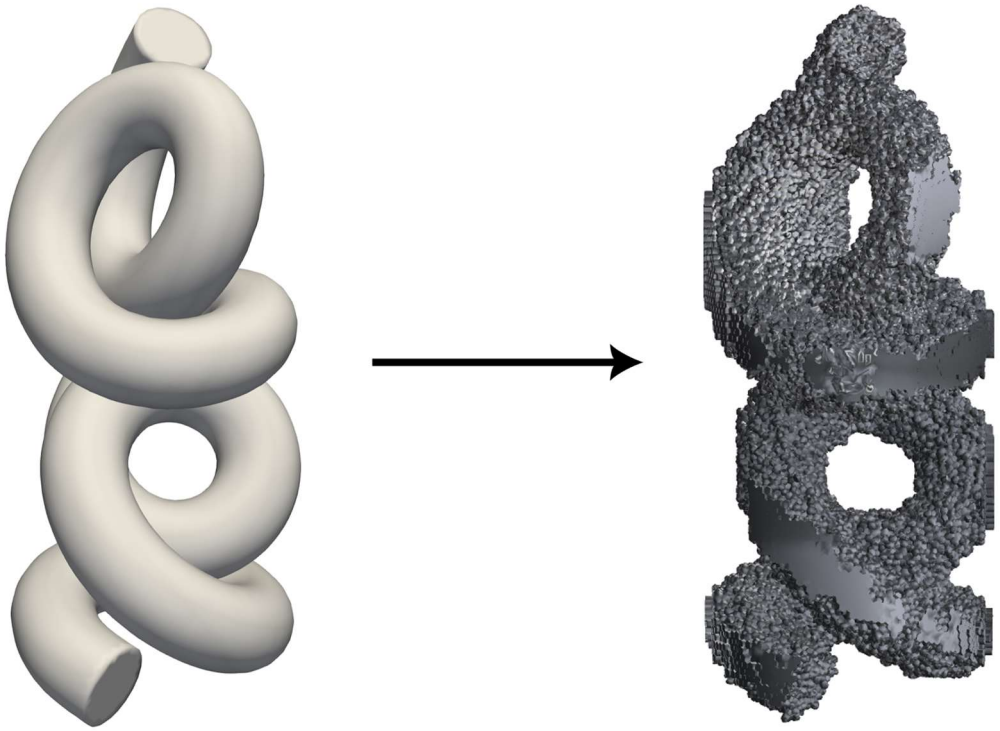

Figure 25: Comparison between coil geometry and discretised coil

The cell-based approach for simulating embolisation coils was selected for this work as opposed to a geometric subtraction of the coil from the flow field due to its higher flexibility, lower computational cost, and capacity for detailed haemodynamic analysis. This has been reported in literature such as Kyung *et al* (2007), wherein it is acknowledged that the subtraction method results in constraints on stability and causes computations to become "prohibitively expensive".

In the context of embolisation, the flow blockage effects are critical, and the fidelity of the simulation focuses on localised flow disturbances rather than just geometric accuracy. The subtraction approach, although widely used for rigid and simple geometric bodies, has inherent difficulties with the handling of the tortuous nature of coils that conform to irregular vasculature. As such, the subtraction approach often requires geometric simplification to allow for meshing, which compromises the accuracy of simulations, particularly at coil boundaries.

This is problematic in cases like AVMs where fine geometric details can affect local flow dynamics. The cell-based approach eliminates this limitation by embedding the coil into the computational domain, allowing for intricate flow patterns to emerge naturally around the coil. Coils introduce highly localised flow disturbances, including vorticity, recirculation, and high shear regions. The cell-based approach preserves the resolution of these features without the need for excessive mesh refinement, which would otherwise be necessary for the subtraction method.

Lastly, subtraction methods are limited in accurately resolving thin boundary layers around coil surfaces, especially when the mesh near the interface is distorted. The cell-based approach inherently resolves boundary layers by assigning flow properties within the cells, ensuring smooth transitions without excessive computational cost.

The porous media model was thus selected for application in this work; however, it is clear it has certain limitations. Specifically, it does not allow for absolute resistance to flow, which means that a small amount of fluid is permitted to pass through the computational cells representing the coils. Thus, even when considering that the average velocity within the coil structure across all cases was found to be between $0.1 - 0.9\%$ of the surrounding flow, this has been recognised as a limitation inherent to the formulation of the porous media model. Nevertheless, the use of inertial resistance parameters derived from the coil geometry ensures that the primary physical effects are adequately captured.

2.4 Clot Modelling

2.4.1 Model background and biological mechanisms

Clotting is a complex function of both biochemical reactions and haemodynamics. The principal biochemical and flow-driven mechanisms as well as the modelling thereof are summarised herein.

An injured blood vessel triggers a vascular spasm, which causes vasoconstriction so as to reduce blood flow. Blood platelets adhere to exposed collagen fibres at the site of injury, whereafter a series of biochemical reactants (clotting factors), most importantly, glycoprotein IIb–IIIa receptor (integrin $\alpha_{\mathrm{IIb}}\beta_3$) and prothrombin are exposed (Savage & Saldivar, 1996). A cascade of enzymatic reactions (coagulation) follows wherein, fibrin (insoluble protein) is generated from the enzymatic action of thrombin on the soluble plasma protein fibrinogen which ultimately solidifies into a fibrous mesh surrounded by red blood cells and activated platelets thus forming the stable clot structure. This process is showcased in Figure 26 (Vedantu, 2024).

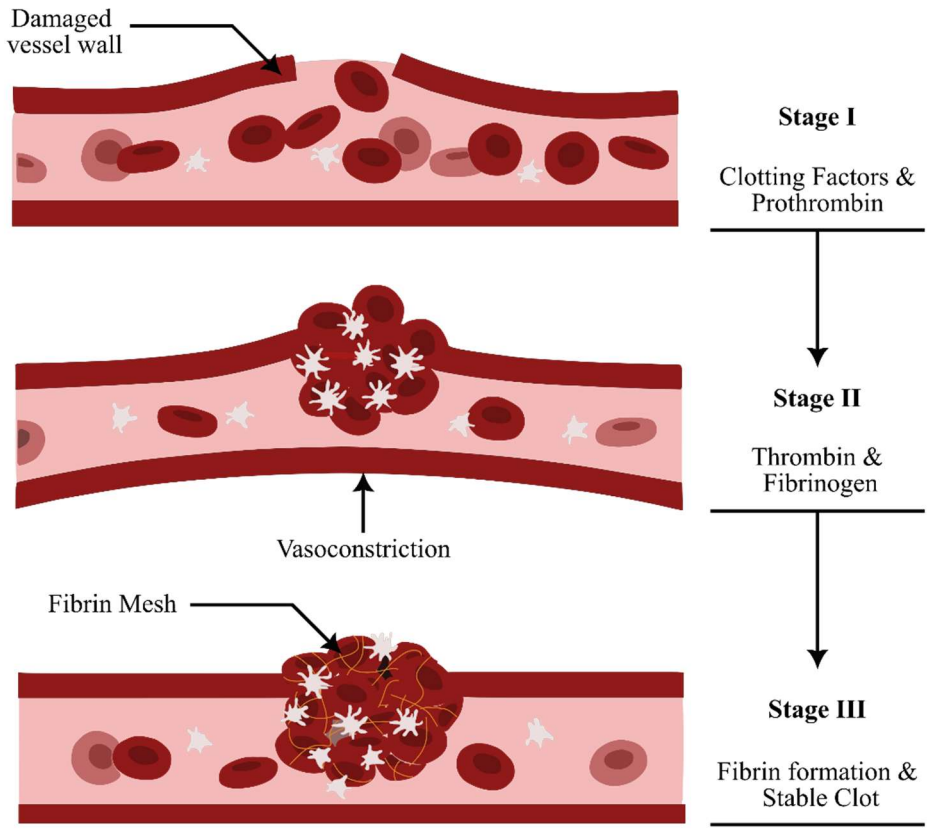

Figure 26: Fibrin clot formation process

2.4.2 Shear-based clotting model

A shear-based clotting model was developed to assess end-state clotting, i.e., the overall mechanical effects of thrombi such as those shown in stage III of Figure 26, while disregarding the biochemical reactants. Hence, this model does not capture the time-dependent nature of clot growth, however it is intended to be applied in a transient formulation to capture the changes in the flow field caused by clot formation resulting from the convective terms in the governing equation of the utilised solver.

The shear-based clotting model operates within a framework of model time rather than physical time, highlighting a fundamental distinction in its application. Unlike biochemical clotting models, which incorporate time-dependent reactions and species transport but are computationally expensive, the shear-based model used here is governed solely by convective flow variables such as velocity and lack an inherent time scale. As such, the progression or growth of clot formations in this work refers exclusively to computational time and no assertions are made regarding the validity of the intermediate clot formations as only the end-state of the clot is analysed, which facilitates transient tracking of the shear field changes but does not correlate to the actual physical time required for clotting *in vivo*.

The use of a transient model is crucial for capturing the convective adjustments in the shear field due to changes in clot morphology. These adjustments are necessary to resolve how local shear conditions influence development, leading to a steady-state or converged clot morphology where no further clotting can occur. While the time-stepping approach resembles pseudo-time methods often employed in CFD to simulate flow field evolution or changes in boundary shape, it does not reflect realistic clotting timescales. Instead, the model's transient framework enables the resolution of flow interactions as they adapt to clot structures, similar to momentum-based models used for position adjustments in FSI.

The shear-based clot model, like the coil model, is formulated as a customised porous media model that operates on a computational cell basis and is executed through the use of a UDF. This model was built to replicate the fundamental mechanics of clot growth and formation through the implementation of shear rate and adjacency conditions so as to model the total clot size and distribution due to coil embolisation.

Shear rate limitations

Shear rate limits are the principal metric which guide the computational clot formation as well as controlling the assignment of clot properties. These limits and their associated properties are tabulated below for further discussion.

Table 6: Shear rate conditions and clot properties

Property	Value	Reference
Shear rate clotting limit $[s^{-1}]$	50	(Casa *et al*, 2017)
Clot Porosity $[-]$	0.75	(Diamond, 1999)
Clot Permeability $[cm^2]$	$1.0e+12$	(Brass & Diamond, 2016)
Fibrinolysis Condition $[s^{-1}]$	5300	(Brass & Diamond, 2016)

It is important to note here that "Fibrinolysis" refers to the process by which fibrin clots, are broken down into smaller pieces. Biologically, this process is promoted by higher shear rates, which exert greater mechanical forces on the thrombus architectural cells, causing them to rupture or break apart (Brass & Diamond, 2016). This stress can disrupt the outer clot, leading to its disintegration and contributing to clot dissolution.

The properties introduced in Table 6 are detailed below:

- Shear rate clotting limit: As defined by Casa *et al* (2017) coagulation dominates low-shear environments as opposed to platelet deposition. This coagulation, i.e., the reaction between thrombin and fibrinogen to form the fibrin clot occurs at shear rates below $50\ s^{-1}$.
- Clot Porosity, Permeability and Lysis condition: A series of papers (two of which are listed in Table 6) produced by Diamond *et al* have investigated the mechanical and fluid properties of clot formations, including the effective porosity associated with clot masses (0.75), the permeability, or in other words the inverse viscous resistance, associated with pure-fibrin clots ($1.0e+12$) and the minimum shear rate at which lysis occurs for these pure-fibrin clot formations ($5300\ s^{-1}$).

A second User-Defined Memory Macro (UDM) is applied to store cell porosity values, as in the case for the coil modelling detailed in section 2.3. The UDM is subsequently used for clot visualisation, adaptive mesh refinement and experimental comparison.

Wall-bounded thrombogenesis

As shown in Figure 26, clot formations have their origins at sites of injury, i.e., the aneurysmal zone, along blood vessel walls. To capture this computationally, an initial group of wall cells is selected to serve as the origin site for thrombus formation. This enforcement may be better understood with the knowledge of the mesh hierarchy in ANSYS Fluent. Figure 27 provides an illustration of how the mesh is organised into threads and how this may be used for mesh variable manipulation.

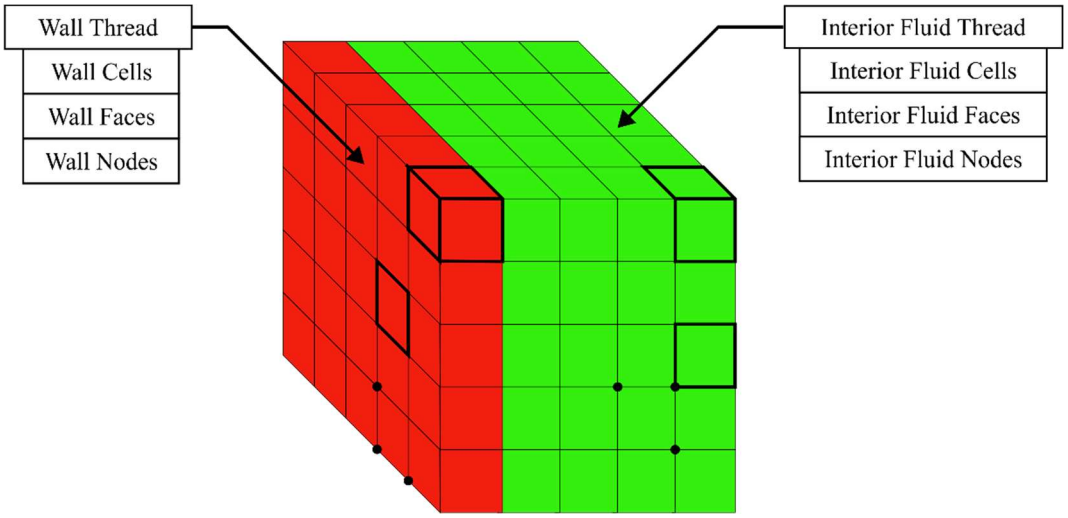

Figure 27: Mesh organisation and hierarchy

The mesh hierarchy is defined in order of thread, cell, face and finally node. All mesh archetypes are grouped into thread pointers, further subdivided by region and function. Hence, cells associated with walls, boundary conditions, etc. may be accessed individually for localised control. Figure 28 shows an example of wall selection as applied to the AVM.

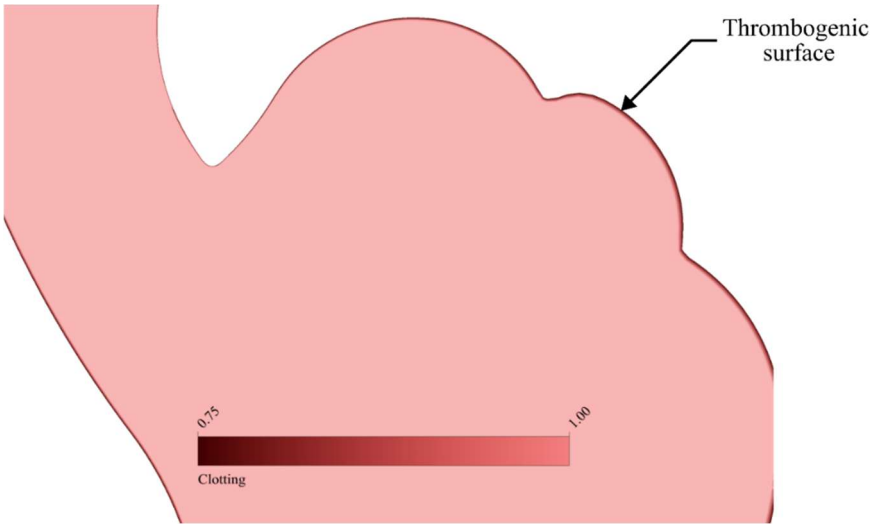

Figure 28: Thrombus origin site allocation within AVM model

Figure 28, combined with the flow shown in Figure 19, illustrates that clot formation is limited to regions of low velocity and exhibiting recirculation. These characteristics promote thrombosis, as lower shear rates and extended residence times (duration fluid remains in a specific area) facilitate clot genesis. Clot formation in the model is not forced at specific nodes but occurs naturally where local flow conditions permit, however, clot initiation is constrained to the aneurysmal wall, as this aligns with the understanding that vessel injury due to abnormal expansion fosters a pro-thrombotic environment.

Adjacency-controlled clot growth

Progressive clot development from a wall-bounded source is accomplished through the use of connectivity macros and associated indices. Effectively, the clotting model only allows clot formations to proliferate from cells which have already been assigned clot properties, i.e., the entire clot formation will develop from the initial site of thrombogenesis. Adjacency is maintained through UDF thread control and face adjacency indexing, primarily through the use of two commands F_{C0} and F_{C1}, details of which are shown in Figure 29.

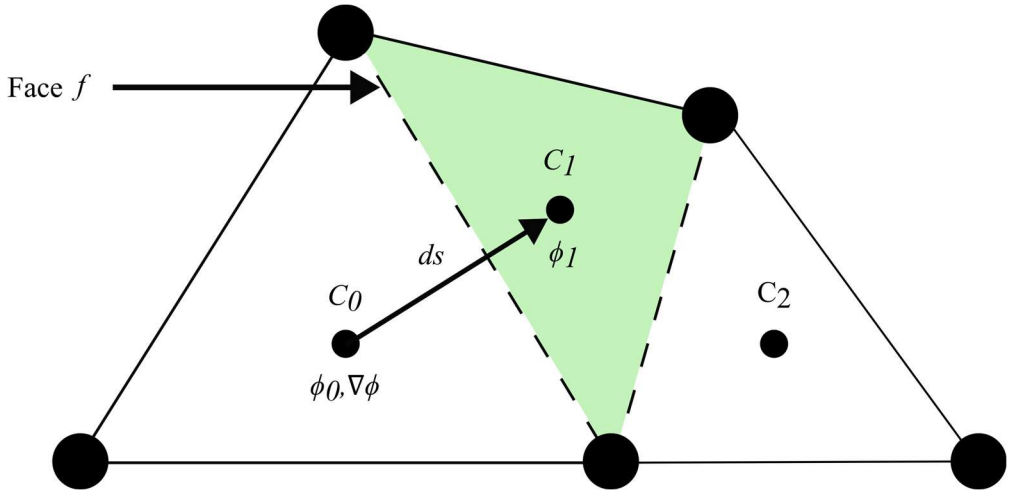

Figure 29: Adjacency controls and indexing

The functions F_{C0} and F_{C1} enable the clotting UDF to retrieve data from the cells located on either side of a specific face, f, allowing for conditional controls based on clot adjacency. Using Figure 29 as an example, if the cell C_0 is identified as clotted, and cell C_1 meets the shear rate criteria for clot formation, then and only then may C_1 be marked as a clotted cell. However, a third cell C_2, located adjacent to C_1 but not sharing a boundary face with C_0, cannot be classified as clotted in the current time step, even if it meets the shear rate criteria, because it lacks adjacency to an existing clot. This ensures that clotting spreads logically based on the flow conditions and proximity to existing clots.

Clot front refinement

Through investigation of the clot propagation and final morphology achieved using the shear-based model, it was found that utilising Adaptive Mesh Refinement (AMR) and scoping this refinement to cells at the clot growth front allowed for a much more accurate replication of the final shape and distribution of the clot. This investigation was carried out using an idealised aneurysmal geometry and the results of the comparison with experimental clot growth (Ngoepe *et al*, 2021) may be found in section 3.1.2.

The refinement is scoped to the clot front through cell registers modified to target cells with a large gradient of porosity, while cells with a low porosity gradient are scoped for coarsening. Cells at the clot front exhibit the highest porosity gradients, as shown in 3D in Figure 30, as the clot boundary forms an interface between the unobstructed flow and newly-formed clot structures, resulting in a sharp change in local porosity. Through AMR, the model can more accurately capture the clot structure, while the coarsening of stable, pre-existing clot regions reduces computational demands.

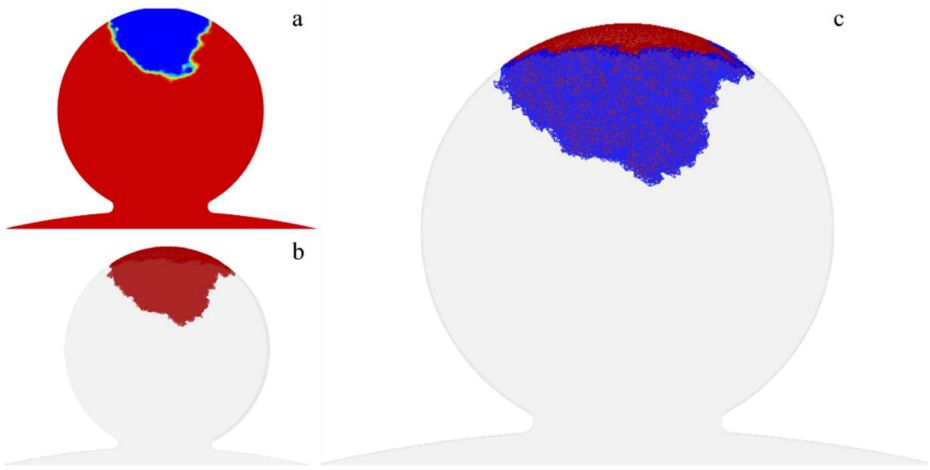

Figure 30: Isolation of the clot front for adaptive refinement (a) UDM contour (blue clot), (b) clot structure by cell and (c) adaption applied to clot front (blue adaption cells)

2.5 Simulation Setup and Conditions

This section details the CFD workflow from meshing of the AVM geometry to the computational setup and includes key physical and numerical considerations. At this point, it should be noted that the computation of the coiled flow and clotting flow is accomplished in two steps as listed below.

Computational steps:

1. Steady state simulation (without clotting UDF): To achieve a stable flow field after the coil has been read into the mesh, treating the coil insertion as instantaneous.
2. Transient simulation (with clotting UDF): This simulation determines the end-stage clot morphology with both coiling and clotting functions active. It reflects computational time rather than physical clotting time, resolving shear-dependent processes until the clot reaches a steady state.

2.5.1 Meshing

As discussed in section 2.4.2, mesh adaption is applied over the course of the simulation which incorporates clotting, however this adaption is limited to the AVM aneurysmal zone and a minimum orthogonal quality of 0.1 is enforced for this adaption. Henceforth, the mesh discussed will be that used for the steady state initialisation of the coiled flow.

The AVM mesh as well as key parameters which describe mesh size and quality are given in Figure 31.

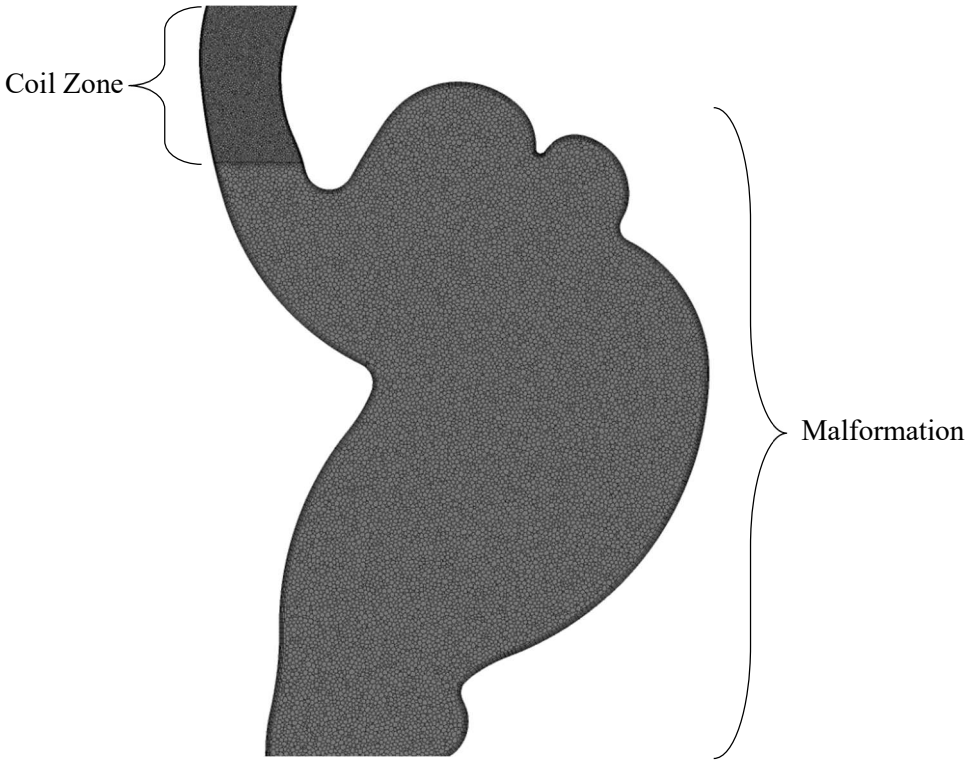

Mesh Metric	Type	Total Elements	Orthogonal Quality	Aspect Ratio
Specification	Polyhedral	2,734,543	Min: 0.2484	Min: 1.3045
			Avg: 0.9404	Avg: 2.4360
			Max: 0.9999	Max: 21.6701

Figure 31: AVM mesh and mesh qualities

The polyhedral mesh type was selected due to its advantages in the context of biomedical fluidics, including that the increased number of neighbouring elements enhances the accuracy of gradient calculations, especially in regard to shear stresses (Spiegel *et al*, 2011) and that polyhedral meshes generally outperform tetrahedral meshes in terms of convergence and simulation stability

A note on local meshing controls

In addition to the global meshing strategy, a number of domain-specific local meshing controls were implemented to ensure sufficient resolution of key haemodynamic features. For the coil region, mesh sizing was based on the smallest structural feature, the $0.889\ \mathrm{mm}$ wire diameter, with a base mesh size if $0.08\ \mathrm{mm}$, providing approximately 11 cells across the diameter. This sizing enables adequate representation of local flow, with an average cross-sectional area deviation of $\sim 5\%$ between the meshed and ideal coil geometry.

The adaptive local meshing scheme applied to the aneurysmal (clot-prone) region, was informed by that found to be ideal for reliable end-state clot analysis. Beginning from the mesh base size of $0.15\ \mathrm{mm}$, the mesh was refined in two steps to $0.0375\ \mathrm{mm}$, with an additional layer reducing local resolution to $0.01875\ \mathrm{mm}$ in persistently clot active zones. Refinement was applied at each timestep based on shear rate thresholds, to ensure progressive resolution of low-shear regions, particularly adjacent to vessel walls. While initial identification of clot-prone regions within the aneurysmal zone was determined via shear rates computed from the base mesh, refinement was applied prior to subsequent timesteps, so as to reduce the potential of the wall-adjacent low-shear zones being persistently under-resolved.

2.5.2 Setup and flow considerations

Boundary conditions

While pulsatile flow has been neglected in this work, the plug flow values for the arterial inlet flow boundary conditions (BCs) were derived from the pulsatile velocity and pressure profiles for the inlet artery, as shown in Figure 32 (Gallo *et al*, 2020).

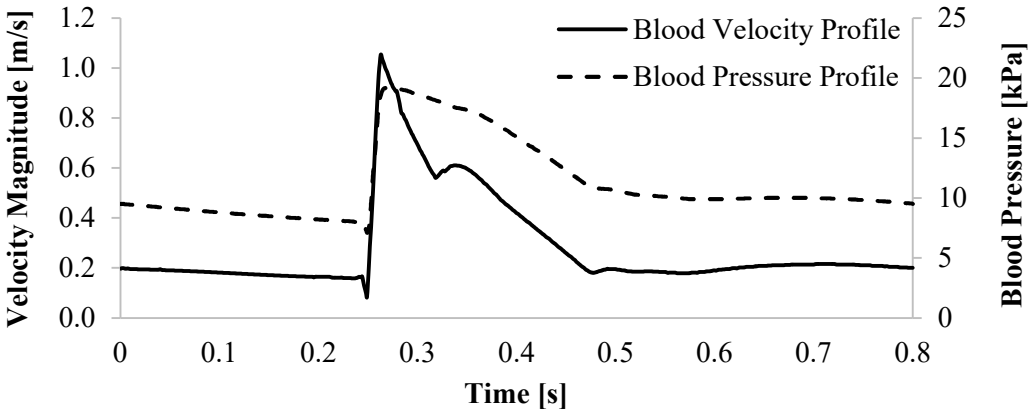

Figure 32: Pulsatile velocity and pressure profile for the posterior tibial artery

From Figure 32, the mean pulsatile velocity and pressure were taken as the arterial inlet conditions, while AVM-related arterial pressure drops derived from Zhang *et al* (2020), allowed for the application of a function which scopes the arterial outlet pressure to be a function of the arterial inlet pressure ($\approx 66\%$). The venous boundary conditions are typically constant in terms of both pressure and velocity and thus the venous inlet velocity was derived from Kalayci *et al* (2015) based on reference values for the flow rate and diameter of the anterior tibial vein, while the venous inlet pressure was assumed to be within the standard range at 8 mmHg (1066.576 Pa) (Shah & Louis, 2023). A summary of the BCs applied for the AVM embolisation model may be found in Table 7, in which the gauge pressure are absolute.

Table 7: Boundary condition specification

Boundary	Applied BC	Specification
Arterial Inlet	Velocity Inlet	Velocity - 0.2829 m/s
		Initial Gauge Pressure – 11244 Pa
Arterial Outlet	Pressure Outlet	Gauge Pressure – f(Arterial Inlet Pressure)
Venous Inlet	Velocity Inlet	Velocity - 0.0111 m/s
		Initial Gauge Pressure - 1066.576 Pa
Venous Outlet	Pressure Outlet	Gauge Pressure – 0 Pa

Turbulence consideration

Vascular flows may be likened to more generic pipe flows albeit with more curvature and more complex flow fields. The well-known critical Reynolds number (Re) for pipe flows as given by Potter *et al* (2010) is 2300, however some literature has documented that physiological flows and particularly blood flows exhibit turbulent-like or fully turbulent behaviour at significantly lower Reynolds numbers. These reported critical Re, derived from experimental studies include Jain (2016) which derived the Re from a stenosed pulsatile flow and Saqr *et al* (2020) which derived the Re from a multiharmonic pulsatile flow. These papers reported critical Reynolds numbers of 600 and 400 respectively.

Given that the location of the parent vessel artery in question, i.e., the posterior tibial artery, is in the lower leg (an extremity) it is unlikely that the flow will require turbulence-capturing. Simulations of the physiological flow (unembolised and neglecting clotting) through the AVM have shown that the maximum expected Reynolds number in the domain is approximately 40 which is well below the most conservative critical Reynolds numbers reported and given that the addition of the embolisation and clotting models will only serve to further slow the flow, a laminar formulation has been applied to all computations.

Solution methods customisation – PISO and PRESTO!

When simulating flows with large negative pressure gradients, such as in porous media models, selection of numerical schemes becomes critical to maintaining both accuracy and stability. The Pressure-Implicit with Splitting of Operators (PISO) algorithm offers an efficient solution for pressure-velocity coupling, especially in unsteady flow simulations. Its ability to perform multiple pressure-correction loops ensures that the pressure and velocity fields remain consistent in scenarios where rapid changes in flow direction and pressure occur, such as at the interface between a porous medium and free flow regions. Thus, PISO is a robust choice for simulations where large pressure gradients are common.

Additionally, the PREssure STaggering Option (PRESTO!) complements PISO by addressing the challenges of accurately interpolating pressure on highly skewed or non-uniform grids. The staggered pressure interpolation helps to ensure that high-pressure gradients do not cause numerical instability, making PRESTO! particularly suited to cases involving porous media, where localised flow obstructions cause sudden drops in pressure. Together, PISO and PRESTO! provide a powerful combination for handling complex flows with steep pressure gradients and ensuring convergence even under challenging flow conditions and thus has been used for all transient simulation steps.

2.6 4D MRI

4D MRI, so named for its integration of 3D spatial encoding and temporal resolution, is a medical imaging technique that enables the measurement of 3D velocity fields using Magnetic Resonance Imaging (MRI). As an advanced modality, it expands upon traditional MRI, which primarily focuses on anatomical visualisation, by resolving velocity components of moving tissues or fluids. This technique offers a non-invasive means of flow visualisation while simultaneously allowing for quantitative measurements of velocity. This was performed *in vitro* to verify the velocity flow field in an unembolised model and partly due to a lack of 3D tomographic Particle Image Velocimetry (PIV) facilities, while also serving as a feasibility study into the applicability of a tabletop MRI system.

2.6.1 MRI overview and initialisation

MRI is grounded in the principles of nuclear magnetic resonance, wherein charged particles which possess intrinsic angular momentum (a quantum property) generate a magnetic field and thus have a magnetisation vector. The vectors are randomly oriented in the absence of external magnetic factors, however, when placed in a strong magnetic field they align parallel or anti-parallel to the field. The net magnetisation, due to a slight excess of vectors aligned in one direction, is manipulated during MRI imaging. These vectors primarily arise from the alignment of hydrogen protons with an external magnetic field, referred to as B0.

The net magnetisation vectors are not fixed but precess about the axis of the magnetic field at a rate known as the Larmor frequency. RF pulses, tuned to this frequency, momentarily flip the net magnetisation vector from its alignment with the external magnetic field, causing it to rotate. As the vector relaxes back to equilibrium, the changing magnetic field induces a current in the MRI receiver coils, generating the signal used for imaging.

The position and selection of imaging slices are determined through the application of magnetic field gradients. These gradients cause a spatial variation in the magnetic field, altering the resonance frequency of the protons depending on their position. This variation combined with frequency-selective RF pulses allow for spatial encoding in 3D via the application of three orthogonal gradients, known as the slice, read and phase gradient.

The initialisation of the magnetic gradient (Shim) and RF pulse strength is essential for the accurate acquisition of spatial and flow data. An example is given in Figure 33, where RF pulse strength is denoted as B1, showcasing how these parameters are allowed to achieve stability prior to measurement. The magnetic field strength, which is largely a function of temperature, and the Larmor frequency are also determined prior to each imaging session.

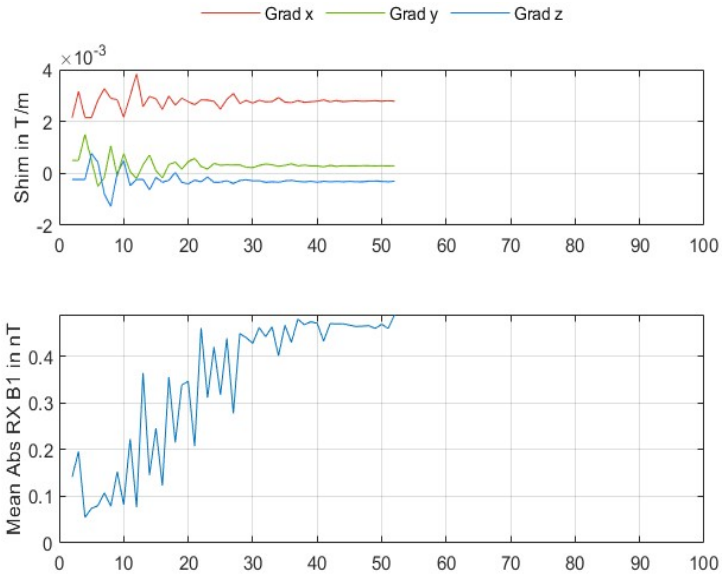

Figure 33: Initialisation of magnetic field gradients and RF pulse strength by iteration

The raw data generated by MRI takes the form of a 2D or 3D spatial frequency map known as k-space. K-space does not directly represent the image but instead stores the frequency and phase information of the MR signal. The process of "filling" k-space involves acquiring data from the MR signal, where different lines or regions of k-space correspond to different phase-encoding (phase direction) and frequency-encoding (read direction) gradients applied during the scan. Once k-space is fully sampled, an inverse Fourier transform (IFT) is applied to convert the data into the raw spatial image amplitude, as shown in Figure 34. Here the slice is selected via the magnetic field gradient in the y direction and the in-plane spatial information is encoded by the x (phase) and z (read) magnetic field gradients.

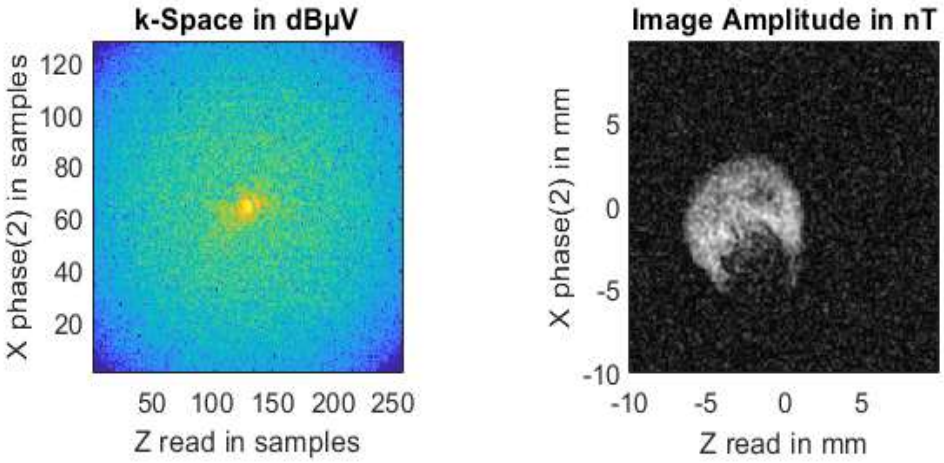

Figure 34: Example of a 2D k-space and the resultant image

2.6.2 Velocity encoding

Phase contrast MRI (PC MRI) denotes the process whereby velocity is measured during MRI scans by way of phase shifts. PC MRI relies on the concept that moving protons will accumulate a phase shift when exposed to a magnetic field gradient. This phase shift is directly proportional to the velocity of the moving spins, making phase a direct measure of velocity in PC MRI.

In a typical MRI scan, phase encoding is used to spatially encode information by applying gradients along different axes, causing protons in different locations to experience different phase shifts. In PC MRI, this process is expanded to include velocity encoding. This is achieved through the introduction of bipolar phase gradients, as shown in Figure 35, wherein the effect of this gradient on stationary spins is neutral, however moving spins accumulate a phase shift that is linearly proportional to their velocity.

By applying additional bipolar gradients, moving protons accumulate different amounts of phase shift depending on their velocity. Thus, the use of these gradients in all orthogonal directions allows for a full 3D flow quantification. Notably, protons moving in the direction of a gradient will experience a positive phase shift, while those moving in the opposite direction will experience a negative shift.

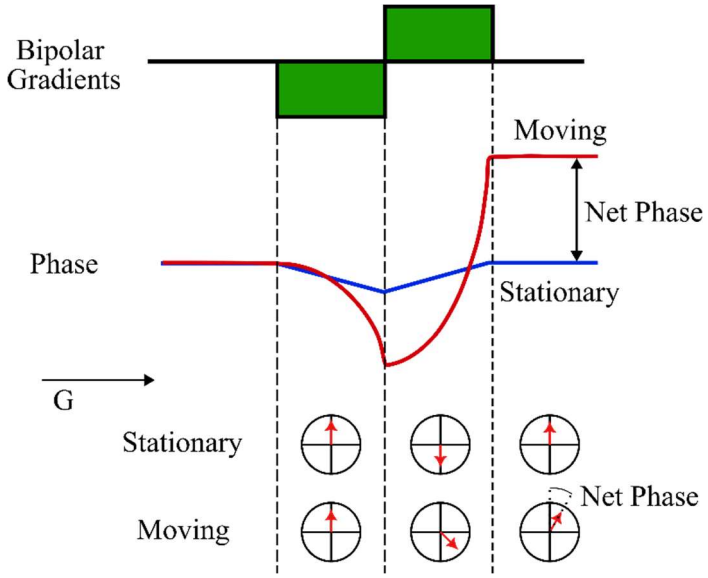

Figure 35: Bipolar gradients and their effect on stationary versus moving protons

Two sets of scans are performed, one with stationary fluid and the other with moving fluid. The phase of the MR signal is measured for each voxel, and the difference between the two images, the flow encoded and stationary encoded images, acquired with different bipolar gradients is used to calculate the velocity of blood flow in that voxel.

For a proton moving at a velocity v, the phase offset $\Delta\emptyset$ caused by the bipolar gradient can be expressed as:

$$\Delta\emptyset = \Gamma \cdot v \cdot \Delta G \cdot \Delta t \quad \ldots\ldots\ldots\ldots 9$$

, where Γ is the gyromagnetic ratio (constant for a given nucleus), ΔG is the strength of the bipolar gradient and Δt is the time duration of the gradient. This calculation is performed independently for each direction, resulting in a 3D velocity vector field for the entire imaging volume.

A consideration for bipolar gradient application is the velocity encoding parameter (VENC), which must be defined prior to acquisition. The VENC serves as a threshold for calculating velocity, as it represents the maximum velocity that can be accurately measured in a given direction. If velocities exceed the VENC limit, a phenomenon known as phase aliasing occurs. This occurs because the phase shift induced by moving spins surpasses the $360°$ range, leading to phase wrapping, where higher velocities appear incorrectly as lower velocities due to the cyclical nature of the phase signal.

Phase wrapping results in discontinuities in velocity, which may be resolved through phase unwrapping techniques. These methods detect and correct erroneous jumps in the phase signal, restoring accurate velocity measurements. As demonstrated in Figure 36, phase aliasing can introduce noise in velocity measurements if not handled correctly.

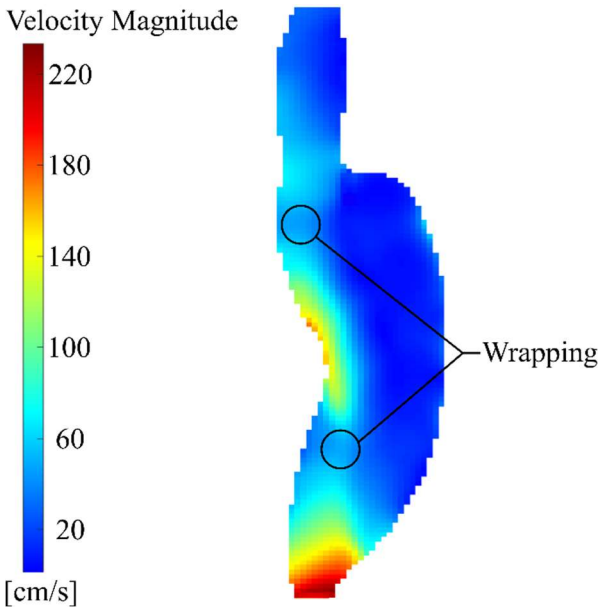

Figure 36: Phase wrapping in velocity measurements

2.6.3 Flow apparatus and experimental considerations

The MRI scanner utilised for experimental verification is the Pure Devices research MRI system with a 0.5 T field gradient strength and a bore of 15 mm (Appendix C). This tabletop MRI scanner (Pure Devices, Germany) as shown in Figure 37, is not suitable for clinical use but is useful for imaging research. The size of the bore is a limiting factor which necessitated a 2/3 scaling of the experimental geometry, as mentioned in section 2.1. Hence, the flow rate of 2 ml/s was scaled to 1.3 ml/s to ensure dynamic similarity.

4D MRI techniques require substantial time to acquire images, thus a closed flow circuit was constructed to maintain a constant flow of BMF through the tabletop scanner.

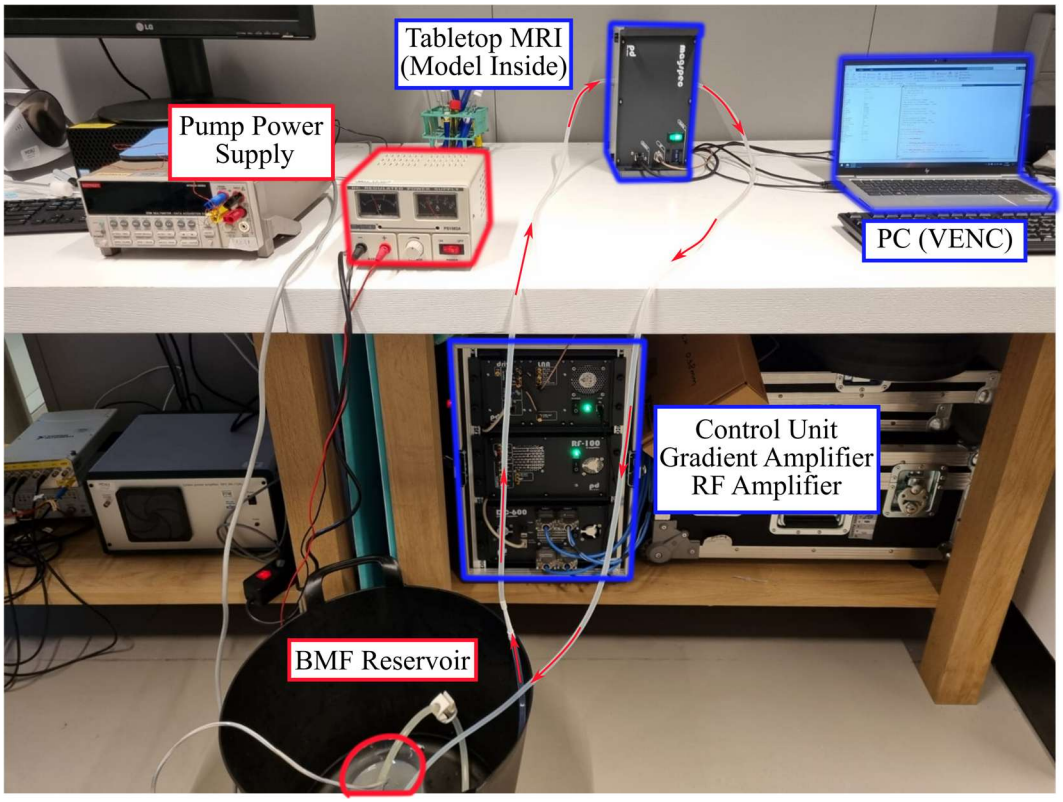

Figure 37: MRI flow apparatus

From Figure 37, the imaging system (blue) comprises the MRI scanner, which is rotated to eliminate any static pressure drop or unwanted acceleration within the flow region in the scanners field of view. This system also includes the scanner's control unit and the gradient and RF amplifiers, which are employed to optimise the strength and precision of image acquisition and encoding. The flow system (red) is composed of a calibrated pump that delivers a steady flow of BMF from a reservoir into the experimental AVM geometry, located within the magnetic bore of the scanner, ensuring consistent and reliable flow during imaging and velocity encoding.

Subsequent to the initial setup and construction of the MRI rig, the flow system was filled with the BMF so that the velocity encoding parameters could be determined and set. These parameters are presented in Table 8 and are implemented through the MRI units' MATLAB interface (MathWorks, United States).

Table 8: MRI velocity encoding parameters

Parameter Description	Specification
Magnetic Field Strength (B0)	0.5033 T
Larmor Frequency (f_{larmor})	21.428 MHz
Longitudinal Relaxation Time (T1)	0.1 s
Transverse Relaxation Time (T2)	0.07 s
Echo Time (t_{echo})	0.008 s
K-space sampling	$32 \times 16 \times 16$
Gyromagnetic ratio (Γ)	$2.6752e + 08$
VENC	0.2 m/s
Total Sequence Time	1668.2 s (27 min)

Some of these parameters were previously mentioned in sections 2.6.1 and 2.6.2. However, more detailed explanations are provided for improved contextualisation below:

1. **Magnetic Field Strength (B0)**: The strength of the static magnetic field used in the MRI system, affecting signal quality and imaging resolution.
2. **Larmor Frequency (f_{larmor})**: Proton resonance frequency in a magnetic field.
3. **Longitudinal Relaxation Time (T1)**: The time taken for the net magnetisation to return to equilibrium along the direction of the magnetic field after perturbation.
4. **Transverse Relaxation Time (T2)**: The time for the net magnetisation vector to lose phase coherence in the transverse plane, influencing image contrast.
5. **Echo Time (t_{echo})**: The time between the application of a pulse and the collection of the signal, influencing image contrast.
6. **K-space sampling**: K-space matrix dimensions used for image reconstruction.
7. **Gyromagnetic Ratio (Γ)**: A physical constant that relates the magnetic moment of a proton to its angular momentum, impacting resonance frequency.
8. **VENC**: The velocity encoding value, used for velocity-encoded MRI.
9. **Total Sequency Time**: The total duration for the entire MRI sequence to complete.

3 RESULTS AND DISCUSSION

3.1 Validation

This section encompasses comprehensive validations of the embolisation coil and clot formation models alongside 4D MRI experimentation aimed at the verification of computational results to follow.

3.1.1 Coil Model Validation

The computational validation of the derived resistance coefficients, as discussed in section 2.3.1, was conducted by way of a parametric mesh refinement study. Twelve meshes of increasing resolution were investigated, with the key flow variable for comparison between the experimental (actual) and computational (theoretical) regimes being the outlet mass flow rate [kg/s]. In Figure 38, the error trend between experimentally and computationally derived values is illustrated. The error diminishes exponentially, reaching a constant percentage error of approximately 0.25%. The mesh metrics for the final utilised mesh are detailed in Table 9, which corresponds to the cross-section shown in Figure 38.

Table 9: Final mesh metrics for uniform porosity coil model validation

Mesh Details	Value
Number of mesh elements	1,181,188
Average aspect ratio	3.4381
Average element quality	0.8337

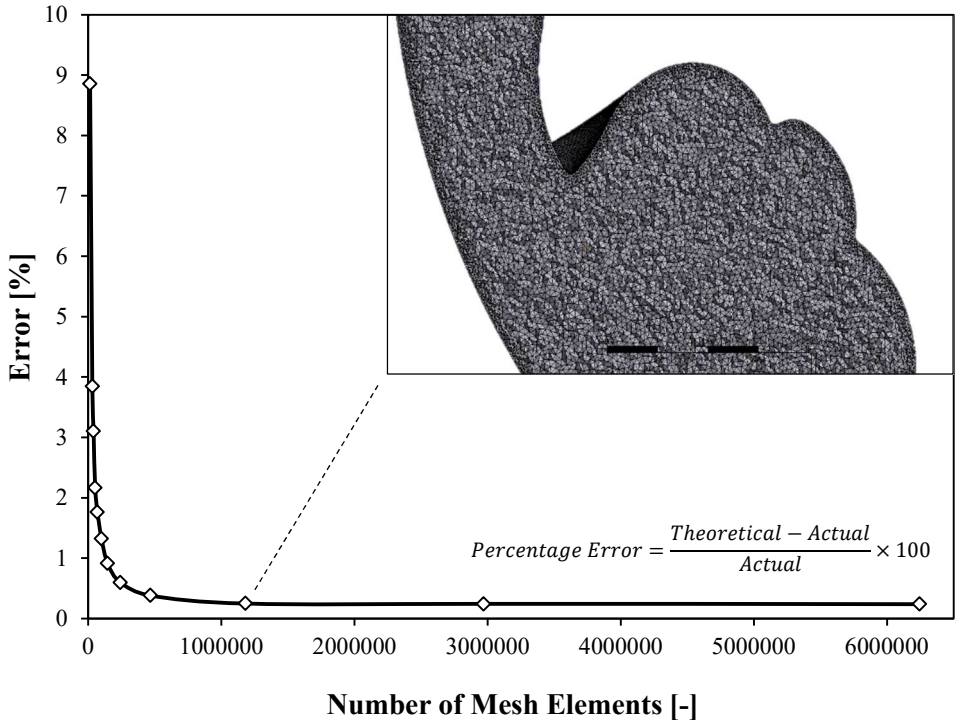

Figure 38: Outcome of parametric validation for embolisation coil simulation

Figure 38 illustrates that further mesh refinement beyond approximately 1.2 million elements does not have a significant impact on error reduction but increases computational cost by ≈ 15 % for each addition of 1 million cells. Hence, this mesh configuration was selected as the optimal compromise for further analysis.

The results of the implementation of the uniform porosity model in the AVM structure are presented in Figure 39. The set coil volume is delineated in both contours, and this may be interpreted as the region where both pressure and velocity experience a marked and abrupt reduction, indicative of a significant decrease in the total energy of the working fluid.

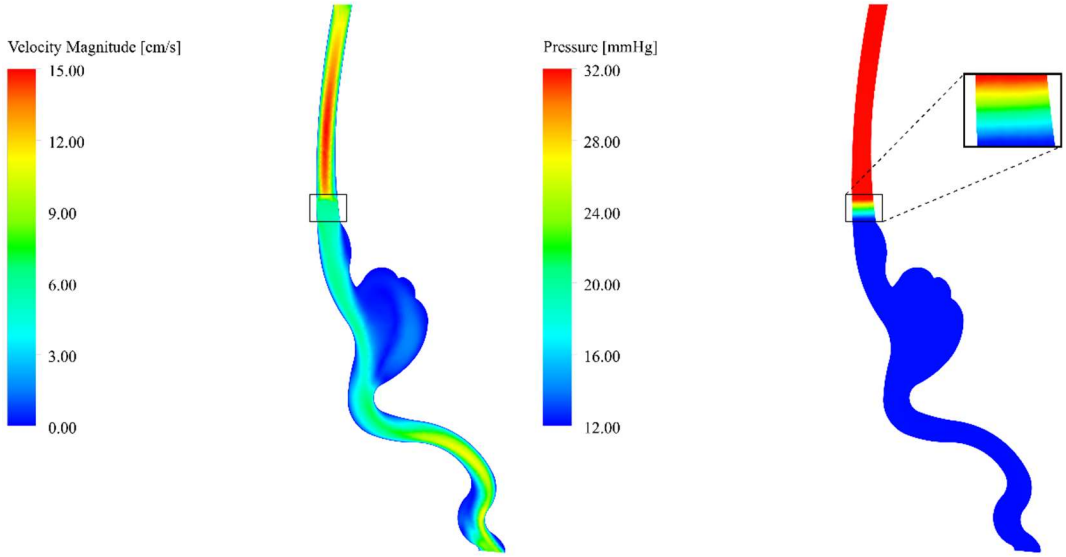

Figure 39: Velocity magnitude contour (left) and pressure contour (right) for an embolised AVM structure

Additionally, Figure 39 highlights a key limitation of the uniform porosity modelling technique. It fails to capture the complex flow dynamics observed in a packed coil configuration. Here, both velocity and pressure reductions are highly localised and regular, which does not accurately represent the impact of the tortuous geometry of a packed coil, as noted by Panneerselvam *et al* (2023). In reality, fluid permeates through gaps in the coil structure, resulting in a less uniform resistance distribution. This discrepancy underscores the need for a non-uniform porosity model, which more effectively characterises the coil's distribution, while preserving the fluid property description adopted for this work. The porosity and permeability parameters derived from this model may be directly applied to the non-uniform porosity model, therefore, the only modification in the simulation is the altered coil geometry, while the properties influencing flow resistance remain consistent.

3.1.2 Clotting Model Validation

As mentioned in section 2.4.2, the validation of the shear-based clotting model was conducted via comparison with experimental data collected by Ngoepe *et al* (Prof. Wei Hua Ho, personal communication, June 6, 2024), wherein, a pure fibrin clot was grown *in vitro* using an idealised aneurysm model. The computational geometry, replicated from the experimental setup is shown in Figure 40 and depicts that the case in question is a simplified berry or saccular aneurysm (resembling a berry on a narrow stem). The "Parent Vessel" in Figure 40 is the feeder artery for the aneurysm.

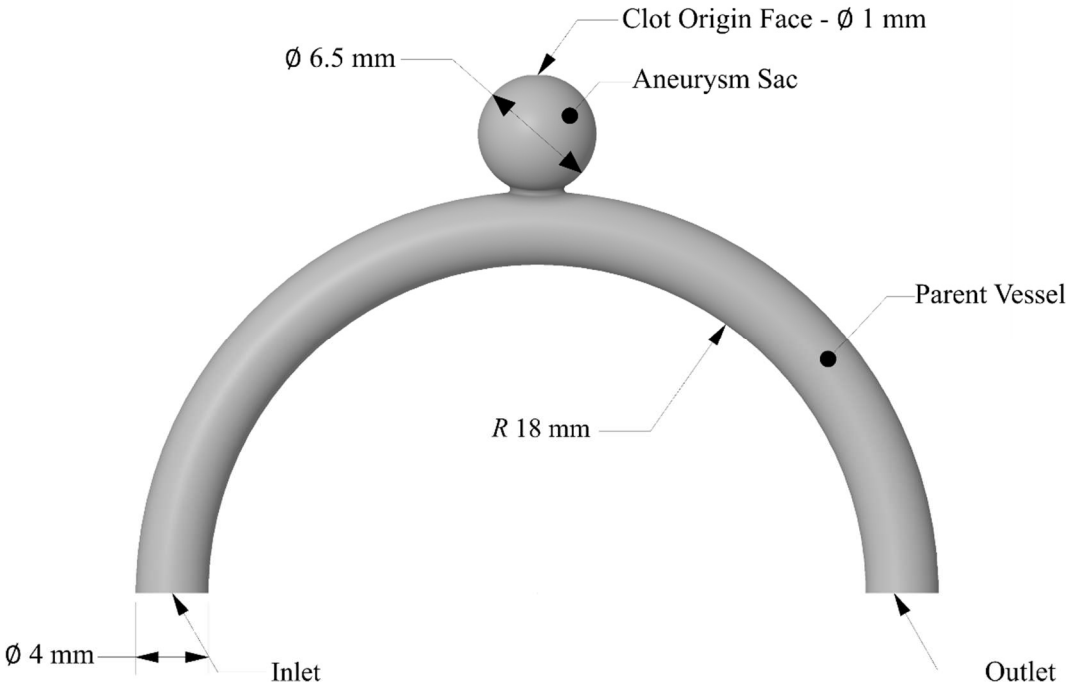

Figure 40: Saccular aneurysm flow domain for clotting validation

The "Clot Origin Face" denoted in Figure 40, serves as the site of clot nucleation in the computational domain. This is enforced in order to reproduce clot initiation in the experimental setup that incorporates biochemical reactions. Computationally, the aneurysm sac and parent vessel are separated into two distinct regions to ensure clot formation begins in the damaged vessel, however clots are not limited to the aneurysm sac and may extend into the parent vessel flow.

It is important to reiterate here, that the purpose of the shear-based clotting model is to capture the end-state of clot formation, i.e., to determine the final stable clot structure. As a result, the clotting validation was conducted by considering two primary factors, namely the total stable clot volume and the distribution of the stable clot within the aneurysm.

The stable clot volume is parameterised as the percentage occlusion (PO) [%] of the aneurysm sac, which in the case of the experimental clot was determined by way of visible area (Ngoepe *et al*, 2021), while the computational distribution is examined in 2-and-3D.

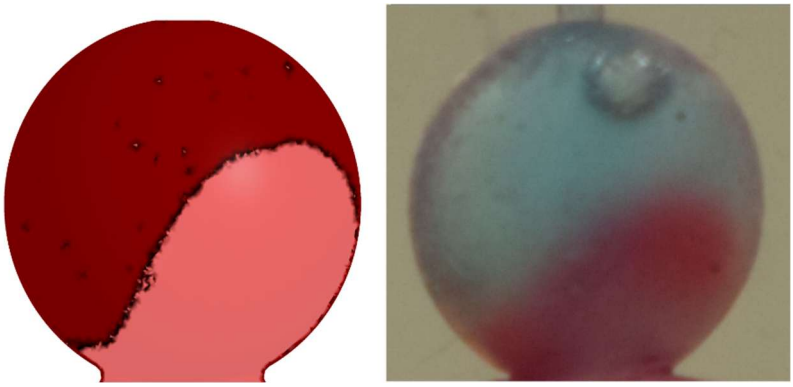

Computational PO [%]	Experimental PO [%]
57.18	57.6

Figure 41: Planar comparison of stable clot formations produced by the shear-based clotting model (left) and experimentation (right)

Shown in Figure 41, the computational clot formation is coloured dark red, while the experimental clot formation is coloured light blue, which is due to dye being introduced for clearer clot visualisation. The shear-based clotting model produces results that closely resemble the *in vitro* fibrin clot, supporting its application in this context. Notably, the shear rate threshold does not fully account for the clot front directly, as such it is less sharply defined. Although the model slightly underestimates the final clot size, the deviation is within 0.5% occlusion, which is acceptable given that this is a simplified model that does not explicitly incorporate biochemical interactions or transport.

Furthermore, the clot distribution shown in the experimental model, i.e., the larger clot formation on the left-side of the aneurysm is captured by the shear-based clotting model. This observation is significant as the flow in the parent vessel is moving from left to right in the plane of the images shown in Figure 41. Hence, it is expected that an anti-clockwise flow would arise in the aneurysm sac, with the highest shear flow entering from the parent vessel and moving up the right wall of the aneurysm, which is shown in Figure 42. As a result, clotting is concentrated in the region of lower shear rate, thus a larger formation is shown on the left side of the aneurysm sac. It is important to note that the clot progression occurs within the computational model and reflects model time, not physical time. The dynamics alluded to here represent the shear-dependent clot growth resolved during the simulation rather than real-world clotting timescales.

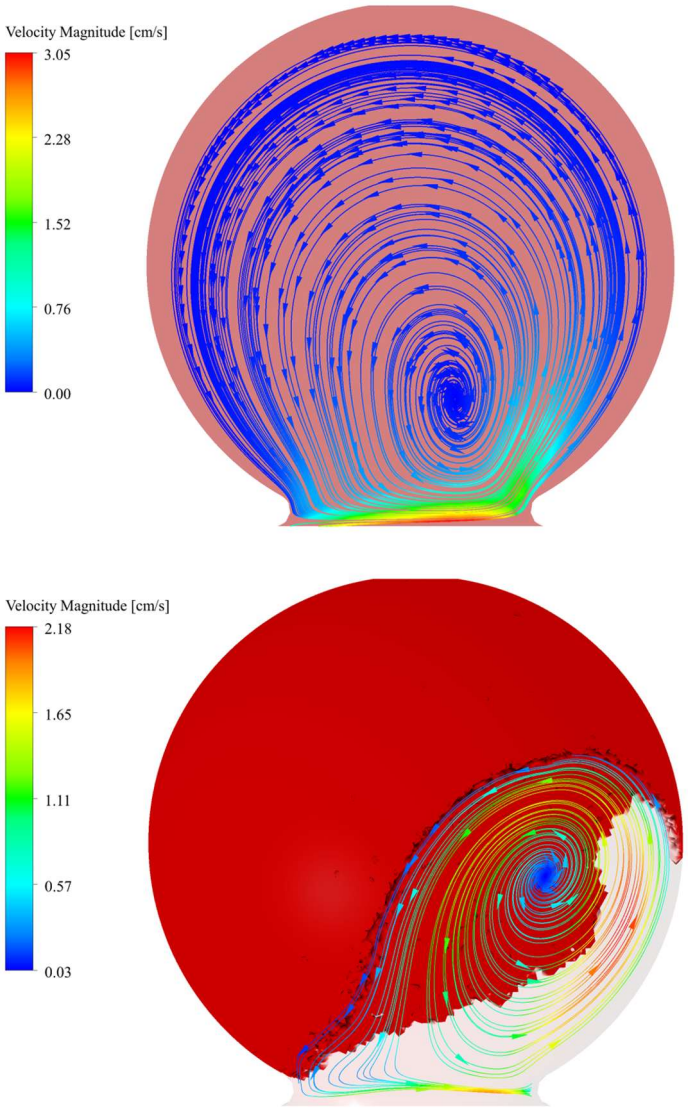

Figure 42: Initial and final vortex within the aneurysm sac

As depicted in Figure 42, the anti-clockwise vortex within the aneurysm persists after the clot has formed, with the highest velocities concentrated on the right side of the aneurysm. Notably, the vortex visibly overlaps the clot because it is a 3D structure that does not fill uniformly across the sphere of the aneurysm. This localised high-velocity zone results in elevated shear rates, inhibiting clot formation in that region. Conversely, the lower shear rates on the left side of the aneurysm create a more conducive environment for clotting. The differential shear exposure effectively guides the final clot distribution and total clot size, with the clot front being mechanically restricted from advancing into the higher-velocity zone on the right side. This flow-induced asymmetry dictates the thrombus morphology, as the interplay between clotting and flow dynamics creates a self-regulating mechanism where flow patterns influence the final spatial distribution of the clot.

3.1.3 MRI Verification

The validation of computational models is essential for ensuring their reliability, particularly in complex biomedical flow scenarios such as AVM embolisation. In this study, 4D MRI was used as a verification tool, providing an experimental dataset to assess the accuracy of the velocity fields generated by the CFD simulations. While this approach offers valuable insights, it is emphasised that the MRI testing was conducted as part of a feasibility study, highlighting the potential utility of the tabletop MR scanner for biomedical flow research rather than achieving full validation.

The field of view (FOV) of the MRI is a $20 \times 15 \times 15$ mm volume, with minor tolerances allowed for the effects of bore-wall interaction, while the presented results utilise a voxel resolution of $0.235\ \text{mm}^3$, constrained primarily by the $x - z$ plane of the magnet with the y axis being aligned with the direction of flow. This resolution was achieved using a fixed k-space encoding array of size $32 \times 16 \times 16$. Despite spatial resolution limitations, the MRI effectively captured core flow structures and velocity distributions within the AVM, enabling qualitative and quantitative assessments.

To address phase aliasing errors, as mentioned in section 2.6.2, a custom unwrapping algorithm was applied, significantly improving data quality and producing a coherent midplane velocity contour. The refined data shown in Figure 43, is a rotated and anti-aliased version of the raw data presented in Figure 36.

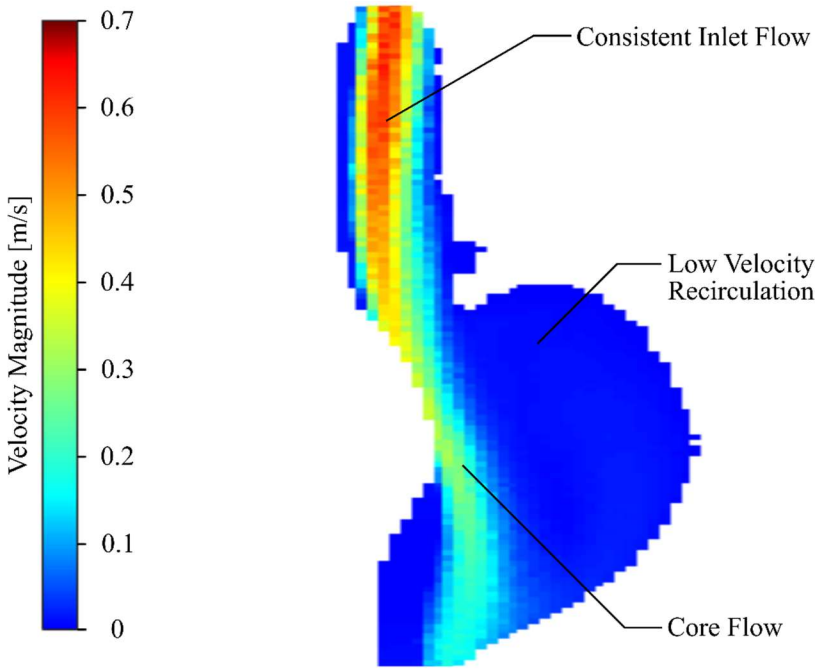

Figure 43: 4D MRI midplane contour

Figure 43 depicts a velocity field parabolic profiles at the inlet, reflecting the expected quadratic distribution of developed internal flows. Low-velocity zones associated with recirculation are also captured, providing key insights into flow behaviour within the AVM. The inlet flow progresses into the malformation, maintaining a core flow pattern. However, adjustments to the geometry to fit within the AVM bore reduced curvature in the vascular phantom, leading to diminished recirculation compared to the baseline scenario, which may be found in section 3.2. These geometric changes, along with spatial resolution constraints, limited the ability of the MRI to resolve near-wall velocities.

To verify the CFD results, Figures 44 and 45 present comparisons between the MRI and computational velocity fields. The CFD data was intentionally coarsened to match the MRI resolution. A section plane, shown in Figure 44 (a), was selected for clear comparison.

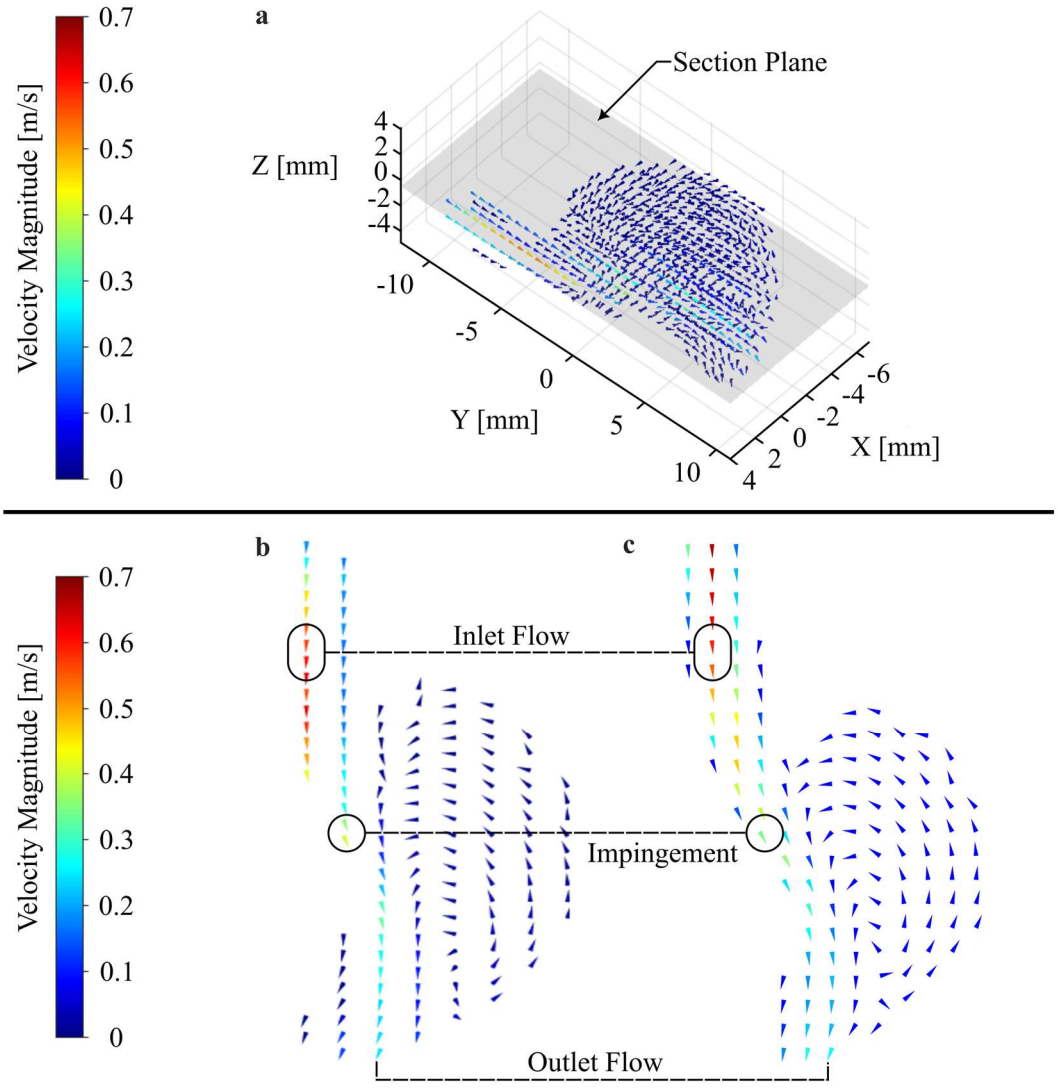

Figure 44: Comparison of MRI (b) and CFD (c) flow fields

Figure 44 demonstrates strong agreement between CFD and MRI datasets, with both capturing similar flow structures, velocity magnitudes and key features such as flow impingement on the AVM wall. Notably, the location and velocity magnitudes associated with this impingement shows consistency between the two datasets, reinforcing the computational model's accuracy. Vortical flow patterns also exhibit alignment in terms of magnitude and orientation, suggesting that CFD reliably simulates the AVMs internal flow.

Minor discrepancies, such as directional discontinuities at the aneurysmal apex and high-velocity core, are attributed to limitations in the MRI dataset, including masking inaccuracies and phase aliasing. These issues are explored further in Figure 45, which presents a planar streamline comparison.

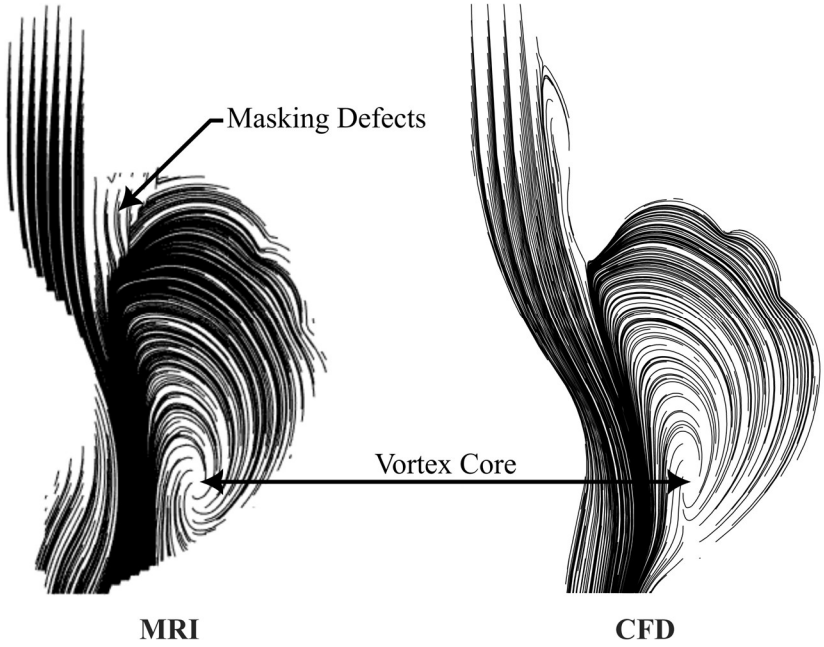

Figure 45: Planar streamline comparison

Figure 45 highlights coherence between the computational and MRI velocity fields, with the streamlines in both datasets showcasing similar patterns. Both datasets capture similar internal flow structures such as comparable streamline density distribution, curvature, and vortex core location. Furthermore, the computational and experimental models show this core forming in the lower section of the AVM, slightly to the right of the primary outlet flow stream and exhibiting a clock-wise circulation.

Differences at the aneurysmal zone apex are likely due to masking defects in the MRI dataset, which has assigned velocities to regions outside of the AVM geometry (air in the MRI bore), however, these discrepancies correspond to low velocities and minimally affect the overall flow comparison.

Figure 46 depicts a spatial map of the percentage difference in velocity magnitudes between the MRI and computational datasets. This comparison was achieved by aligning the 3D flow fields, followed by nearest-neighbour interpolation of the higher-resolution CFD data onto the MRI grid. This process allowed for a direct, point-by-point evaluation of discrepancies between the two velocity fields, offering insight into areas of agreement and divergence.

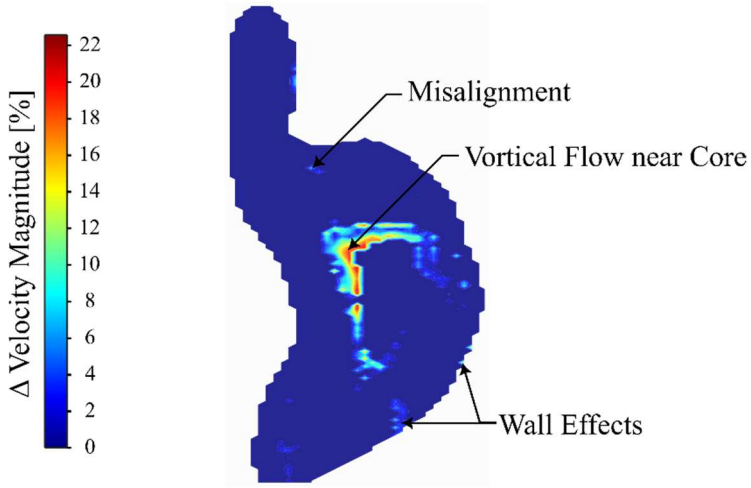

Figure 46: Spatial map of differential velocity magnitude

The spatial map in Figure 46 identifies three primary error sources:

1. The most prominent error is found in regions of vortical flow adjacent to the core flow, where steep velocity gradients challenge MRI accuracy.
2. Misalignment errors due to masking inaccuracies at the intersections between MRI and CFD dataset boundaries.
3. Near-wall regions where MRI resolution limitations affect data reliability.

Despite these sources of error, the overall agreement between the MRI and CFD datasets remains strong. The greatest error, approximately 22%, is localised, while most of the internal flow regions exhibit errors ranging from $0 - 2\%$. This indicates a prominent level of similarity and reliability in the computational model's representation of the baseline flow; hence the computational data is taken to be verified while the validation of the reliability of the coil and clotting models are presented in sections 3.1.1 and 3.1.2, respectively.

MRI limitations and future potential

While 4D MRI proved effective as a verification tool for CFD results, several limitations hinder its use as a comprehensive validation method. The primary challenge lies in achieving useful results at higher spatial resolutions. The resolution of the presented results is insufficient to capture boundary layer and near-wall velocities. This limitation is particularly evident at the AVM inlet, where impinging flow interacts with surfaces of high curvature, leading to signal degradation and data loss, as observed in Figures 44 and 45. Although the SLA-printed AVM geometry, constructed from high-resolution polymer resin, minimises scattering effects, the scanner's resolution remains the principal constraint at this scale, however it should be noted that this was primarily constrained due to time limitations and is not a technical or inherent limitation of the scanner.

Phase aliasing further complicates the data acquisition process. Custom unwrapping algorithms were applied to mitigate these errors, but the corrections remain limited by the constraints of the MRI's spatial and temporal resolution for the presented results. Masking defects also introduced discrepancies, particularly in high-curvature regions such as the aneurysmal apex, as seen in Figure 45, where velocity values were inaccurately assigned.

Addressing these limitations would enhance the utility of 4D MRI for validating CFD models. Improved spatial resolution would allow for more accurate representation of near-wall flows, while longer scan durations and averaging methods would mitigate signal degradation as exemplified by Zafar *et al* (2019) and thus serve to improve data gathered at higher spatial resolutions. If these challenges are overcome, 4D MRI could evolve into a robust tool for validating computational models in biomedical flow research, providing high-quality qualitative and quantitative insights into complex vascular dynamics.

3.2 Pathophysiological Flow

Pathophysiological flow refers to the natural, unembolised haemodynamics within blood vessels, occurring under diseased physiological conditions. In this context, it specifically refers to the blood flow through the AVM in the absence of embolisation or clotting phenomena. The unaltered flow field within the AVM under baseline conditions, as set out in section 2.5.2, is shown in Figure 47.

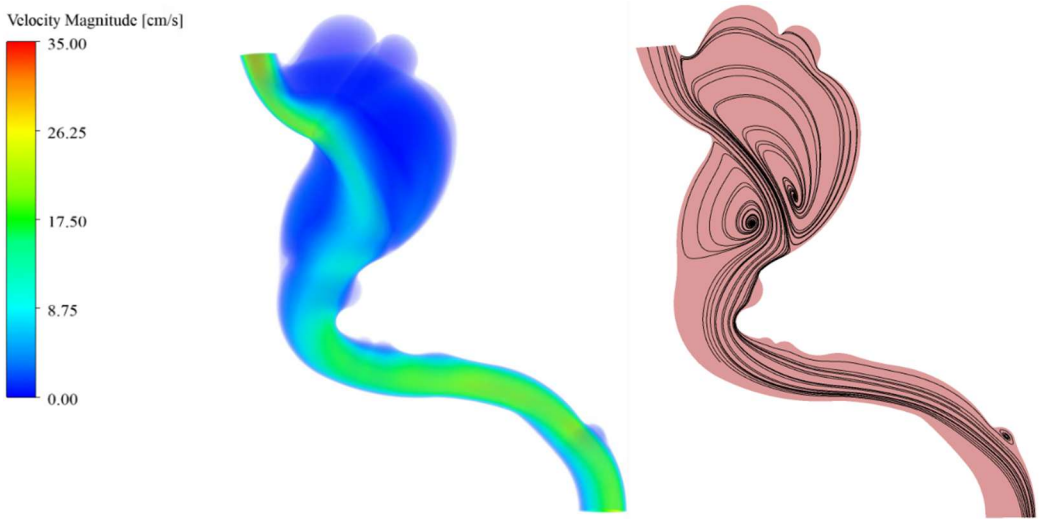

Figure 47: 3D velocity rendering (left) and midplane clipped velocity streamlines (right) of pathophysiological flow through the AVM

From Figure 47, a relatively high-velocity core flows centrally through the malformation, originating from the constrained arterial inlet and preferentially directing towards the venous outflow, in a similar manner to the flow discussed in section 3.1.3. The regions of lower velocity correspond to areas of recirculation, as depicted by the streamlines on the right, which arise primarily due to vessel curvature. These regions are of clinical significance, as the zones of recirculation exhibit low flow and shear rates, increasing the likelihood of clot formation. Additionally, high-curvature areas, coinciding with regions of slow flow, are prime sites for clot initiation due to reduced shear rates. This occurs because the concave wall geometry relative to the mean flow direction slows the velocity, hence lowering shear.

Establishing the baseline flow state is essential for accurately assessing the impact of embolisation procedures, clot formation, and the overall success of interventions. Both localised AVM flow and larger-scale flow parameters must be considered, as the introduction of embolisation coils and clot formation in the AVM significantly alters the pathophysiological flow by way of flow redirection through the feeder and draining vessels.

The aforementioned larger-scale flow parameters are herein defined as the AVM baseline values, derived from the pathophysiological flow field, and are summarised in Table 10. The flow variables selected to serve as the descriptors of the baseline state are the volume-averaged AVM shear rate ($\dot{\gamma}_{\mathrm{AVM}}$) and the volumetric flow rate through the malformation ($\mathrm{Q}_{\mathrm{AVM}}$). This is extended to include the clot volume in later sections.

Table 10: Baseline AVM flow properties

Property	**Baseline Value**
$\dot{\gamma}_{AVM}\ [s^{-1}]$	74.417
$Q_{AVM}\ [mm^3/s]$	1.458

The volume-averaged shear rate serves as an indicator of the velocity gradients within the AVM and reflects the degree of flow disturbance. Higher shear rates typically correspond to disrupted flow patterns, which are commonly observed under pathophysiological conditions in the presence of an AVM. Following embolisation, the shear rate is expected to decrease compared to the baseline pathophysiological flow due to the reduction in the overall velocity within the AVM, as flow is diverted into the parent and draining vessels. When comparing different embolisation cases, this trend in the overall reduction in shear rate is expected to continue as flow resistance is incrementally increased, however a higher post-embolisation shear rate may signify that the clot has successfully restricted high-velocity flow paths within the AVM, reflecting the desired outcome of effective embolisation. Hence, both a quantitative and qualitative evaluation of the AVM flow field is required to interpret flow reduction due to clot formation.

The AVM flow rate serves as the most powerful tool in assessing embolisation success, as it directly quantifies the degree to which blood flow through the AVM has been obstructed. Following the introduction of coils and subsequent clot formations, the flow resistance increases, causing a significant reduction in the AVM flow rate. This reduction is a hallmark of embolisation efficacy, as it indicates that blood is being diverted away from the AVM and redirected into parent and draining vessels. The ultimate goal of embolisation is to reduce the AVM flow rate to zero, representing complete occlusion and the effective elimination of the pathological AVM.

To facilitate meaningful comparisons, these metrics are consistently referenced against the pathophysiological flow, hereafter referred to as the baseline (B). Subsequently, the outcomes of various embolisation configurations can be more clearly interpreted, providing a more robust framework for evaluating procedural success.

3.3 Embolised Flow

Embolised flow, refers to the haemodynamic environment resulting from the introduction of the embolisation coil alone, i.e., in the absence of clotting effects. The insertion of coils by way of manually-fed catheter delivery is effectively random, thus six distinct embolisation cases are investigated to represent stochastic variations in coil configurations and evaluate the subsequent effect on flow characteristics.

The configurations include the insertion of one, two, and three coils, at different coil insertion angles. The number of coils selected was determined based on findings by Trerotola *et al* (2019), wherein a mean of 3 inserted coils were found to be sufficient for embolisation in all porcine cases investigated. Two distinct coil insertion angles were selected, namely $0°$ (straight) and $45°$ (angled) relative to the AVM inlet feeder axis. This selection is based on standard bent-tip catheter angles commonly used in clinical practice, as documented in microcatheter product catalogues (Endovascular Today, 2024).

The primary aim of this analysis is to evaluate the impact of coil quantity and insertion angle on the local flow and pressure within the AVM. The expectation is that the introduction of the single coil will result in the most substantial reduction in flow velocity, with subsequent additions of coils showing a diminishing effect. The insertion angle influences flow patterns indirectly by altering the final configuration of the coils, which affects their interaction with the surrounding fluid. This relationship highlights how coil positioning, determined by the insertion angle, governs the resulting haemodynamics.

A naming convention has been established for the different coil configurations. The single, double, and triple cases are denoted by the letters **S**, **D**, and **T**, respectively, followed by the insertion angle, e.g., the double-coil case with a $45°$ insertion angle is denoted as **D45**.

Figures 48 and 49 present detailed representations of the embolisation scenarios considered, including variation in coil insertion angles, featuring both the smoothed coil geometries and their discretised forms as translated into the solver accompanied by the surrounding streamlines. Additionally, the spatial variation in pressure along the length of each coil is evaluated by plotting the pressure drop as a function of coil length. The y axis represents the pressure [mmHg], while the x axis corresponds to the length of the coil [mm], aligned with the direction of blood flow. This pressure distribution provides insight into the local pressure gradients and allows for a clear assessment of how coil geometry and placement affects haemodynamics within the AVM.

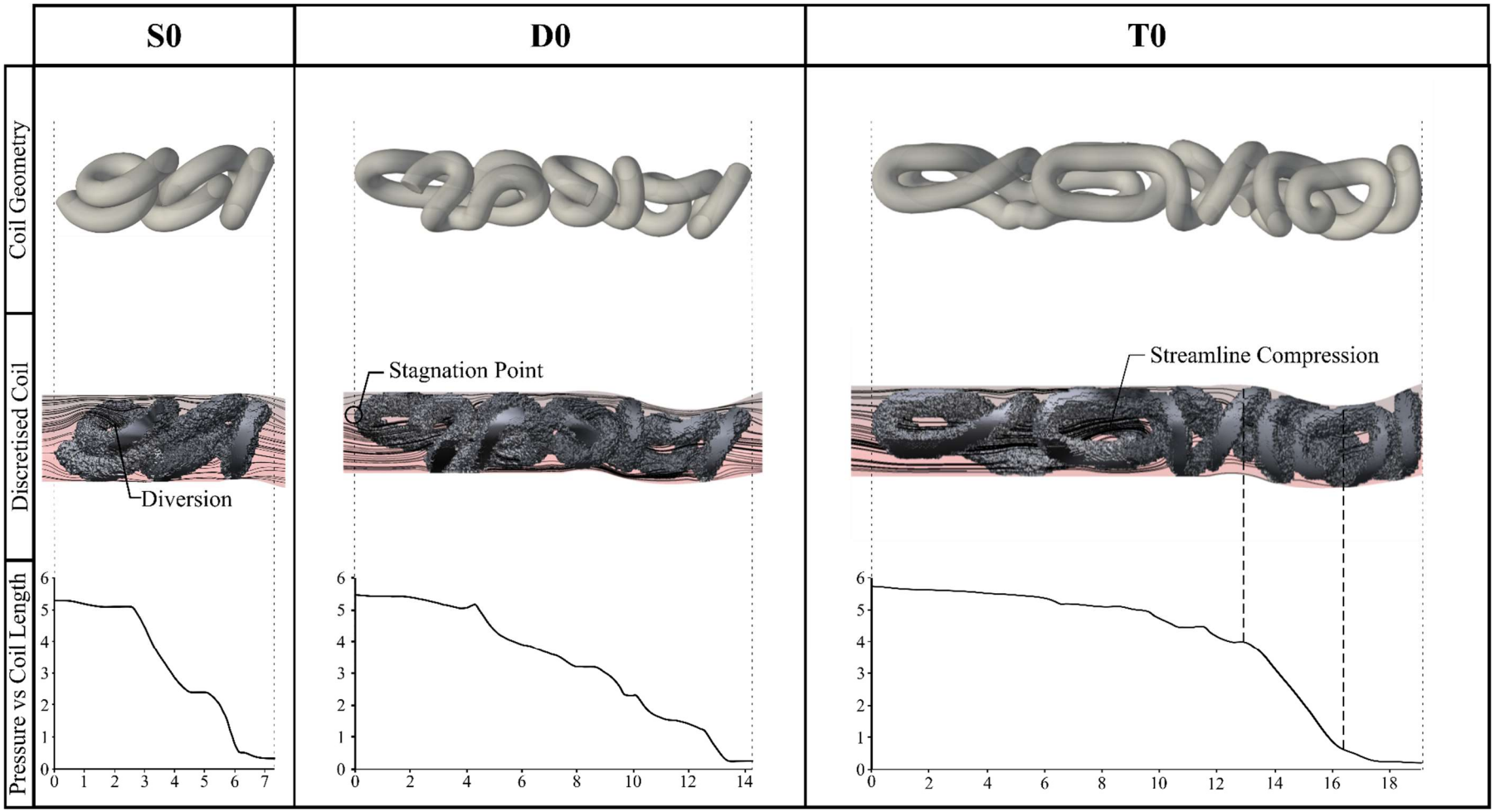

Figure 48: Straight catheter delivery embolisation cases (Pressure [$mmHg$] vs. Coil Length [mm])

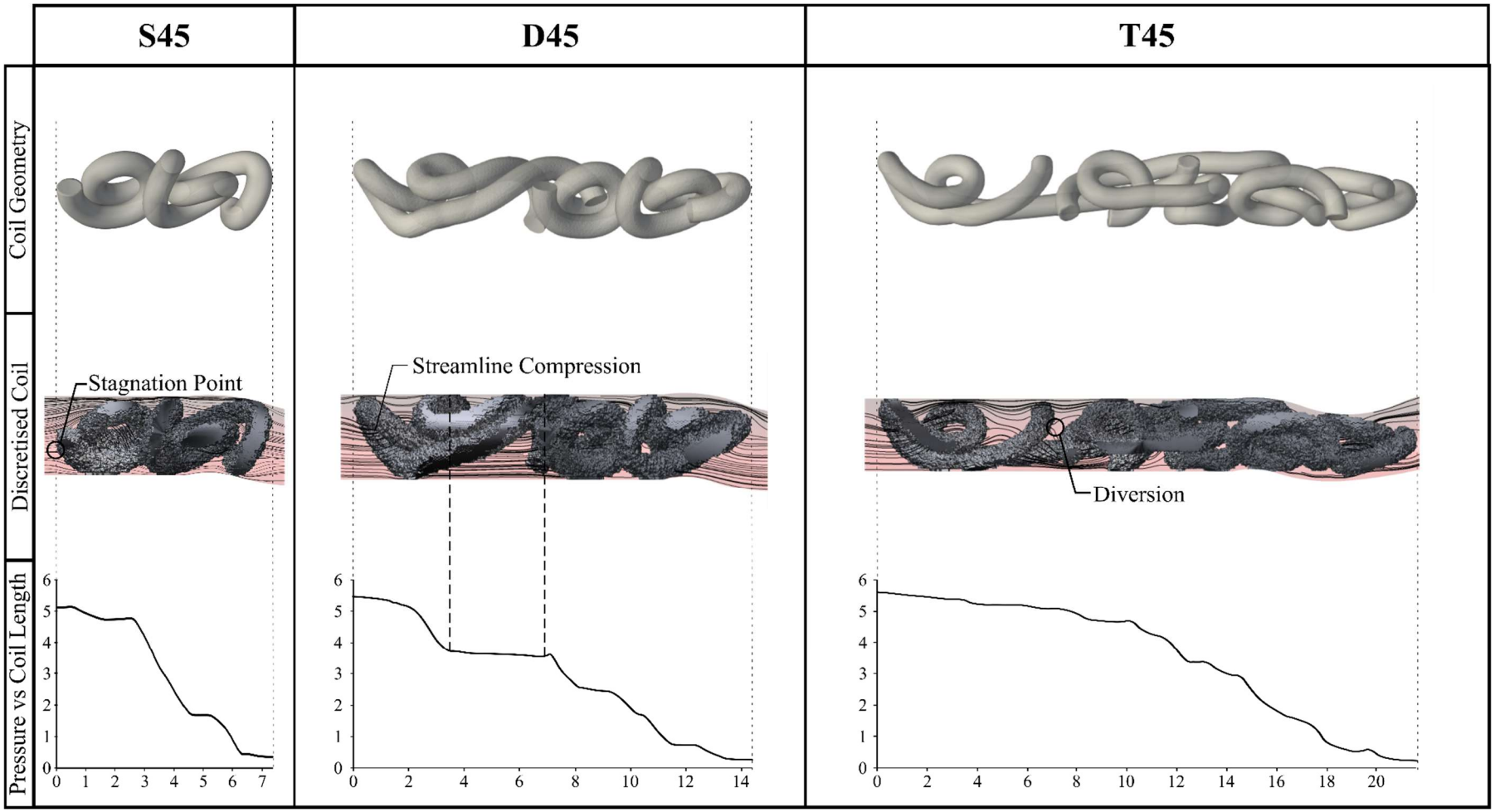

Figure 49: Angled catheter delivery embolisation cases (Pressure [$mmHg$] vs. Coil Length [mm])

The streamlines presented in Figures 48 and 49 substantiate the use of the non-uniform porous media model coil description as the method captures the most fundamental flow characteristics associated with the *in vivo* coil flow obstruction, i.e., stagnation and flow diversion. As streamlines encounter the coil surface, they either stagnate or divert, creating regions of low and high velocity around the coil. These behaviours are captured in the pressure and streamline distributions, where stagnation points, and areas of accelerated flow can be observed. The coil structure induces flow compression and elongation, increasing the local velocity and causing a corresponding pressure drop, which is particularly evident in the pressure versus coil length graphs, where pressure peaks are observed at stagnation points, followed by sharp drops as fluid accelerates around the coil.

The coil's geometry plays a key role in influencing these local pressure gradients, i.e., in regions with denser packing, higher resistance leads to more significant pressure drops, as seen in the T0 column of Figure 48. Conversely, in areas where the coil packing is less dense, the pressure drop is less pronounced, as shown in the D45 column of Figure 49. In the context of AVM treatment, the pressure drop induced by the coil serves to reduce the blood flow into the AVM and thus promotes the formation of downstream clots. The global flow rate reduction through the AVM is a result of the diversion of flow to the parent and draining vessels, which aids in occluding the abnormal vasculature.

Figures 50 and 51 illustrate that the pressure approaches zero for all cases from between $5 - 6$ mmHg, emphasizing that the pressure differential across the AVM is significantly lowered and exemplifying the diminishing effect of increasing the number of packed coils. This finding agrees with Piasecki *et al* (2020) which found that changing endovascular coil configurations *in vivo* caused no significant change in intra-aneurysmal pressure.

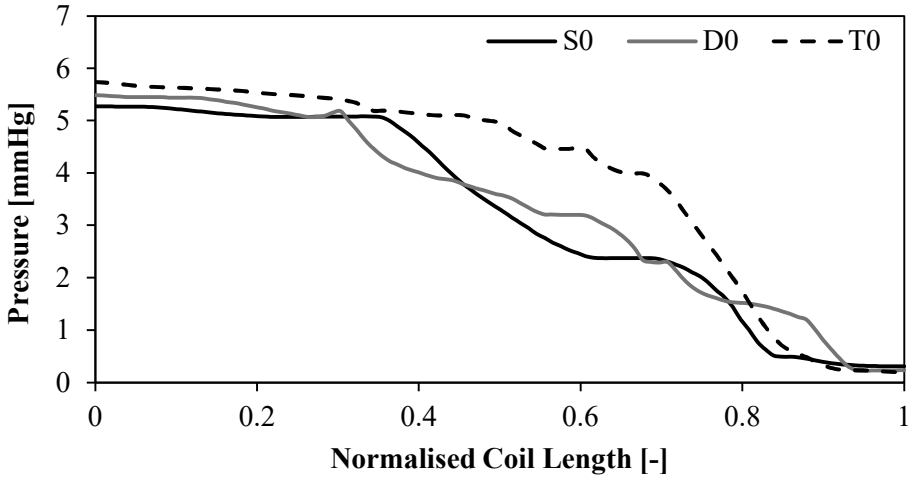

Figure 50: Straight insertion angle coil pressure drop

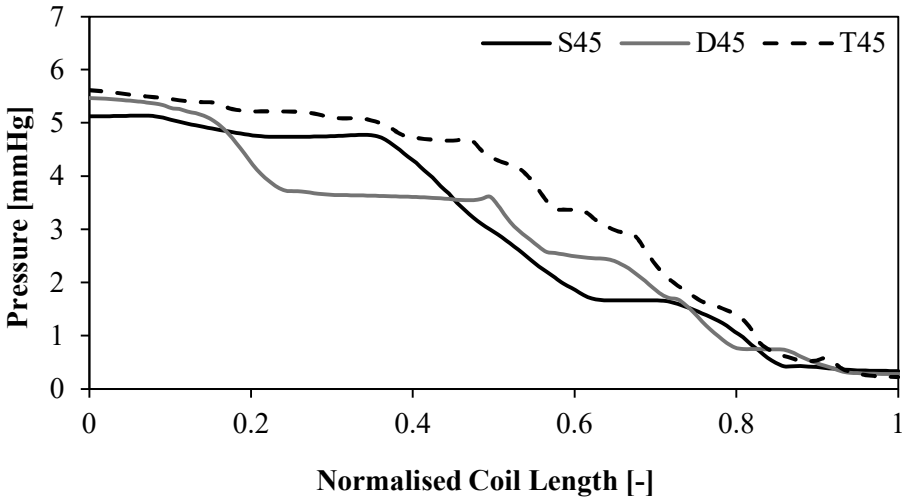

Figure 51: Angled insertion angle coil pressure drop

The analysis of overall pressure drops across the length of the coils, depicted in Figures 50 and 51, reveals a clear trend. As anticipated, the total pressure reduction increases with the number of coils inserted, with subsequent incremental changes in pressure drop between successive coils for both the straight and angled insertion scenarios. This observation could imply that a single coil might suffice for effective AVM occlusion. Nevertheless, to substantiate this hypothesis, it is necessary to correlate these findings with the reduction in AVM flow rate post-clotting for a more comprehensive assessment of AVM occlusion.

To better analyse the overall impact of the coil embolisations, with respect to one another pressure drop and AVM flow rate for each coil insertion are shown in Figure 52.

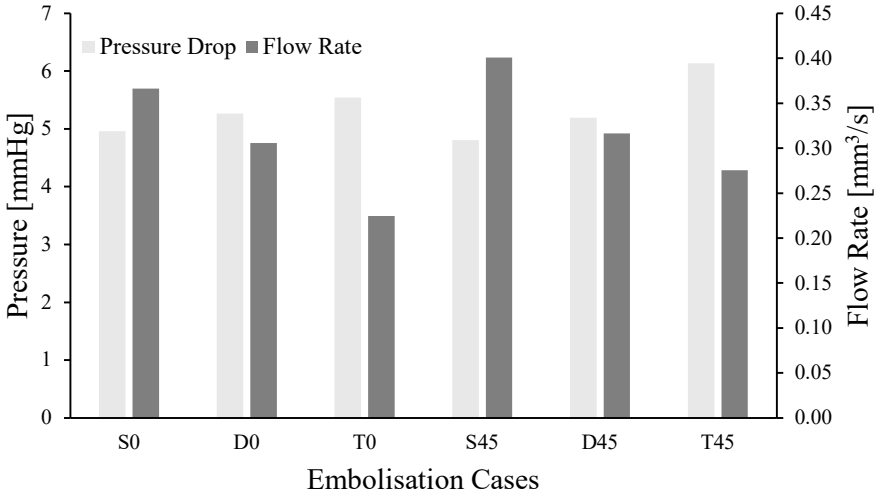

Figure 52: Flow variables for different embolisation cases

Figure 52 emphasizes the inverse relationship between the pressure drop across the coil and the flow rate entering the AVM. Specifically, as the pressure drop across the coil increases, the downstream pressure decreases, resulting in a diminished pressure gradient across the AVM. This reduced pressure differential translates directly into a lower flow rate through the AVM. This relationship is crucial for determining the success of AVM occlusion procedures, as lower flow rates are more likely to lead to successful embolisation.

Table 11: Coil packing densities

Case	S0	D0	T0	S45	D45	T45
Packing Density [%]	33.43	34.13	40.86	33.06	33.78	36.13

Table 11 presents the coil packing densities achieved for each coil configuration, defined as the percentage of the flow volume occupied by the coil within its bounding box. Packing density increases with the number of coils, reflecting clinical practice, where sequential coil placement enhances flow blockage. Notably, for the AVM case investigated, a straight insertion angle results in higher packing densities. This advantage likely arises from the vessel curvature near the deployment site, which influences coil configuration by inducing kinks as coils collide with the vessel wall. These collisions affect dynamic packing, promoting tighter configurations and enhancing flow obstruction.

A comparison of the six embolisation cases illustrated in Figure 52, in conjunction with the data presented in Table 11, indicates that the T0 configuration is the most effective in facilitating AVM occlusion. This stems from the greater number of coils employed in the T0 case as well as the higher coil packing density of 40.86%, which creates greater resistance to flow, a slightly greater pressure reduction and a lower flow rate. In contrast, T45 , which has the same number of coils but a lower packing density of 36.13% is less effective. This variation, resulting from the change in coil insertion angle, is similarly evident in the other cases. For instance, when evaluating S0 and S45 as well as D0 and D45, the angled insertion cases demonstrate lower packing densities, leading to a comparatively smaller pressure drop and a higher AVM flow rate, while the number of coils remains consistent.

3.4 Evaluation of Final Embolised States

The success of coil embolisation procedures relies on more than just the mechanical blockage provided by the coils. It is shaped by a complex interplay of factors, including the number of coils deployed, the extent of clot formation, and the subsequent alterations in flow dynamics. A thorough evaluation of embolisation effectiveness involves detailed analyses of flow patterns and the combined impact of these embolisation mechanisms.

3.4.1 Comparison of baseline and single coil embolised flow

A comparison between the uncoiled baseline flow (B) and the S0 case serves as a reference for the current evaluation. Figure 53 illustrates the distinct flow patterns in these scenarios, highlighting the clotting effects induced by the application of the coil.

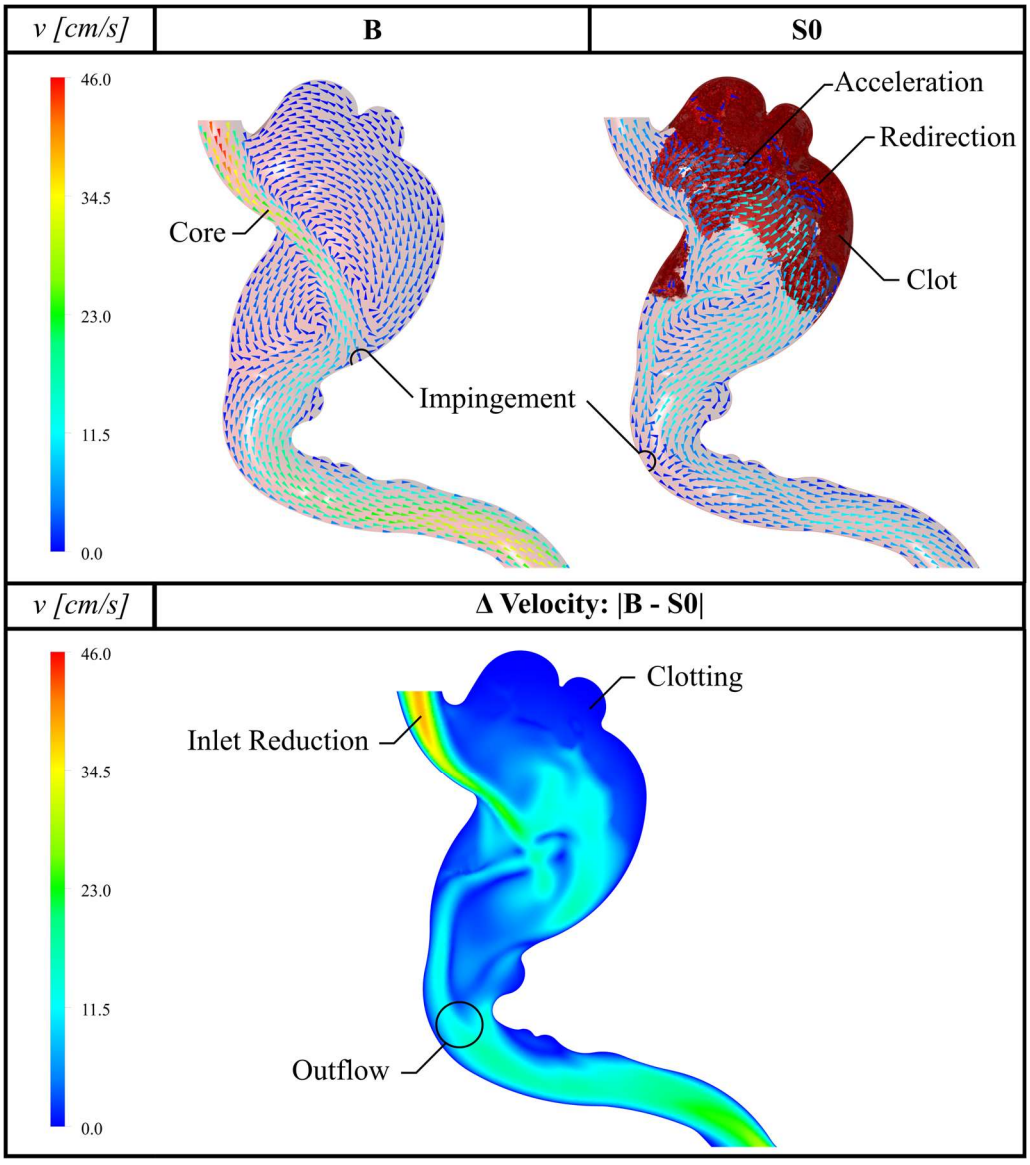

Figure 53: Comparison of baseline and S0 AVM flow field

In Figure 53, as seen in Figure 47, the baseline flow demonstrates a clear and predictable pattern. At the section plane, a relatively high-velocity core moves within a toroidal vortex, which appears as two counter-rotating planar vortices of lower velocity, representing a stable flow condition under normal circumstances. However, in the S0 case, the overall flow velocity has drastically reduced due to the combined effects of the coil placement and clot formation. This reduction is particularly notable at the inlets, where the velocity decreases from $46\ \mathrm{cm/s}$ in the baseline flow to approximately $10\ \mathrm{cm/s}$ in the S0 case.

The planar vortices in the baseline case are present in S0, but they are irregular and significantly diminished in strength. As a result, flow velocities are more distributed and exhibit less coherence in the S0 case compared to the baseline flow state. Around the clot, flow velocity drops drastically, as blood is redirected around the high-resistance regions formed by the clot volume. Some narrow regions near the clot front experience local acceleration, indicating that the remaining flow jets around the clot as the pathways available for the blood to pass through are constricted. Sharper velocity gradients appear near these clot boundaries due to the flow being actively diverted.

Furthermore, the reduced flow in the recirculation zones highlights that flow detachment near the clot's larger formations is contributing to the flow stagnation. This reinforces how clot formations create a positive feedback loop where regions with low flow tend to be conducive to clotting, which in turn slows flow further, facilitating additional clot formation. This feedback mechanism is also clear in the subtraction map, wherein the regions corresponding to clotting exhibit minimal changes between the flow states.

The subtraction offers insight into the most significant differences in the AVM flow fields. The most substantial variations occur near the inlet and within the core region of the baseline flow, where velocity has drastically reduced. The draining flow exhibits a substantial change in the flow distribution in the lower section of the AVM, where the exiting flow exhibits both an outflow and inflow as a result of the change in the impingement area between the two flow states.

The overall effects of coil embolisation and clot formation in the S0 case highlight significant flow deceleration and redistribution within the AVM. These changes provide a clear indication of how mechanical interventions such as coil embolisation can substantially alter local haemodynamics, achieving their clinical goal of reducing blood flow to a malformation. This understanding is essential for optimising embolisation strategies to ensure maximum occlusion and successful clinical outcomes.

The overall effects are further interrogated using the changes to the baseline AVM flow properties. These are presented in Table 12.

Table 12: Change in AVM baseline properties

Property	Baseline	S0	Difference [%]
$\dot{\gamma}_{AVM}\ [s^{-1}]$	74.417	50.112	32.66
$Q_{AVM}\ [mm^3/s]$	1.458	0.322	77.91

The volume-averaged shear rate within the AVM demonstrates a significant reduction of 32.66%, which can be attributed to the combined effects of coil placement and clot formation. These effects suppress flow velocity, thereby reducing velocity gradients that contribute to elevated shear rates within the malformation. The coil serves as a physical barrier that disrupts the natural flow patterns, while clot formation amplifies this effect by further obstructing flow.

Similarly, the AVM flow rate exhibits a substantial decrease, with the coil alone reducing the flow rate to $0.336\ \mathrm{mm}^3/\mathrm{s}$ prior to the onset of clotting as opposed to $0.322\ \mathrm{mm}^3/\mathrm{s}$ post-clotting. This underscores the primary role of the coil as the initial and dominant means of flow obstruction. It is this interaction between the coil implantation, the subsequent clot formation and the overall changes in AVM flow rate, that serves as the mechanism by which embolisation procedures may be assessed as successful, as discussed in section 3.4.4.

3.4.2 Impact of coil packing on flow and clot formation

The degree of coil packing within the AVM influences both haemodynamics and clot development. As coil packing increases, the obstruction to blood flow becomes more substantial, leading to marked reductions in the AVM flow rate. These changes in flow promote an environment conducive to clot formation and resulting in larger stable clots.

Having established the pressure drops and flow reductions caused by the coils in conjunction with the overall flow changes related to embolisation as discussed in section 3.4.1, the following will shift focus toward a comparison of the different embolisation cases. This comparison will separately evaluate the straight and angled coil insertion groups to analyse the impact of varying the number of coils within each series. Additionally, it will provide a comparative assessment of how changes in the insertion angle affect the AVM flow. The resultant clot formations and AVM flow fields are depicted in Figure 54.

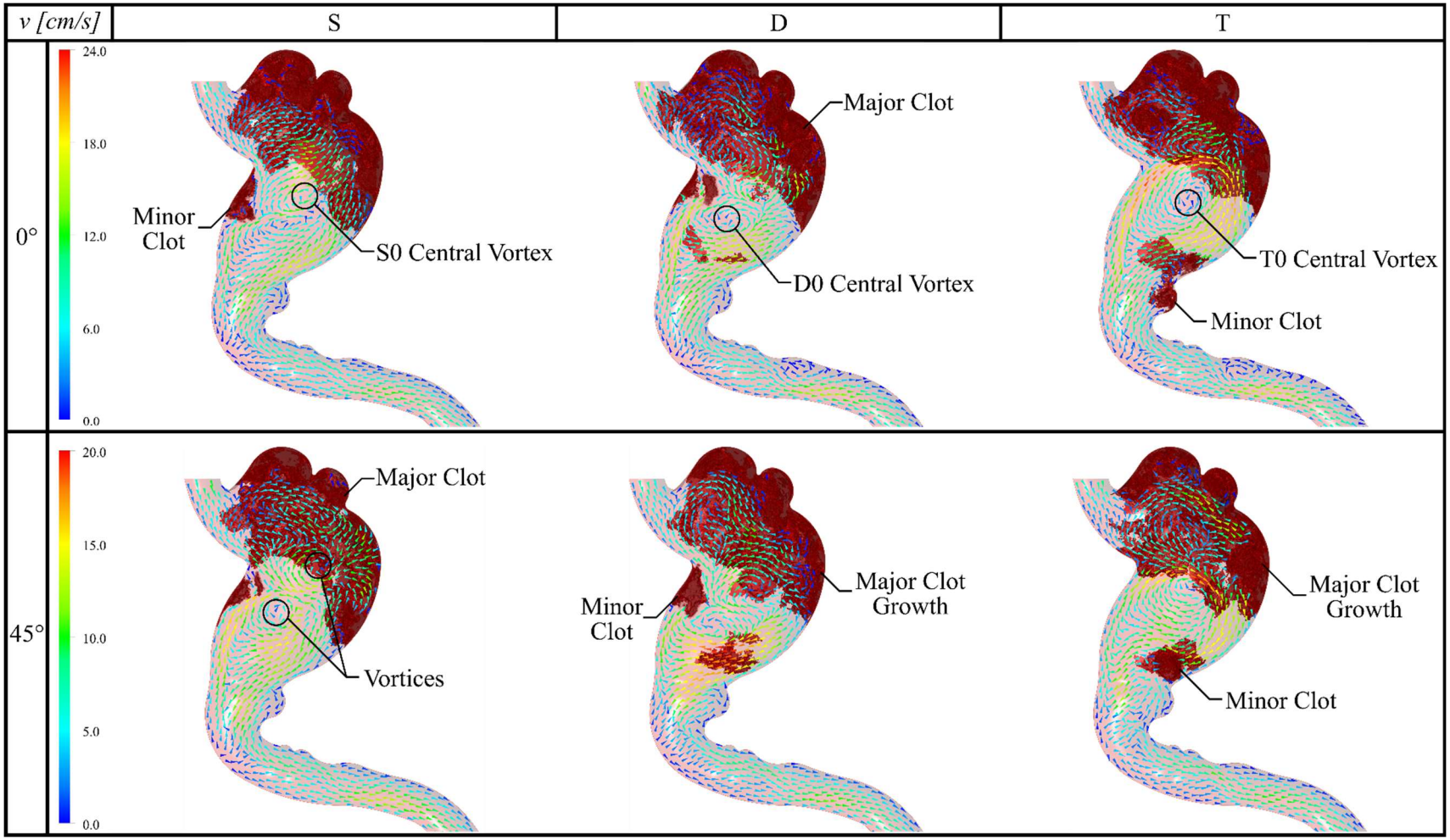

Figure 54: AVM flow for all coil configurations

0° angle of insertion series (S0-D0-T0)

As shown in all cases, the major fibrin clot formation within the AVM is primarily located at the top right of the malformation, denoted as "Major Clot" in Figure 54, and thus is in the area of recirculation with the lowest shear similar to that encountered by Sakariassen *et al* (2014). The size of this clot increases with the number of inserted coils. This formation highlights the relationship between coil packing and flow resistance within the malformation. Furthermore, the 0° series highlights an important factor in total clot size within the malformation, the location and distribution of the clot.

The stable major clot encroaches on the malformation inlet, which is a region of high flow velocity, as the number of coils increases. Clot formations in this constricted area heighten the potential for total vessel occlusion, which would result in the most significant reduction in AVM flow. However, this region also experiences the highest shear rates as the clot nears the inlet in successive cases. Consequently, the increased shear at the leading edge of the clot inhibits further growth and raises the possibility of fibrinolysis.

A secondary observation, particularly in case T0, is the strengthening of the central vortex as the coil count rises. In T0, the vortex results in relatively higher velocity circulating flow, preventing the formation of the minor clot on the left side of the malformation where flow separation previously occurred in the S0 case.

45° angle of insertion series (S45-D45-T45)

Similar flow characteristics as discussed for the 0° of insertion cases may also be found in the 45° cases, e.g., the strengthening of the central vortex and its impact on the major clot formation as well as the change in location of the minor clot growth from the left to the right wall of the malformation. Furthermore, the distribution of the major clot shows that growth (referring to the change in total clot size between cases) is consistently focused on the right of the malformation, away from the inlet, as noted for cases D45 and T45.

Major clot formations in this region would result in a marginal increase in the overall flow resistance of the malformation in comparison with those near the inlet as was discussed for the straight angle cases. This observation is similar to findings regarding clot formation in proximal (upstream/supply) vessels versus distal locations in the brain from Sillanpää *et al* (2013). This would suggest that, for the stochastic cases under consideration, the angled coil embolisation cases may have a comparatively lower effect on flow reduction and therefore may exhibit higher intra-AVM flow rates. These initial observations are supported by and expanded upon through the evaluation of the AVM baseline values.

Baseline value comparison

Assessing the overall flow quantities, i.e., the AVM baseline values, allows for the determination of the comparative success of the embolisation cases. These baseline values are given in Table 13.

Table 13: Baseline values

Property	S		D		T	
	0	45	0	45	0	45
Clot volume [mm^3]	296.30	321.24	329.21	309.55	339.67	301.74
$\dot{\gamma}_{avm}$ [s^{-1}]	50.11	55.72	55.09	53.37	59.60	57.57
Q_{AVM} [mm^3/s]	0.322	0.331	0.286	0.285	0.224	0.257

The comparison of the 0° series' baseline values demonstrates key trends in haemodynamic parameters that highlight the influence of increasing coil numbers on occlusion efficacy. A notable increase in clot volume is observed as coil numbers increase with S0 exhibiting the smallest clot volume and T0 exhibiting the largest at $339.67\ mm^3$. This progressive increase in clot volume with increasing coil number shown for the 0° series, further emphasizes the increase in the overall AVM flow resistance with an increasing number of inserted coils, evidence of which is shown in cases like D0 and T0, wherein the larger clot volumes are indicative of a local low shear environment.

In contrast to the 0° coil insertion series, clot volume decreases with increasing coil number in the angled coil insertion series. This trend is primarily due to the preferential formation of clots on the right side of the AVM, as shown in Figure 54, where clot volume increases with additional coils but has minimal impact on overall flow reduction. This highlights an interplay between the extent of clotting and its location, as the localised clot formation does not obstruct the AVMs primary flow path and thus does not contribute significantly to the positive feedback loop which accompanies clot formation.

The general trend in AVM shear rate shows an increase with a greater number of inserted coils, suggesting that as more coils and/or clots are present, higher velocity flows are hindered. This increase in shear rate could result from a combination of factors, including the development of a greater velocity gradient near the clot and vessel walls, as well as a reduction in the distance over which the velocity changes occur, such as the flow acceleration near the clot surface. Both of these arise as a result of clotting and contribute to the observed rise in shear rates within the flow field.

Hence, larger clot volumes are typically associated with higher shear rates, but there is a complex interaction between the number of coils packed, clot formation, and their effects on the overall shear rate. This is evident in the 45° insertion series, wherein S45 has the largest clot volume at $321.24\ mm^3$, yet T45, exhibits a higher shear rate.

Meanwhile, D45 shows a lower shear rate than S45 despite having more clotting than T45. This suggests that while increasing the number of coils consistently raises shear rates, as seen in the 0° series, comparatively smaller clots may still result in decreased shear.

The flow rate through the AVM consistently decreases as the number of coils increases, reflecting effective occlusion of blood flow. In the 0° series, S0 shows the highest flow rate, while T0 achieves the overall lowest at $0.224\ mm^3/s$. A similar trend is observed in the angled series, though with higher overall flow rates. This steady reduction underscores the role of coil embolisation and clot formation in diverting blood away from the AVM. Clinically, these findings are particularly significant for T0, as they indicate a strong likelihood of complete flow blockage. The assessment of the investigated embolisation cases utilising a clinical metric is detailed in section 3.4.4.

Impact of coil insertion angle on flow and clot formation

The overall trends from the data in Table 13 indicate that the 0° coil insertion cases consistently outperform the 45° cases across nearly all measured metrics. This superiority is evident for all configurations, however, there are notable exceptions, such as the single coil AVM shear rates and the double coil AVM flow rate. Specifically, for the single coil cases, S45 shows a significantly larger clot volume due to preferential clot formation on the right side of the AVM, comparable to D0, resulting in a higher shear rate. Additionally, while D45 exhibits a slightly lower flow rate than D0, the difference is marginal, suggesting the two cases have comparable performance, likely due to similar coil packing densities as outlined in Table 11.

These findings align with expectations discussed in section 3.3, reinforcing that the 0° insertion angle consistently delivers better performance. This is likely attributable to the more effective and denser packing configurations obtained through the use of the 0° coil insertion angle, which enhances flow diversion and redirection away from the AVM and into its feeder vessels, exhibiting agreement with the trend found in Morales *et al* (2011). Thus, for the stochastic cases investigated, the 0° series demonstrates an advantage over the 45° series in achieving successful embolisation outcomes.

3.4.3 Qualitative baseline flow comparison

Moving on from the inter-case comparison, a qualitative and quantitative review of the changes in the AVM flow field are considered in sections 3.4.3 and 3.4.4 respectively. The qualitative comparison is achieved through the analysis of differential velocity maps, as shown in Figure 55. These visualisations reveal key insights into how flow dynamics are disrupted by the interventions, providing a qualitative basis for assessing the likelihood of success of each case.

The general trend observed in the differential maps exhibit a noticeable reduction in velocity of the core flow as compared to the baseline flow, emphasizing the successful obstruction of high-velocity blood streams. The inlet of the AVM, as denoted for case S0, consistently shows the greatest reduction in flow, indicating that the combined effects of the coil implementation and clot formations significantly reduce the overall AVM flow rate. Regions displaying minimal changes in velocity delineate areas where clot formation has occurred as these correspond to baseline low-velocity zones, diminishing further blood movement. These observations are the clearest indicators of the effective disruption of the AVMs pathological shunting, diverting blood away from the malformation.

The most substantial flow reduction near the impingement point for the baseline flow, as discussed in section 3.4.1 and demarcated for cases D0 and D45, is not evident in the single coil scenarios. This indicates that a single coil is insufficient to significantly disrupt the baseline flow at this location. In contrast, both double coil cases demonstrate a clear reduction in velocity around the impingement zone. Among the triple coil scenarios, T0 exhibits the most significant change, both in terms of the velocity magnitude and the spatial extent of the affected area. The ability of T0 to produce such extensive flow reduction further supports its potential for clinical success, as it suggests a more robust blockage and a higher chance of complete occlusion.

As shown for cases D0 and D45, the degree of recirculation on the lower left side of the AVM has a significant impact on the minor clot size, wherein stronger recirculation results in greater velocities and thus higher velocity gradients at the minor clot zone. Furthermore, a stronger recirculation here is associated with a reduced driving pressure over the AVM and suggests a more successful embolisation. Notably, while the impingement reduction for D45 is greater, it has a lower exit recirculation strength, potentially highlighting the reason for the similarity between the D0 and D45 cases as discussed in section 3.4.2.

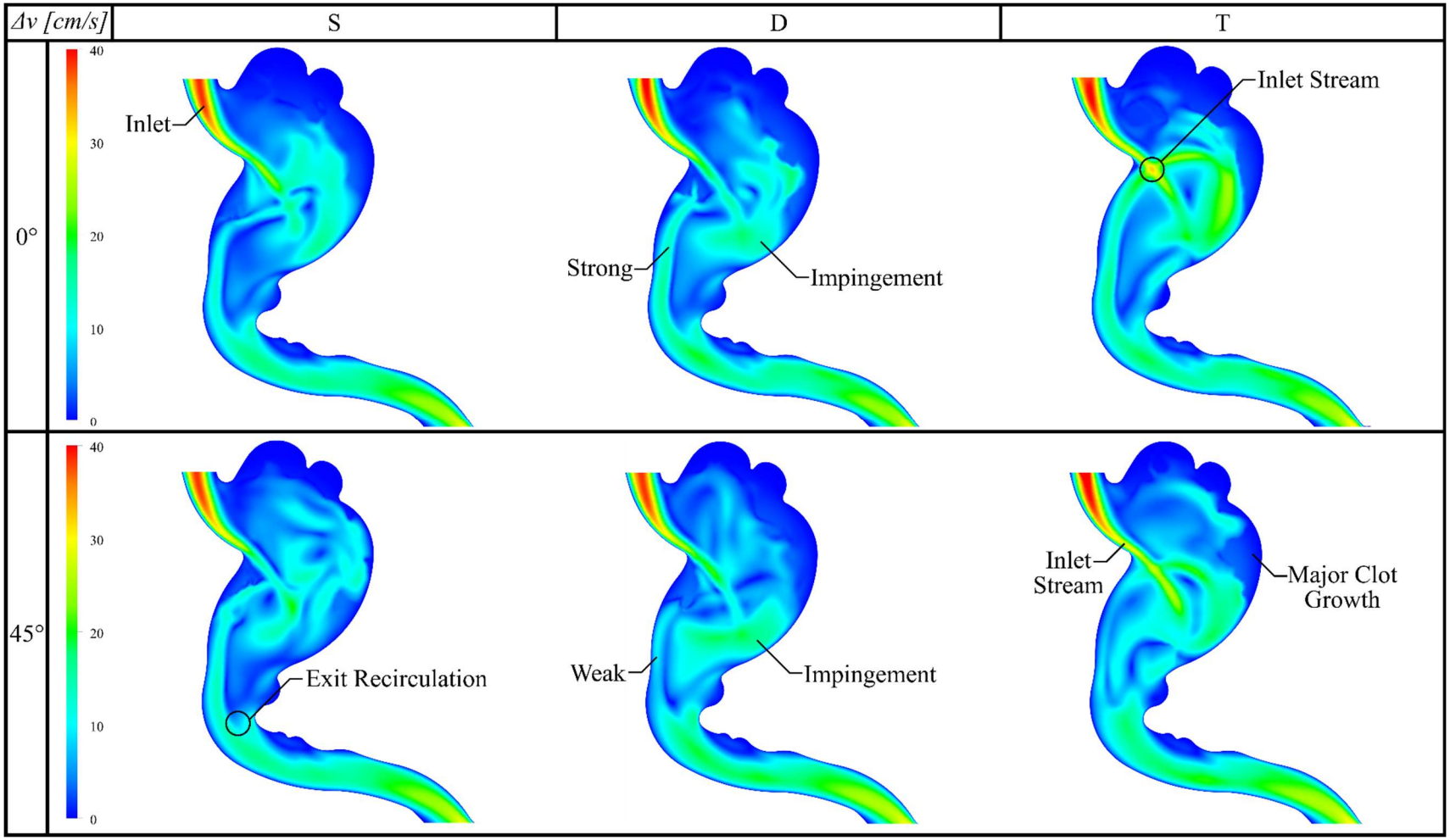

Figure 55: Differential velocity maps for all embolisation cases

The major clot formation observed in case T45, as discussed in section 3.4.2, is primarily concentrated on the right side of the AVMs aneurysmal zone. While this localised clotting does contribute to flow reduction, it is noticeably less effective than the clotting near the inlet region seen in case T0. In T0, the reduction in flow velocity is both more substantial in magnitude and more widespread, indicating a greater impact on overall blood flow.

Finally, the overall success of the embolisation cases may be assessed by the degree to which flow is perturbed and hence reduced in the inlet stream. As shown in Figure 55, and supported by the values from Table 13, the extent to which the inlet stream or core of the AVM baseline flow is differentiated increases from the single coil to the triple coil cases for both the 0° and 45° coil insertion angle series.

Ultimately, T0 and T45 show the most substantial reduction in the inlet stream, both in magnitude and area with T0 having a greater impact than T45. This obstruction is clinically significant because reducing the overall inlet flow can significantly impact the overall perfusion of the AVM, indicating successful coil embolisation.

Having evaluated the visual changes in the AVM baseline flow due to the application of the different embolisation cases, 3.4.4 aims to quantify and discern the success of these procedures based on a clinical metric.

3.4.4 Clinical evaluation of embolisation success

The flow variations explored in sections 3.4.1 through 3.4.3 offer valuable insights into the underlying physics governing changes in the AVM during embolisation, however these changes are more or less case-dependent, i.e., they are largely influenced by the specific vascular geometry and curvature. The clinical significance of the different embolisation scenarios is ultimately quantified by the reduction in flow rate through the AVM, relative to the baseline case.

As outlined in section 1.3.1, the primary clinical method for assessing intra-operative success during AVM occlusion involves the visual evaluation of contrast flow through the embolisation coil. This is typically conducted using Digital Subtraction Angiography (DSA), a technique where real-time imaging of the vessel is achieved via Computed Tomography (CT), with surrounding tissue digitally subtracted to enhance the clarity of the vascular structures. During this procedure, a contrast agent is introduced into the vasculature, allowing clinicians to determine the success of the embolisation based on the absence of visual contrast distal to the occlusive coil. This contrast imaging is typically conducted both intra-operatively and for long-term post-operative follow-up.

A variety of different contrast agents are used for intra-operative and post-operative CT scans; however, the most commonly used contrast agent is iodine in various concentrations and mixtures due to its water-soluble nature and limited risk to patients. CT imaging may be described as an advanced post-processing medical imaging modality which typically operates on the basis of x-ray imaging. Iodine has a high atomic number, which makes it highly effective at absorbing x-rays, which allows for the enhancement of the contrast of x-ray images, allowing for a clearer differentiation between different tissues, and in this case between blood flow and the surrounding anatomy.

An example of the CT contrast used by the DGMC is the VISIPAQUE^{TM} iodixanol contrast from GE Healthcare, with an iodine concentration of $320\ \mathrm{mgI/ml}$. Assuming based on the desired clinical imaging state (Kaproth-Joslin *et al*, 2022; Lieber *et al*, 2009), that the contrast agent mixes completely with the arterial blood flow prior to entering the AVM feeder vessel, and that the laminar flow consistent throughout the arterial domain ensures an even distribution of the contrast, a direct comparison between the contrast concentration and the flow rate entering the AVM feeder may be made such that the percentage flow rate reduction will correspond to an equal reduction in contrast concentration.

The limit of detectability (LOD) of iodinated CT contrast in blood has been found to be approximately $0.8\ \mathrm{mgI/ml}$ in vessels with a diameter of $3\ \mathrm{mm}$, and $10\ \mathrm{mgI/ml}$ in vessels with a diameter of $1\ mm$ in Heshmat *et al* (2023) and Taylor *et al* (2019). The trend in both LOD and HU with decreasing vessel diameter has been fitted with a decaying exponential function as shown in Eqn 10. This form is derived by considering that x-ray attenuation has an inversely exponential relationship to scan depth (Brown *et al*, 2022; Darling *et al*, 2009), hence when isolating vessels with DSA, this law may be applied equivalently.

$$\mathrm{C_{min}} = 34.17\mathrm{e}^{-1.23(\emptyset_v)} \qquad \dots\dots\dots\dots 10$$

Given that the coils are present and complicate visualisation, their effect has been captured by scaling down the effective diameter of the feeder vessel in this area to 1.8 mm, thus resulting in the effective limit of detectability being $3.7\ \mathrm{mgI/ml}$. The baseline flow was found to have a flow rate reduction between the arterial and AVM feeder of approximately 87%. Applying this directly to contrast reduction, the initial contrast concentration in the AVM feeder without coiling is $20.8\ \mathrm{mgI/ml}$, hence any flow rate reduction greater than 82% will be taken as successful in occluding the AVM. The percentage flow rate reductions for each embolisation case are given in Figure 56.

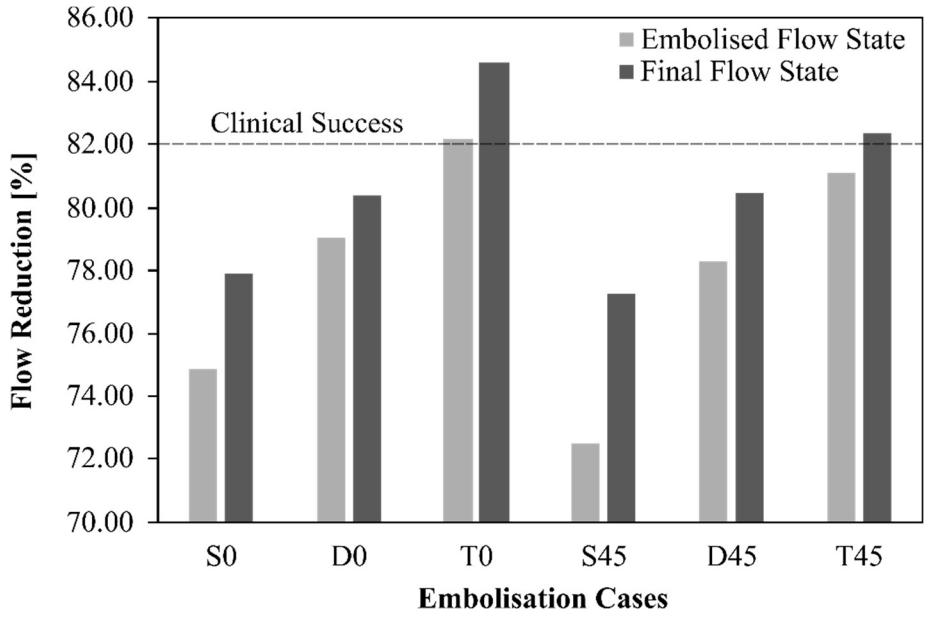

Figure 56: Clinical evaluation of embolised states

As illustrated in Figure 56, the triple coil configurations (T0 and T45) demonstrated success in achieving significant flow reduction, with the T0 case yielding the most pronounced decrease in flow rate. Furthermore, the analysis of the embolised flow state, which represents flow before clotting happens (as the operation is completed before the onset of clotting), indicates that the T0 configuration alone will be deemed a successful procedure.

This finding aligns with clinical practices where vascular specialists emphasize the necessity of using multiple coils to achieve effective embolisation (Dr Cecil Mosimanegape Pule, personal communication, October 17, 2024), particularly for complex cases on this scale. Thus, the superior performance of the triple coil setup, especially the T0 configuration, reflects standard procedural approaches, where achieving sustained flow reduction through the packing of multiple coils is critical for treatment efficacy. This complements the findings of Trerotola *et al* (2019) wherein a mean three coils were consistently sufficient for embolisation as mentioned in section 3.3.

T0 is not only the most effective configuration but also the most robust, offering the highest level of confidence for successful embolisation. In contrast, while the T45 configuration also achieved success, this outcome was contingent upon clotting effects. It must be noted at this stage that the visual inspection that is carried out during the procedure is subjective and could be affected by various factors such as the ambient conditions in the theatre, the model and resolution of the scanner, the accessibility of the surrounding vasculature for contrast injection as well as inter-observer biases.

3.5 Impact of co-morbidities

Further clinical evaluation of the embolised states with varied flow conditions has been included so as to extend the applicability of the model. Several vascular co-morbidities can coincide with the presence of an AVM, potentially influencing the success of the embolisation procedure. Two additional cases were considered where the boundary conditions for the AVM parent vessels were adjusted, in relation to the standard reported in section 2.5.2, to account for altered flow states, namely arterial hyper - and hypotension.

3.5.1 Arterial hypertension

Hypertension is the general term attributed to raised blood pressure and has several causes, including atherosclerosis: aortic stenosis: hypertensive heart diseases and renal artery stenosis etc. (Oparil *et al*, 2018). Taking a conservative approach, the highest pressure benchmark associated with hypertension is anything greater than $140\ \text{mmHg}$ or $18665\ \text{Pa}$, which is applied as the initial gauge pressure, while the velocity was scaled to $0.3645\ \text{m/s}$, assuming a constant baseline flow resistance, through the application of Eqn 11, whereby the quadratic relationship between pressure drop and velocity is maintained.

$$\frac{\Delta P_{\text{hypertensive}}}{\Delta P_{\text{baseline}}} = \frac{v^2_{\text{hypertensive}}}{v^2_{\text{baseline}}} \quad \text{… … … …11}$$

The final changes in the success of the embolisation cases are subsequently presented in Figure 57.

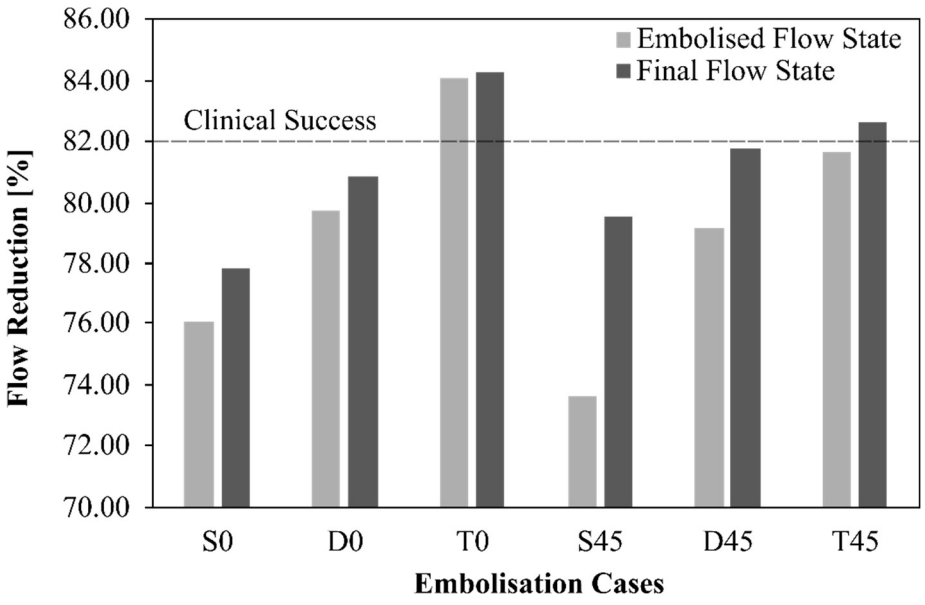

Figure 57: Evaluation of hypertensive embolised states

The success of embolisation in hypertensive cases mirrors that of the standard condition cases explored in section 3.4.4, as only the T0 and T45 scenarios were determined to be effective. While it is typically expected that hypertensive conditions would reduce long-term embolisation efficacy (Kim *et al*, 2021), this suggests that the increased flow does not significantly affect the outcomes for the cases under investigation. However, coil-induced flow reduction is more pronounced, while clotting contributes proportionally less. This may be associated with the coils' ability to block higher velocity flows, reducing them to levels similar to those observed in the standard cases. Nevertheless, this increased blockage raises shear rates within the AVM and allows higher flow rates, resulting in less clot formation, leading to a smaller reductions in flow related to clot structures, while the coils generate larger overall reductions due to the higher input velocities compared to the standard cases.

3.5.2 Arterial hypotension

Hypotension is the general term attributed to low blood pressure and is associated with diseases like septic shock; bradycardia; anaphylaxis and congenital heart defects etc (Sharma *et al*, 2023). For cases such as hypotension, blood pressure may decrease in one part of the lesion while potentially increasing in another. In the current context, reducing the inlet pressure is a logical approach to simulate hypotension, as it directly influences the driving pressure into the lesion, mimicking the systemic decrease in perfusion pressure observed in hypotensive cases. The most prevalent benchmark associated with hypotension is anything less than $65\ \mathrm{mmHg}$ or $8666\ \mathrm{Pa}$, which is once again applied as the initial gauge pressure, while the resultant scaled velocity is $0.2484\ \mathrm{m/s}$.

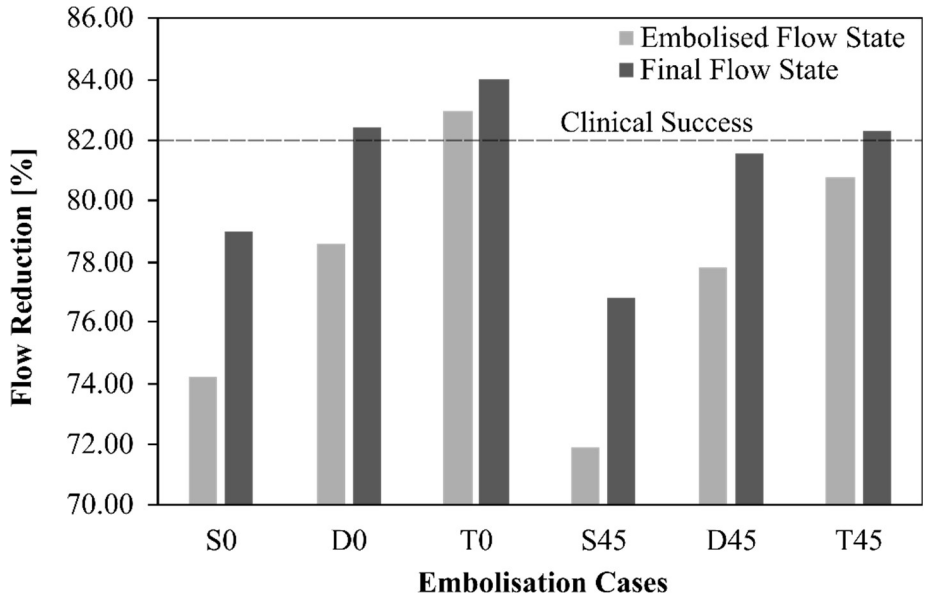

Figure 58: Evaluation of hypotensive embolised states

For the hypotensive cases, exhibited in Figure 58, the flow reductions differ markedly from those observed under hypertensive and standard conditions. Here, the contribution of coils to flow reduction is comparatively lower, but the impact of clotting is enhanced. The reduced flow and shear rates inherent to hypotensive states create an environment conducive to clot formation, which in turn, increases the overall likelihood of clinical success. This is evident in cases D0 and D45, where the pronounced clotting effects pushed D0 to be classified as clinically successful and ultimately to outperform T45, despite lower initial flow reduction by the coils. The favourable conditions for clotting under hypotension suggest that reduced shear rates allow clots to stabilise and expand, making hypotensive conditions particularly advantageous for successful coil embolisation.

Comparing these scenarios highlights distinct mechanisms across the hypertensive, hypotensive, and standard conditions. In the hypertensive cases, higher input velocities allow coils to reduce flow effectively, but the accompanying increased shear rates hinder clot formation. From a biochemical standpoint elevated shear rates in hypertensive conditions hinder coagulation factor accumulation and thrombus stability, thus resulting in reduced clot formation as discussed in findings from Ahmad (2020), and in the case of the investigated embolisation scenarios, leads to a greater reliance on coil performance for success. Conversely, hypotensive conditions demonstrate the opposite trend, i.e., lower initial flow reduction by the coils is offset by significant clotting which thrives under the reduced flow and shear conditions. These comparisons underscore the importance of understanding the interplay between flow dynamics and clotting mechanisms, suggesting that while hypertensive conditions demand robust coil performance, hypotensive environments enhance clotting, providing an alternative route to successful embolisation.

Notably, venous hyper - and hypotension, although recognised conditions, were excluded from this analysis. This exclusion is justified as venous hypertension is often associated with severe, life-threatening illnesses such as congestive heart failure or portal hypertension, where the management of these conditions would take precedence over AVM treatment. Additionally, the impact of venous pressure changes on the AVM embolisation process is less direct compared to alterations in arterial pressures, making arterial conditions more relevant to this study.

4 CONCLUSIONS AND RECOMMENDATIONS

4.1 Conclusions

This study presents a detailed analysis of AVM coil embolisation, combining CFD with experimental verification using 4D MRI to assess the effects of various coil configurations and clot formation on flow reduction. The results have demonstrated significant findings regarding optimisation of coil placement, mechanical factors of clot formation, and the validation of computational models, with insights for clinical practice.

The effect of coil implantation was modelled through the application of a non-uniform porosity field, developed on the basis of a uniform porous media model which has been computationally and experimentally validated, exhibiting a percentage error of 0.25%. The non-uniform porosity model is capable of capturing the intricate coil structure within the AVM vasculature and the corresponding local pressure gradients surrounding the coils.

The role of clot formation was explored through a shear-based porous media model, validated against experimental data. The computational data produced stable clot volumes closely resembling those observed *in vitro*, with a minor deviation of 0.42% when assessed for an idealised aneurysm case, affirming the simplified model's reliability. Clot distribution and total clot size were shown to be influenced by local shear rates, with preferential formation occurring in regions of lower shear. Asymmetric clot distribution is driven by flow-induced differential shear exposure, which suppresses clotting in higher-velocity zones.

Verification of the computational models was achieved through comparison with 4D MRI data, which showed strong coherence in the resultant 3D flow fields. The MRI and CFD datasets exhibited similar qualitative flow structures, including the accurate representation of vortex cores and flow impingement on the AVM wall. Despite localised discrepancies, primarily attributed to MRI's limitations in capturing high-gradient velocities and near-wall flows, the overall agreement confirmed the reliability of the computational models, with most flow regions showing an error range between $0-2\%$. The most significant discrepancies, reaching approximately 22%, were localised to areas of vortical flow adjacent to the core flow. These findings support the use of CFD as a predictive tool for preoperative planning, while demonstrating the feasibility of 4D MRI using a tabletop scanner for complex flow measurement in research contexts.

The effectiveness of coil embolisation was extensively evaluated across six configurations (one to three coils and two different coil insertion angles), revealing that, in the case of the

geometry under investigation, triple coil packing with a straight insertion angle (T0) is the most efficient for achieving AVM occlusion. T0 exhibited the highest packing density of 40.86% and achieved the lowest flow rate of $0.224\ \mathrm{mm}^3/\mathrm{s}$, underscoring its ability to significantly reduce blood flow into the AVM. This configuration along with its $45°$ equivalent, was found to result in a flow rate reduction that suggests clinical success through the development and application of a clinically informed surgical metric of success, a finding that has been verified by clinicians from experience.

Comparative analysis of the stochastically representative coil configurations further emphasised the superiority of straight insertions, which consistently outperformed the angled insertions. The $0°$ coil series achieved higher packing densities than the $45°$ series, even though coils inserted at greater angles relative to the vessel axis might be expected to exhibit increased curvature and packing due to vessel wall impact. As a result of the increased packing densities, the $0°$ series demonstrated lower AVM flow rates, greater pressure reductions and larger end-state clot volumes across all cases. While similar trends may be observed through clinical observation, CFD provides a significant advantage by enabling detailed patient-specific analysis of flow dynamics and coil performance, unlike general guidelines derived from aggregate observations.

This study also investigated the embolisation outcomes under different haemodynamic conditions, including hypertensive and hypotensive states. It was found that hypertensive cases still achieved effective flow reduction, particularly in T0 and T45, but with an increased reliance on mechanical coil performance due to elevated shear rates that hindered clot formation. Conversely, hypotensive conditions promoted more extensive clotting due to reduced shear, compensating for lower overall flow obstruction by the coils. These contrasting mechanisms highlight the need for tailored treatment approaches based on patient-specific haemodynamic profiles, with hypertensive patients benefitting from robust coil placement and hypotensive cases capitalising on clot-favouring conditions.

Ultimately, this study establishes a strong foundation for optimising AVM embolisation techniques by integrating detailed computational modelling with experimental verification. The insights gained underscore the role of such a pre-surgical planning tool, which may better inform clinicians of factors impacting coil placement and packing, the effects of patient-specific co-morbidities on the likelihood of success, and the potential for improving embolisation outcomes and surgical decision-making through enhanced understanding of flow dynamics and clot formation.

4.2 Contributions

The significant contributions made by this work include:

- The development, implementation and validation of porous media techniques for the modelling of coil and clot structures. These models are capable of being applied directly as cell-based fluid property algorithms in CFD solvers.
- The evaluation of coil packing number, density, angle of insertion and the resulting effect of the embolisation cases has evidenced that these factors are not trivial to predict and are not directly related, as for example, the surrounding vasculature plays a dominant role in the resulting coil packing density. This study provides a framework and tool set to assess these variables and how they interact with one another and the surrounding flow so as to optimise embolisation procedures.
- This study reveals how clot formation complements mechanical flow obstruction, varying across haemodynamic conditions. This emphasises the importance of patient-specific factors in optimising embolisation techniques.
- A clinical metric has been formulated and applied in order to directly link the results of the computational models with real-world clinical practice.
- Successful alignment of CFD and 4D MRI data has confirmed the reliability of computational models for predicting embolisation success. This strengthens the role of CFD in preoperative planning and enhances the utility of tabletop MRI scanners employing 4D MRI in clinical diagnostics.

4.3 Recommendations and Future Work

The following recommendations are aimed at extending the application of these models, while improving the reliability and clinical significance of this work. The utility and accuracy of the methods may be improved by considering the following:

1) Refinement

While the current shear-based clotting model accurately predicts stable clot formation, future work should explore the incorporation of biochemical factors such as thrombin generation, transport mechanisms and platelet aggregation. Integrating these elements could provide a more comprehensive understanding of the clotting process especially with respect to the transient nature of clot formation under complex flow conditions, thereby improving predictive accuracy for embolisation outcomes and allowing the model to be extended further into the time domain and the inclusion of factors such as vessel wall elasticity and pulsatile blood flow.

2) Validation of non-uniform porosity model

This study validated the uniform porosity model; however, this model was extended to a non-uniform model without subsequent experimentation and testing. The accuracy and validity of the non-uniform porosity model, while logically sound should be investigated. Future work should thus focus on comparing this model with other computational models of the coil within vascular flows such as volume subtraction methods or Fluid-Structure Interaction (FSI) methods as well as experimental sources and clinical data.

3) Impact of haemodynamic variations on embolisation success

Given the variation under hypertensive, normotensive, and hypotensive conditions, further research should extend this co-morbidity analysis in order to investigate how different patient-specific haemodynamic states influence embolisation success. This, in conjunction with point 1, could include the adaption of the model to fit several biochemical parameters and markers. Developing patient-tailored treatment protocols based on preoperative flow assessments could improve clinical outcomes, especially in complex AVM cases.

4) Advanced imaging practice for improved validation

Relating to the application of 4D MRI through the use of the tabletop scanner, future improvements could include increasing the scan resolution to enhance masking accuracy and near-wall measurements, although this may reduce the signal-to-noise ratio (SNR). To mitigate this, multi-scan averaging may be applied to improve accuracy and provide a clearer signal but would require longer scanning times.

The measurements achieved with the tabletop scanner in this work, were obtained as part of a two-week pilot study at the University of Twente (UT) prior to the University of the Witwatersrand (Wits) acquiring a unit. Setup and encoding recommendations from this study for future work would also include increasing scan time to achieve increased voxel resolutions and to ensure that the flow vessel of interest is mounted in a fixed orientation within the MRI bore for improved post-processing and masking.

5) Development of a clinical tool based on a reduced order model

A Reduced Order Model (ROM) may be derived from the detailed CFD analysis conducted in this study. A ROM would simplify the complex haemodynamic calculations involved in AVM treatment, enabling quick, approximate predictions of flow reduction and clot formation with different coil configurations and insertion angles. Such a model, calibrated against data from this and/or future projects, could allow clinicians to input patient-specific parameters and simulate embolisation outcomes rapidly, aiding in personalised treatment planning. This approach could provide an efficient and accessible decision-support tool.

REFERENCES

Ahmad, S. (2020). Clinical outcome of endovascular coil embolization for cerebral aneurysms in Asian population in relation to risk factors: A 3-year retrospective analysis. *BMC Surgery*, *20*(1). https://doi.org/10.1186/s12893-020-00756-1

Babiker, M. H., Gonzalez, L. F., Albuquerque, F., Collins, D., Elvikis, A., Zwart, C., Roszelle, B., & Frakes, D. H. (2013). An in vitro study of pulsatile fluid dynamics in intracranial aneurysm models treated with embolic coils and flow diverters. *IEEE Transactions on Biomedical Engineering*, *60*(4), 1150–1159. https://doi.org/10.1109/TBME.2012.2228002

Banerjee, M. K., Ganguly, R., & Datta, A. (2012). Effect of Pulsatile Flow Waveform and Womersley Number on the Flow in Stenosed Arterial Geometry. *ISRN Biomathematics*, *2012*, 1–17. https://doi.org/10.5402/2012/853056

Barreau, X., Marnat, G., Gariel, F., & Dousset, V. (2014). Intracranial arteriovenous malformations. In *Diagnostic and Interventional Imaging* (Vol. 95, Issue 12, pp. 1175–1186). Elsevier Masson SAS. https://doi.org/10.1016/j.diii.2014.10.004

Bergou, M., Wardetzky, M., Robinson, S., Audoly, B., & Grinspun, E. (2008). Discrete elastic rods. *ACM Transactions on Graphics*, *27*(3). https://doi.org/10.1145/1360612.1360662

Bokhari, M. R., & Bokhari, S. R. A. (2023). *Arteriovenous Malformation of the Brain.* https://www.ncbi.nlm.nih.gov/books/NBK430744/#:~:text=The%20mortality%20rate%20is%2010,commonly%20occurs%20in%20young%20adults.

Bougardt, J et al. (2024). *In-vitro* and *in-silico* modelling of arteriovenous malformations for surgical planning. In Hoffmann, J., & Venter, M. P. (Eds), *Proceeding of the 13th South African Conference on Computational and Applied Mechanics*. https://saam.africa/

Brass, L. F., & Diamond, S. L. (2016). Transport physics and biorheology in the setting of hemostasis and thrombosis. In *Journal of Thrombosis and Haemostasis* (Vol. 14, Issue 5, pp. 906–917). Blackwell Publishing Ltd. https://doi.org/10.1111/jth.13280

Brown, M., Crawforth, P., & Curtis, D. (2022). Rapid non-destructive sizing of microstructural surface integrity features using x-ray diffraction. *NDT and E International*, *131*. https://doi.org/10.1016/j.ndteint.2022.102682

Carty, G., Chatpun, S., & Espino, D. M. (2016). Modeling Blood Flow Through Intracranial Aneurysms: A Comparison of Newtonian and Non-Newtonian Viscosity.

Journal of Medical and Biological Engineering, *36*(3), 396–409. https://doi.org/10.1007/s40846-016-0142

Casa, L. D. C., Ku, D. N., & Woodruff, G. W. (2017). *Thrombus Formation at High Shear Rates*. https://doi.org/10.1016/j.jvs.2014.12.050

Cherry, E. M., & Eaton, J. K. (2013). Shear thinning effects on blood flow in straight and curved tubes. *Physics of Fluids*, *25*(7). https://doi.org/10.1063/1.4816369

Cox, J. A., Bartlett, E., & Lee, E. I. (2014). Vascular malformations: A review. In *Seminars in Plastic Surgery* (Vol. 28, Issue 2, pp. 58–63). Thieme Medical Publishers, Inc. https://doi.org/10.1055/s-0034-1376263

Darling, C. L., Le, C. Q., Featherstone, J. D. B., & Fried, D. (2009). An automated digital microradiography system for assessing tooth demineralization. *Lasers in Dentistry XV*, *7162*, 71620T. https://doi.org/10.1117/12.816868

de Leacy, R., Ansari, S. A., Schirmer, C. M., Cooke, D. L., Prestigiacomo, C. J., Bulsara, K. R., & Hetts, S. W. (2022). Endovascular treatment in the multimodality management of brain arteriovenous malformations: report of the Society of NeuroInterventional Surgery Standards and Guidelines Committee. *Journal of NeuroInterventional Surgery*, *14*(11), 1118–1124. https://doi.org/10.1136/neurintsurg-2021-018632

Diamond SL. (1999). Engineering design of optimal strategies for blood clot dissolution. Annu Rev Biomed Eng. 1999;1:427-62.

Du, J., Kim, D., Alhawael, G., Ku, D. N., & Fogelson, A. L. (2020). Clot Permeability, Agonist Transport, and Platelet Binding Kinetics in Arterial Thrombosis. *Biophysical Journal*, *119*(10), 2102–2115. https://doi.org/10.1016/j.bpj.2020.08.041

Endovascular Today-US Device Guide-Microcatheters. (2024).

Frank, M., Holzberger, F., Horvat, M., Kirschke, J., Mayr, M., Muhr, M., Nebulishvili, N., Popp, A., Schwarting, J., & Wohlmuth, B. (2024). Numerical simulation of endovascular treatment options for cerebral aneurysms. *GAMM Mitteilungen*. https://doi.org/10.1002/gamm.202370007

Franzetti, G., Bonfanti, M., Tanade, C., Lim, C. S., Tsui, J., Hamilton, G., Díaz-Zuccarini, V., & Balabani, S. (2021). *Effective Computational Framework for Pre-Interventional Planning of Peripheral Arteriovenous Malformations with In Vivo and In Vitro Validation*. https://doi.org/10.1101/2021.05.15.444310

Friesen, J., Bergner, J., Khan, M. I. A., Triess, S., Zoll, A., Pelz, P. F., & Adili, F. (2021). Comparison of existing aneurysm models and their path forward. In *Computer Methods and Programs in Biomedicine Update* (Vol. 1). Elsevier B.V. https://doi.org/10.1016/j.cmpbup.2021.100019

Gallo, C., Ridolfi, L., & Scarsoglio, S. (2020). Cardiovascular deconditioning during long-term spaceflight through multiscale modeling. *Npj Microgravity*, *6*(1). https://doi.org/10.1038/s41526-020-00117-5

Gao, E., Young, W., Ornstein, E., Pile-Spellman, J., & Ma, Q. (1997). Journal of' Cerebral Blood Flow and Metabolism A Theoretical Model of Cerebral Hemodynamics: Application to the Study of Arteriovenous Malformations.

Heshmat, A., Barreto, I., Rill, L., Liu, S., Patel, R., & Arreola, M. (2023). Contrast thresholds for detection of various iodine concentrations in subtraction CT and dual-energy CT systems. *Journal of Applied Clinical Medical Physics*, *24*(1). https://doi.org/10.1002/acm2.13834

Holzberger, F., Muhr, M., & Wohlmuth, B. (2024). A comprehensive numerical approach to coil placement in cerebral aneurysms: mathematical modeling and in silico occlusion classification. *Biomechanics and Modeling in Mechanobiology*. https://doi.org/10.1007/s10237-024-01882-y

Hyun, K. K., Ho, S. S., Yong, H. F., Sung, Y. P., Chang, M. H., & Sun, K. (2005). The effects of pulsatile flow upon renal tissue perfusion during cardiopulmonary bypass: A comparative study of pulsatile and nonpulsatile flow. *ASAIO Journal*, *51*(1), 30–36. https://doi.org/10.1097/01.MAT.0000150324.02040

Jafarinia, A., Armour, C. H., Gibbs, R. G. J., Xu, X. Y., & Hochrainer, T. (2022). Shear-driven modelling of thrombus formation in type B aortic dissection. *Frontiers in Bioengineering and Biotechnology*, *10*. https://doi.org/10.3389/fbioe.2022.1033450

Jain, K. (2016). *Transition to Turbulence in Physiological Flows: Direct Numerical Simulation of Hemodynamics in Intracranial Aneurysms and Cerebrospinal Fluid Hydrodynamics in the Spinal Canal*.

Jalali, A., Delouei, A. A., Khorashadizadeh, M., Golmohammadi, A. M., & Karimnejad, S. (2020). Mesoscopic simulation of forced convective heat transfer of Carreau-Yasuda fluid flow over an inclined square: Temperature-dependent viscosity. *Journal of Applied and Computational Mechanics*, *2*, 307–319. https://doi.org/10.22055/jacm.2019.29503.1605

Kalayci, T, O., Sonmezgoz, F., Apaydin, M., Inci, M, F., Sarp, A, F., Birlik, B., Uluç, M, E., Oyar, O & Kestelli, M. Venous flow volume measured by duplex ultrasound can be used as an indicator of impaired tissue perfusion in patients with peripheral arterial disease. (2015). *Medical Ultrasonography*, *17*(4). https://doi.org/10.11152/mu.2013.2066.174.flw

Kaneko, N., Ullman, H., Ali, F., Berg, P., Ooi, Y. C., Tateshima, S., Colby, G. P., Komuro, Y., Hu, P., Khatibi, K., Ponce Mejia, L. L., Szeder, V., Nour, M., Guo, L., Chien, A., Vinuela, F., Nemoto, S., Mashiko, T., Sehara, Y., … Jahan, R. (2020). In Vitro Modeling of Human Brain Arteriovenous Malformation for Endovascular Simulation and Flow Analysis. *World Neurosurgery*, *141*, e873–e879. https://doi.org/10.1016/j.wneu.2020.06.084

Kaproth-Joslin, K., Hobbs, S., Rajiah, P., Chaturvedi, A., & Chaturvedi, A. (2022). Optimizing low contrast volume thoracic CT angiography: From the basics to the advanced. *Journal of Clinical Imaging Science*, *12*. https://doi.org/10.25259/JCIS_51_2022

Kim, J., Kim, J. H., Lee, H. S., Suh, S. H., & Lee, K. Y. (2021). Association between longitudinal blood pressure and prognosis after treatment of cerebral aneurysm: A nationwide population-based cohort study. *PLoS ONE*, *16*(5 May). https://doi.org/10.1371/journal.pone.0252042

Koning, N. J., A Vonk, A. B., van Barneveld, L. J., Beishuizen, A., Atasever, B., van den Brom, C. E., Boer, C., & Barneveld, van L. (2012). Pulsatile flow during cardiopulmonary bypass preserves postoperative microcirculatory perfusion irrespective of systemic hemodynamics. *J Appl Physiol*, *112*, 1727–1734. https://doi.org/10.1152/japplphysiol.01191.2011

Kyung, S. C., Balaras, E., Lieber, B. B., Sadasivan, C., & Wakhloo, A. K. (2007). Modeling the interaction of coils with the local blood flow after coil embolization of intracranial aneurysms. *Journal of Biomechanical Engineering*, *129*(6), 873–879. https://doi.org/10.1115/1.2800773

Lezak B & Varacallo M. Anatomy, Bony Pelvis and Lower Limb, Foot Veins. [Updated 2022 Nov 7]. In: StatPearls [Internet]. Treasure Island (FL): StatPearls Publishing; 2024 Jan-. [Figure, Vasculature of the Lower Limbs Public Domain, via Clker Free Vector Images] https://www.ncbi.nlm.nih.gov/books/NBK542295/figure/article-32233.image.f1/

Li, M., Hotaling, N. A., Ku, D. N., & Forest, C. R. (2014). Microfluidic thrombosis under multiple shear rates and antiplatelet therapy doses. *PLoS ONE*, *9*(1). https://doi.org/10.1371/journal.pone.0082493

Lieber, B. B., Sadasivan, C., Hao, Q., Seong, J., & Cesar, L. (2009). The mixability of angiographic contrast with arterial blood. *Medical Physics*, *36*(11), 5064–5078. https://doi.org/10.1118/1.3243079

Linh, D.-T. N., Khanh, L., Dung, L. T., Ha, N. H., Son, T. T., & Duc, N. M. (2022). Recurrence after treatment of arteriovenous malformations of the head and neck. *AIMS Medical Science*, *9*(1), 9–17. https://doi.org/10.3934/medsci.2022003

Lopes, D., Puga, H., Teixeira, J. C., & Teixeira, S. F. (2019). Influence of arterial mechanical properties on carotid blood flow: Comparison of CFD and FSI studies. *International Journal of Mechanical Sciences*, *160*, 209–218. https://doi.org/10.1016/j.ijmecsci.2019.06.029

Lorbeer, R., Grotz, A., Dörr, M., Völzke, H., Lieb, W., Kühn, J. P., & Mensel, B. (2018). Reference values of vessel diameters, stenosis prevalence, and arterial variations of the lower limb arteries in a male population sample using contrast-enhanced MR angiography. *PLoS ONE*, *13*(6). https://doi.org/10.1371/journal.pone.0197559

Lowe, J. A., Barton, E., Leslie, L. J., Souppez, J.-B. R. G., Fratini, A., Ho, W. H., Yazdi, S. G., & Geoghegan, P. (n.d.). *An In-Vitro Study on the Carotid Bifurcation and its Influence on Arterial Haemodynamics with Newtonian and Non-Newtonian Blood Analogs*.

Majumdar, S., & McWilliams, J. P. (2020). Approach to pulmonary arteriovenous malformations: A comprehensive update. In *Journal of Clinical Medicine* (Vol. 9, Issue 6, pp. 1–26). MDPI. https://doi.org/10.3390/jcm9061927

Maredza, M., Bertram, M. Y., & Tollman, S. M. (2015). Disease burden of stroke in rural South Africa: An estimate of incidence, mortality and disability adjusted life years. *BMC Neurology*, *15*(1). https://doi.org/10.1186/s12883-015-0311-7

Morales, H. G., Kim, M., Vivas, E. E., Villa-Uriol, M. C., Larrabide, I., Sola, T., Guimaraens, L., & Frangi, A. F. (2011). How do coil configuration and packing density influence intra-aneurysmal hemodynamics? *American Journal of Neuroradiology*, *32*(10), 1935–1941. https://doi.org/10.3174/ajnr.A2635

Morales, H. G., Larrabide, I., Geers, A. J., Aguilar, M. L., & Frangi, A. F. (2013). Newtonian and non-Newtonian blood flow in coiled cerebral aneurysms. *Journal of Biomechanics*, *46*(13), 2158–2164. https://doi.org/10.1016/j.jbiomech.2013.06.034

Nataraj, A., Mohamed, M. B., Gholkar, A., Vivar, R., Watkins, L., Aspoas, R., Gregson, B., Mitchell, P., & Mendelow, A. D. (2014). Multimodality Treatment of Cerebral Arteriovenous Malformations. In *World Neurosurgery* (Vol. 82, Issues 1–2, pp. 149–159). Elsevier Inc. https://doi.org/10.1016/j.wneu.2013.02.064

Ngoepe, M. N., & Ventikos, Y. (2016). Computational modelling of clot development in patient-specific cerebral aneurysm cases. *Journal of Thrombosis and Haemostasis*, *14*(2), 262–272. https://doi.org/10.1111/jth.13220

Ngoepe, M. N., Pretorius, E., Tshimanga, I. J., Shaikh, Z., Ventikos, Y., & Ho, W. H. (2021). Thrombin–Fibrinogen In Vitro Flow Model of Thrombus Growth in Cerebral Aneurysms. *TH Open*, *05*(02), e155–e162. https://doi.org/10.1055/s-0041-1728790

Onciu, C. v., Maffeis, J., Popescu, I. A., & Teboul, F. (2024). A rare case of arteriovenous malformation of the forearm. *Annals of Vascular Surgery - Brief Reports and Innovations*, *4*(2). https://doi.org/10.1016/j.avsurg.2024.100282

Oparil, S., Acelajado, M. C., Bakris, G. L., Berlowitz, D. R., Cífková, R., Dominiczak, A. F., Grassi, G., Jordan, J., Poulter, N. R., Rodgers, A., & Whelton, P. K. (2018). Hypertension. In *Nature Reviews Disease Primers* (Vol. 4). Nature Publishing Group. https://doi.org/10.1038/nrdp.2018.14

Osuga, K., Mikami, K., Higashihara, H., Maeda, N., Tsuboyama, T., Kuwabara, M., Onishi, H., Hori, M., Kim, T., Tomoda, K., Murakami, T., & Nakamura, H. (2006). Principles and techniques of transcatheter embolotherapy for peripheral vascular lesions. In *Radiation Medicine - Medical Imaging and Radiation Oncology* (Vol. 24, Issue 4, pp. 309–314). https://doi.org/10.1007/s11604-006-2411-1

Panneerselvam, N. K., Sudhir, B. J., Kannath, S. K., & Patnaik, B. S. V. (2023). Hemodynamic analysis of coil filled patient-specific middle cerebral artery aneurysm using porous medium approach. *Physics of Fluids*, *35*(11). https://doi.org/10.1063/5.0173688

Perrira, N., Shuib, A. S., Phang, S. W., & Muda, A. S. (2022). Experimental Investigation of Blood Mimicking Fluid Viscosity for Application in 3D-Printed Medical Simulator. *Journal of Physics: Conference Series*, *2222*(1). https://doi.org/10.1088/1742-6596/2222/1/012016

Piasecki, P., Ziecina, P., Brzozowski, K., Wierzbicki, M., & Narloch, J. (2020). Intra-aneurysmal pressure changes during stent-assisted coiling. *PLoS ONE*, *15*(6). https://doi.org/10.1371/journal.pone.0233981

Potter, M.C. , Wiggert, D.C., Ramadan, B.H. (2010). *Mechanics of Fluids.* 4th Edition.

Rutledge, W. C., Ko, N. U., Lawton, M. T., & Kim, H. (2014). Hemorrhage Rates and Risk Factors in the Natural History Course of Brain Arteriovenous Malformations. In *Translational Stroke Research* (Vol. 5, Issue 5, pp. 538–542). Springer US. https://doi.org/10.1007/s12975-014-0351-0

Sakariassen, K. S., Orning, L., & Turitto, V. T. (2015). The impact of blood shear rate on arterial thrombus formation. In *Future Science OA* (Vol. 1, Issue 4). Future Medicine Ltd. https://doi.org/10.4155/fso.15.28

Saqr, K. M., Tupin, S., Rashad, S., Endo, T., Niizuma, K., Tominaga, T., & Ohta, M. (2020). Physiologic blood flow is turbulent. *Scientific Reports*, *10*(1). https://doi.org/10.1038/s41598-020-72309-8

Savage, B., & Saldívar, E., et al. (1996). Initiation of Platelet Adhesion by Arrest onto Fibrinogen or Translocation on von Willebrand Factor. In *Cell* (Vol. 84).

Sezai, A., Shiono, M., Orime, Y., Nakata, K. I., Hata, M., Iida, M., Kashiwazaki, S., Kinoshita, J. I., Nemoto, M., Koujima, T., Furuichi, M., Eda, K., Hirose, H., Yoshino, T., Saitoh, A., Taniguchi, Y., & Sezai, Y. (1999). Major organ function under mechanical support: Comparative studies of pulsatile and nonpulsatile circulation. *Artificial Organs*, *23*(3), 280–285. https://doi.org/10.1046/j.1525-1594.1999.06318

Shah P, Louis MA. Physiology, Central Venous Pressure. 2023 Jul 10. In: StatPearls [Internet]. Treasure Island (FL): StatPearls Publishing; 2024 Jan–. PMID: 30137777.

Sharma S, Hashmi MF, Bhattacharya PT. Hypotension. 2023 Feb 19. In: StatPearls [Internet]. Treasure Island (FL): StatPearls Publishing; 2024 Jan–. PMID: 29763136.

Siebert, M. W., & Fodor, P. S. (2009). *Newtonian and Non-Newtonian Blood Flow over a Backward-Facing Step-A Case Study*.

Sillanpää, N., Saarinen, J. T., Rusanen, H., Elovaara, I., Dastidar, P., & Soimakallio, S. (2013). Location of the clot and outcome of perfusion defects in acute anterior circulation stroke treated with intravenous thrombolysis. *American Journal of Neuroradiology*, *34*(1), 100–106. https://doi.org/10.3174/ajnr.A3149

Siogkas, P. K., Papafaklis, M. I., Sakellarios, A. I., Stefanou, K. A., Bourantas, C. v., Athanasiou, L. S., Exarchos, T. P., Naka, K. K., Michalis, L. K., Parodi, O., & Fotiadis, D. I. (2015). Patient-specific simulation of coronary artery pressure measurements: An in vivo three-dimensional validation study in humans. *BioMed Research International*, *2015*. https://doi.org/10.1155/2015/628416

Spiegel, M., Redel, T., Zhang, J. J., Struffert, T., Hornegger, J., Grossman, R. G., Doerfler, A., & Karmonik, C. (2011). Tetrahedral vs. polyhedral mesh size evaluation on flow velocity and wall shear stress for cerebral hemodynamic simulation. *Computer Methods in Biomechanics and Biomedical Engineering*, *14*(1), 9–22. https://doi.org/10.1080/10255842.2010.518565

Taylor RE, Mager P, Yu NC, Katz DP, Brady JR, Gupta N. Iodine quantification and detectability thresholds among major dual-energy CT platforms. Br J Radiol. 2019 Dec;92(1104):20190530. doi: 10.1259/bjr.20190530. Epub 2019 Oct 7. PMID: 31559858; PMCID: PMC6913374.

Teigen, C. (2015). *A Complete Embolisation System*. https://evtoday.com/articles/2015-apr/a-complete-embolization-system

Teixeira, F. S., Neufeld, E., Kuster, N., & Watton, P. N. (2020). Modeling intracranial aneurysm stability and growth: an integrative mechanobiological framework for clinical cases. *Biomechanics and Modeling in Mechanobiology*, *19*(6), 2413–2431. https://doi.org/10.1007/s10237-020-01351-2

Trerotola, S. O., Pressler, G. A., & Premanandan, C. (2019). Nylon Fibered Versus Non-Fibered Embolization Coils: Comparison in a Swine Model. *Journal of Vascular and Interventional Radiology*, *30*(6), 949–955. https://doi.org/10.1016/j.jvir.2018.10.004

Uller, W., Alomari, A. I., & Richter, G. T. (2014). Arteriovenous malformations. *Seminars in Pediatric Surgery*, *23*(4), 203–207. https://doi.org/10.1053/j.sempedsurg.2014.07.005

Umeda, Y., Ishida, F., Tsuji, M., Furukawa, K., Shiba, M., Yasuda, R., Toma, N., Sakaida, H., & Suzuki, H. (2017). Computational fluid dynamics (CFD) using porous media modeling predicts recurrence after coiling of cerebral aneurysms. *PLoS ONE*, *12*(12). https://doi.org/10.1371/journal.pone.0190222

Valencia, A., Zarate, A., Galvez, M., & Badilla, L. (2006). Non-Newtonian blood flow dynamics in a right internal carotid artery with a saccular aneurysm. *International Journal for Numerical Methods in Fluids*, *50*(6), 751–764. https://doi.org/10.1002/fld.1078

Vedantu. (n.d.). *Briefly describe the stages in the clotting of blood.* Retrieved from https://www.vedantu.com/question-answer/briefly-describe-the-stages-in-the-clotting-of-class-11-biology-cbse-5fca8f76da46832f5e0b7c7a

Wani, M. L., Ahangar, A. G., Ganie, F. A., Wani, S. N., & Wani, N. D. (2012). Vascular injuries: Trends in management. In *Trauma Monthly* (Vol. 17, Issue 2, pp. 266–269). Baqiatallah University of Medical Sciences. https://doi.org/10.5812/traumamon.6238

WHO. (2022). *Health situation analysis of the African Region Country Profiles*. (2022). http://apps.who.int/bookorders.

Yakes, W., & Baumgartner, I. (2014). Interventional treatment of arterio-venous malformations. *Gefasschirurgie*, *19*(4), 325–330. https://doi.org/10.1007/s00772-013-1303-9

Yesudasan, S., & Averett, R. D. (2019). Recent advances in computational modeling of fibrin clot formation: A review. In *Computational Biology and Chemistry* (Vol. 83). Elsevier Ltd. https://doi.org/10.1016/j.compbiolchem.2019.107148

Yi, K. H., Lee, J. J., Hur, H. W., & Kim, H. J. (2021). Anatomical consideration of deep calf veins: application to catheter-directed thrombolysis. *Surgical and Radiologic Anatomy*, *43*(12), 2071–2076. https://doi.org/10.1007/s00276-021-02821-7

Zafar W.,Masood, A., Iqbal, B., & Murad, S. (2019). Resolution, SNR, signal averaging and scan time in MRI formetastatic lesion in spine. A case report 1 MedDocs Publishers. In *J Radiol Med Imaging* (Vol. 2, Issue 1). http://meddocsonline.org/

Zhang, C., Chau, N., & Ho, H. (2020). Patient-Specific Blood Flow Analysis for Cerebral Arteriovenous Malformation Based on Digital Subtraction Angiography Images. *Frontiers in Bioengineering and Biotechnology*, *8*. https://doi.org/10.3389/fbioe.2020.00775

APPENDICES

Appendix A

Formlabs Form 3 Printer Specifications

Table A1: Formlabs Form 3 Printer Specifications

Component/Part/Specification	Details
Light Source	Class 1 Laser, 450 nm wavelength, 250 mW laser, 85 µm laser spot size
Maximum Print Speed	31 mm/hour
Surface Accuracy	87% {100 µm of CAD model} 66% {50 µm of CAD model}
Build Volume (W × D × H)	14.5 × 14.5 × 19.3 cm
Build Area	210 cm^2
Maximum Part Length	22.4 cm
XY Resolution	25 µm
Layer Thickness	25 – 300 µm
Internal Temperature	35 ℃
Printer Dimensions (W × D × H)	40.5 × 37.5 × 53 cm
Minimum Access Dimensions (W × D × H)	40.5 × 53 × 78 cm
Printer Weight	17.5 kg
Operating Environment	18 – 28 ℃
Power Requirements	100 – 240 VAC, 2.5 A, 50/60 Hz, 220 W
Software	PreForm, Dashboard, Fleet Control
Resin Tank Estimated Lifetime	250 – 800 hour of printing and/or 10 – 35 weeks exposed to resin

Figure A1: Formlabs Form 3 SLA Printer

Appendix B

TA Instruments AR2000 Rheometer Specifications

Table B1: TA Instruments AR2000 Rheometer Technical Specifications

Component/Part/Specification	Details
Minimum Torque	$0.1\ \mu Nm$
Maximum Torque	$200\ mNm$
Motor Inertia	$15\ \mu Nms^2$
Angular Velocity Range	$10^{-8} - 300\ rad/s$
Frequency Range	$1.2 \times 10^{-7} - 100\ Hz$
Displacement Resolution	$0.04\ \mu rad$
Air Bearing	Porous Carbon
Gap Resolution	$0.06\ \mu m$
Normal Force Range	$0.01 - 50\ N$
Peltier Plate Temperature Controls (TC)	-20 to $200\ ℃$
Environmental Test Chamber TC	-150 to $200\ ℃$
Concentric Cylinder-Peltier TC	-10 to $150\ ℃$

Figure B1: TA Instruments AR2000 Rheometer

Appendix C

Pure Devices tabletop Research MRI Specifications

Table E1: Pure Devices tabletop Research MRI Unit Technical Specifications

Component/Part/Specification	Details
Magnet Unit (magspec)	
Bore size	15 mm
Field Strength	0.55 T
Gradient Strength (built-in gradient amplifier)	120 mT/m (x, y) 125 mT/m (z)
Gradient Strength (external DC-600 gradient amplifier)	480 mT/m (x, y) 500 mT/m (z)
Gradient efficiency	120 mT/m/A (x, y) 125 mT/m/A (z)
Sample diameter imaging	15 mm
Field homogeneity (FOV)	$<$ 30 ppm
Field homogeneity (5 mm)	$<$ 10 ppm
Connection to the imaging unit	RJ − 45
Connection of the receiver/transmitter	BNC
Dimensions (L × W × H)	27 × 25 × 14 cm
Weight	22.5 kg
Control Unit (drive^l)	
PC connection	USB − B 2.0
Connection of the imaging unit	RJ − 45
Connection of the receiver/transmitter	SMB
Power supply	12 V DC, 2 A
Power supply unit (external)	100 − 240 V AC, 50/60 Hz, 2 A
Dimensions (L × W × H)	27 × 9.5 × 14 cm
Weight	2.3 kg
openMATLAB interface	
Product licence	Can only be used with drive^l
System Requirements	
MATLAB	MATLAB 2016a or later
Operating system	Windows 10 or 11 (64-bit)

Figure E1: Pure Devices tabletop MRI Research Unit and $drive^l$ control unit